



RETURNING MATERIALS:
Place in book drop to
remove this checkout from
your record. FINES will
be charged if book is
returned after the date
stamped below.

--	--	--

STRUCTURAL AND ELECTRICAL PROPERTIES
OF GRAPHITE INTERCALATION COMPOUNDS
AND GRAPHITE FIBER COMPOUNDS

by

Xiao-Wen Qian

A DISSERTATION

Submitted to
Michigan State University
in Partial Fulfillment of the Requirements
for the Degree of

DOCTOR OF PHILOSOPHY

Department of Physics and Astronomy

1986

ABSTRACT

STRUCTURAL AND ELECTRIC PROPERTIES OF GRAPHITE INTERCALATION COMPOUNDS AND GRAPHITE FIBER COMPOUNDS

by

Xiao-Wen Qian

The structure of metal-ammonia $K-NH_3$ liquid layers in the ternary graphite intercalation compound $K(NH_3)_{4.33}C_{24}$ at room temperature is studied by measuring the in-plane X-ray diffuse scattering from the intercalant layers. A c^* ($q = 0.88, q_c^*$) scan performed on the system shows that the liquid layers in different graphite galleries are uncorrelated, and the liquid layer is 2 dimensional (2D). We modeled the 2D liquid layer structure using a computer generated planar distribution of hard K^+ and NH_3 discs. The modeled structure is the close packing of two building blocks: N-fold clusters that are formed by attaching four NH_3 discs with variable radii symmetrically to a fixed radius K^+ disc and a unbound "spacer" NH_3 disc. The expressions for the in-plane and c^* contributions to the scattering from such 2D liquids in the galleries of graphite were deduced and applied to the generated model. By comparing the calculated scattering pattern with the experimental results, we concluded that the 2D $K-NH_3$ liquid layers have

a 4-fold coordinated structure that is the planar analogue of the 6-fold coordinated structure found in bulk (3D) $K-NH_3$ solutions.

The microscopic bromine distribution in pitch-based brominated graphite fibers has been measured with a field emission scanning transmission electron microscope (STEM) by monitoring the Br $K\alpha_1$ X-ray intensity. An inhomogeneous distribution of Br along the fiber is found with two distinct cross-sectional distributions, namely: a uniform distribution in Br-rich regions and a Gaussian-like distribution in Br-poor regions. A model based on these Br distribution measurements is proposed to understand the relation between the Br microstructure and the macroscopic residual resistance of the fiber. This model yields semiquantitative agreement with experimental results.

ACKNOWLEDGMENT

It gives me great pleasure to acknowledge my advisor and collaborator Professor Stuart A. Solin, who introduced me to this research field, and whose intuitive insight and rich experiences have guided me through every stage of this work. I thank him for his helpful criticisms and other generous help in the time of need.

I also benefited a great deal from the collaborations with D.M. Hwang, D.R. Stump, B.R. York, R.M. Fronco and many more. Interactions with them gave me a unique experience that this author will remember for a long time to come. I also thank Y.B. Fan, Y.Y. Huang, and S. Lee for their assistance and for many interesting discussions. I am particularly grateful to Vivion E. Shull for his invaluable assistance in using the electron microscope and for much other help. Finally, the financial support from NSF, NASA and Exxon are also acknowledged.

FORWARD

Considerable efforts in both theory and experiment have been made to study low dimensional, particularly 2 dimensional (2D), phenomena in recent years. Examples of systems which exhibit 2D properties are: (1) multi-layered structural materials including those synthesized by the breakthrough technology of molecular beam epitaxy (MBE) and less costly natural lamellar materials like graphite intercalation compounds (GIC's), and clay intercalated compounds (CIC's). (2) single layer systems such as adsorbed layers on the surface of a substrate material and the inversion layer in a MOSFET. In these families of low dimensional system, GICs, in which the intercalant is monolayer or a trilayer constituent alternating with n graphite layers in a staged periodic superlattice structure, stand out for many special properties. Among those are the atomic level epitaxy and great tunability both structurally and electronically that enable us to study the whole spectrum of dimensional effects ranging from 1D through quasi-2D, 2D-3D crossover, and 3D phenomena. Our interests have been in low dimensional structural and electrical properties of the GICs, and for this purpose the first part of this thesis is devoted to detection and characterization of a 2D metal-ammonia liquid solution structure in a unique GIC, i.e. potassium-ammonia solution intercalated graphite compound. The study of the structural and electric properties of other GICs system are collected in the appendices. The second part of this thesis deals with a different form of graphite compound, i.e. graphite

fiber compounds. The relations between the electrical properties and structural properties of these fiber compounds are probed.

Part I and Part II of this thesis have been published or are in press in the Physical Review and are referenced as follows, X.W. Qian, D.R. Stump and S.A. Solin, Phys. Rev. B, 33, 5756(1985), and X.W. Qian, S.A. Solin and J.R. Gaier, Phys. Rev. B, in press.

TABLE OF CONTENTS

OVERVIEW	1
PART I: Structural Properties of Potassium-Ammonia Liquids in Graphite	
I. Introduction	15
II. Experimental techniques and results	19
III. X-ray scattering from stacked 2D liquid layers	24
IV. Structural model	29
V. Radial distribution function	52
VI. Concluding Remarks	57
VII. Acknowledgment and references list	60
PART II. The Microstructural-Derived Macroscopic Residual Resistance of Brominated Graphite Fibers.	
I. Introduction	64
II. Experimental techniques and justifications	66
III. The fiber resistance calculation	75
IV. Experimental results and discussions	77
V. Concluding remarks and summary	85
VI. Acknowledgment and references list	87
APPENDICES	90
Reprints and Preprints of Additional Published/Submitted Papers.	

OVERVIEW

The subject of graphite intercalation compounds (GIC's) has become a large research field mainly due to the tremendous efforts of physicists, chemists and material scientists during the last few decades. Major efforts of the researchers have been on the structural, electrical and magnetic properties of these compounds, although many other properties such as thermal transport, vibrational excitations etc. have also been investigated. However, in this overview only the structural properties of GICs will be briefly reviewed with stress on the low dimensional characteristics of the material.

The understanding the structure of GIC's begins with the knowledge of the parent material graphite. Graphite is a prototypical layered structural material whose structure is shown in Fig. 1 [Ref. 1]. Notice that carbon atoms are covalently bonded into a hexagonal lattice plane, and that these planes are then stacked in the \vec{c} direction and bound by Van de Waals type interactions. The weak interplane bonding of carbon atoms coupled with very strong intraplane bonding gives rise to a large anisotropy in both the structural and the electronic properties of graphite. Structurally, the anisotropy is manifested in the large difference between the c-axis and a-axis lattice constants and force constants. For instance the nearest carbon-carbon (C-C) distance within the basal plane is only 1.42 Å, while the interplane distance is 3.35 Å. This anisotropic structure makes it possible to insert foreign species in between the basal planes without significantly altering the integrity of carbon layer structure. In fact many types of atoms or multi-atom

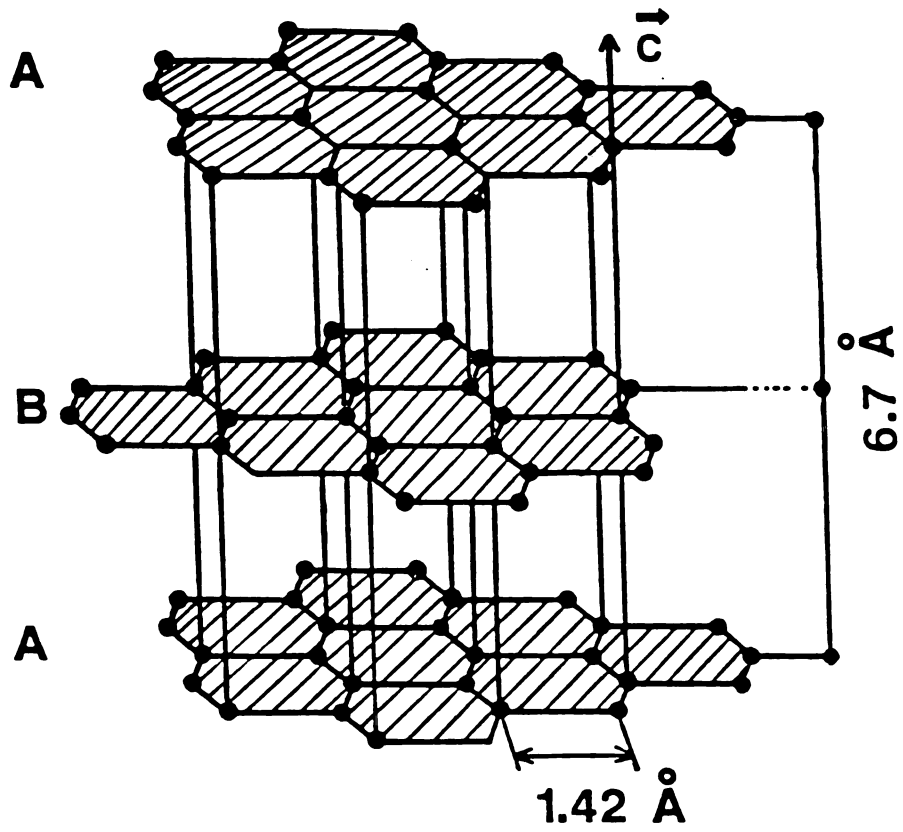


Fig. 1. The structure of hexagonal graphite.

molecules can be intercalated into graphite under appropriate conditions to form a mono-atomic or a tri-atomic or monomolecular thick layer in the galleries between the carbon basal planes. This intercalation process is always accompanied by a charge transfer between the intercalant and host graphite. Depending on the sign of the charge transfer, a GIC is called a donor compound if electrons are given to the host by the intercalant, and an acceptor compound if electrons are transferred from the carbon layer to the intercalant. Alkali metal intercalated GIC's are examples of donor compounds, and strongly acidic molecules such as HNO_3 , SbCl_5 , Br_2 intercalated into graphite are examples of the acceptor compounds.

An important and essentially unique characteristic of GIC's is the staging phenomena, which is the periodic sequencing of carbon layers and intercalant layers as shown in Fig. 2. The stage number n is defined by n carbon layers in between two adjacent intercalant layers. Both theoretical and experimental studies have been conducted to understand this interesting property of GIC's.^{2,3,4} It has been revealed that the formation of the stage is driven by two fields: (1) a strain field that produces an attractive interaction between intercalants in the same layer and a repulsive interaction between the intercalants in different layers, and (2) a static electric field produced by the ionized intercalant and mediated by host carbon layers that yield an additional long range repulsive interaction between intercalants in different layers. These two fields are responsible for the formation and

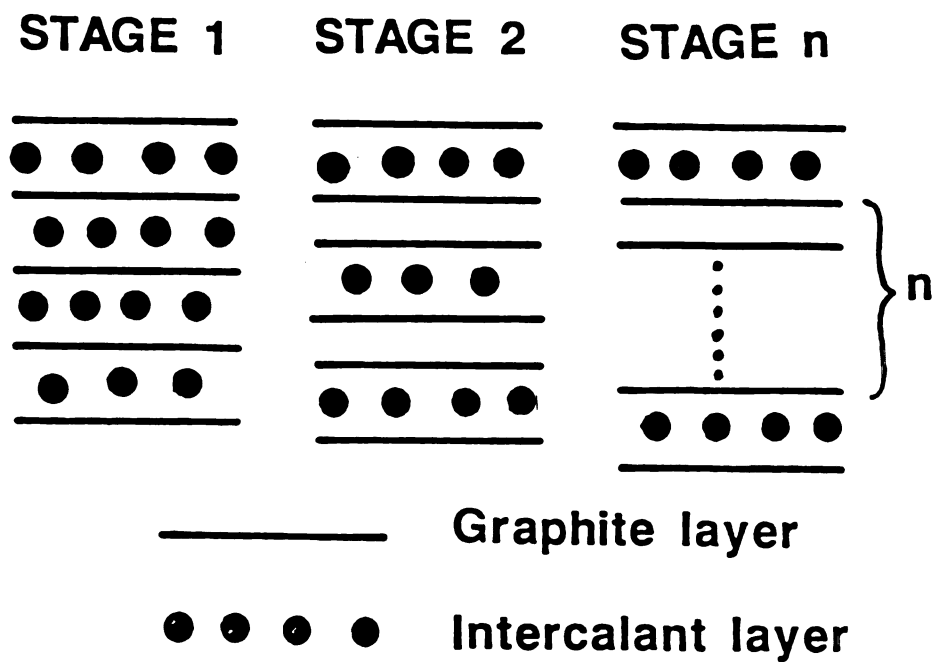


Fig. 2. The \vec{c} -axis stacking sequence of graphite layers and intercalant layers in stages 1, 2, and n graphite intercalation compounds.

stabilization of the stage structure, although other mechanisms such as the formation of microscopic intercalant islands also play a role.⁵

While the structural ordering in the \vec{c} -axis direction, i.e. staging phenomena, has been recently understood quite well¹, many efforts have also been devoted to the understanding of intercalant in-plane structure.^{1,6} GIC's, in this aspect, provide a rich system with which to study quasi-2D phenomena, since under many favorable conditions the intercalant layers can be considered as a good approximation of a 2D system

In principle, the intercalant atoms are always in the potential field imposed by carbon layers (particularly the two bounding layers) and by other intercalant layers. Therefore the structure of the intercalant layer will always be affected by the carbon layer substrate and vice versa. In fact these mutual effects have been studied by many workers. For example, Casswell, Solin¹ and Zabel⁶ et al studied the intercalant layer structure in alkali metal intercalated GIC's, where they found that the alkali metal-carbon interaction plays a dominant role in the ordered phase of the alkali metal at low temperature. Recently work by Moss⁷ and Moret⁸ showed that even in the liquid phase of the alkali metal layer at room temperature, the modulation on the liquid structure due to the graphite layer potential is quite pronounced, although the largest graphite substrate potential modulation is only 0.091 eV [Ref. 9]. On the other hand the presence of intercalant in the graphite also affects the carbon layer structure. However this effect is found to be small due to the strong covalent bonding between the

carbon atoms in the host layer. For example intercalation induced change in the intraplanar carbon-carbon distance has been found to always be less than 1%.^{1,10} These findings by various researchers indicate that the carbon layer in the graphite is a rather smooth substrate on which intercalants ions or atoms can be quite mobile at modest temperature. This unique property of GIC's give us a possibility of create a quasi-2d system.

The key effort for obtaining a 2D intercalant layer is to eliminate the correlations between the intercalants in different layers, and to reduce the role of the substrate potential field modulation. To eliminate the correlations between the intercalants in different layers, one can increase the distance between them, i.e. increase the stage number. To reduce the role of the graphite layer potential, one can heat the system so that the potential energy imposed on the intercalant can be compensated for by its high thermal energy. However in the ternary alkali metal K-NH₃ intercalated GIC K(NH₃)_{4.33}C₂₄, a 2D layer is achieved by the co-intercalation of NH₃ into the stage 2 binary potassium intercalated compound KC₂₄. The intercalation of NH₃ into a K-intercalated GIC serves two purposes: (1) it increases the intercalant-intercalant or guest-guest (G-G) interaction within a layer to reduce the role of the guest-host (G-H) interaction. This is possible because ammonia is well known as a strong solvent for alkali metals in the 3D case¹¹ where K atoms will immediately be ionized in the highly polarizable ammonia liquid. Upon the insertion of NH₃ into a K

occupied intercalant layer, the strong affinity of K to NH_3 introduces a competition with the carbon layer to bind K^+ . Consequently the interaction between K and carbon is reduced as evidenced by the charge back transfer observed in $\text{K}(\text{NH}_3)_{4.33}\text{C}_{24}$ ^{12,13} compounds. Notice that because of the addition of one more interaction, i.e. the K- NH_3 interaction, the role of the K-C interaction is reduced even without reduction of K-C interaction strength. (2) Since the strong interaction of K- NH_3 , the structure of each intercalant layer is dominated by G-G interactions which result in a liquid structure at room temperature. This leaves the interaction between intercalants in different layers limited to an average effect, thus the correlations between the intercalant layers are absent even in a stage 1 $\text{K}(\text{NH}_3)_{4.33}\text{C}_{24}$ where intercalant layers are only one graphite layer apart. This is the requirement for a 2D system.

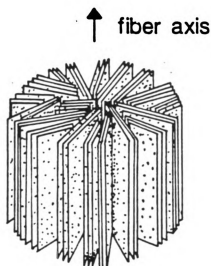
In the first part of this thesis, the experimental verification of such 2D metal-ammonia liquid solution structure is presented. From that we conclude that potassium-ammonia layers in the $\text{K}(\text{NH}_3)_{4.33}\text{C}_{24}$ form a 2D 4-fold coordinated liquid which is the 2D structural analogue of the well known 3D potassium-ammonia solutions. At the time of writing this overview, other experiments such as quasi-elastic neutron scattering¹⁴ have reconfirmed the structure which was deduced in this work. Additionally our recent work on the electrical resistivity¹⁵ and optical reflection and transmission properties¹⁶ of $\text{K}(\text{NH}_3)_x\text{C}_{24}$ reveals that it

is also the electronic analogue of the corresponding 3D metal-ammonia solution. i.e. it also shows a 2D Mott type metal-insulator transition.

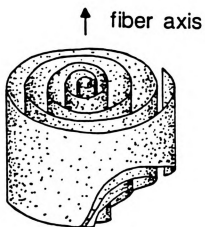
The second part of this thesis deals with the study of graphite fiber compounds.

Currently graphite fibers are made by two techniques: (1) the graphitization of precursor material such as pitch, polyacrylonitrile (PAN), rayon fibers at high temperature¹⁷, and (2) chemical vapor deposition of carbon onto microscopic carbon filaments¹⁸. These two techniques yield two structurally different fiber products. The fiber made by first technique consists of many graphite ribbons micrometer length and several tens to several hundreds of angstrom thick. These graphite ribbons are intertwined in such a way that statistically the graphite basal planes are aligned along the radial directions of the fiber as schematically shown in Fig. 3(a). The second technique produces fibers in which the graphite layer is wrapped around the axis of the fiber to form an onion like cylindrical structure shown in Fig. 3(b). Since many foreign species can be readily intercalated into the graphite as mentioned in the paragraphs above, insertion of many reactants into graphite fibers can be also achieved, although the threshold for the reaction to form a fiber compound is often significantly higher than that for bulk graphite compounds.

Systematic study on these fiber compounds has only begun in last few years.^{19,20} While most of the efforts have been devoted to the practical aspects of these compounds such as their high mechanical strength etc., the fundamental physical basis for many properties of



(a)



(b)

Fig. 3. (a) A schematic illustration of the structure of pitch based graphite fiber. The basal planes of the graphite layers are statistically aligned in the radial directions, and the \vec{c} -axes of the graphite planes are tangential. (b) A schematic illustration of the structure of vapor grown graphite fiber. The \vec{c} -axes of the graphite planes point radially outward.

these compounds has not been established. For example, it is found experimentally that the electrical properties such as electrical resistivity of graphite fiber can be improved by adding species such as Br or CuCl_3 , but the understanding of mechanism for such improvement is still, to our knowledge, minimal and too empirical. Therefore our efforts to study these fiber compounds have been centered on trying to elucidate the physical basis for their many interesting properties.

From studies of bulk GIC's, we know that properties such as electrical resistivity depend critically on the the local chemical environment^{20,21} and local structure^{20,21} of both the intercalant and the host graphite. Therefore, a knowledge of the microscopic scale chemical compositional distribution and structure are essential to any real understanding of the macroscopic properties. Since graphite fiber intrinsically lacks the uniformity of the structure found in its corresponding bulk counterpart, the detection and characterization of microscopic level chemical compositional distribution and structure would be especially important to understand any macroscopic level property. Guided by this thought, we present in the second part of this thesis a study on the relation between the microscopic chemical distribution and the macroscopic resistance of unique fiber compounds, i.e. residue brominated pitch based graphite compounds. The microscopic properties are probed by using a field emission scanning transmission electron microscope (FE-STEM), since the scale involved are in the range of several tens of angstroms to several micrometers. We also attempted to develop a phenomenological theory to couple the microscopic and macroscopic properties in such fiber compounds, and used it to explain

the resistance changes in two different phases of brominated pitch based graphite fibers.

Finally let me briefly mention that the special morphology of graphite fibers sometimes can provide a convenient experimental system. An example of this fiber application is our recent a-axis resistance measurement on $K(NH_3)_x C_{24}$ to study the 2D metal-insulator transition^{15,16} using a vapor grown graphite fiber whose structure is shown in Fig. 3(b). The fiber was chosen because of its large aspect ratio.

References list of overview:

1. S.A. Solin, Adv. Chem. Phys. 49, 455(1982).
2. S.A. Safran, Phys. Rev. Lett. 44, 937(1980).
3. R. Clarke, N, Casswell, and S.A. Solin, Phys. Rev. Lett. 42, 61(1979).
4. D.P. DiVincenzo, C.D. Fuerst, and J.E. Fisher, Phys. Rev. B. 29, 1115(1984).
5. G. Kirczenow, Phys. Rev. Lett. 49, 1855(1982).
6. H. Zabel, in Ordering in Two Dimensions, edited by S.K. Sinha, (North Holland, New York, 1980), p61.
7. G. Reiter, and S.C. Moss, Phys. Rev. B 33, 7209(1986).
8. F. Rousseaux, R. Moret, D. Guerard, P, Lagrange, and M. Lelaurain, in Proceedings of International Symposium on Graphite Intercalation Compounds, Tsukuba, Japan, 1985. [Synth. Met. 12, 45(1985)].
9. S.C. Moss, G. Reiter, C. Thompson, J.L. Robertson, J.D. Fan, and K. Ohshima, in Extended Abstracts of Graphite intercalation Compounds Section of Fall MRS Meeting, 1986, (MRS, Pittsburgh, 1986).
10. D.E. Nixon and G.S. Parry, J. Phys. C, 2, 1732(1969).
11. J.C. Thompson, Electrons in Liquid Ammonia (Clarendon, Oxford,1976).
12. B.R. York, and S.A. Solin, Phys. Rev. B, 31, 8206(1985).
13. R.M. Fronko, H.H. Resing, T. Tsang, X.W. Qian, and S.A. Solin, to be published in J. Chem. Phys., [See Appendices].
14. Y.B. Fan, S.A. Solin, D. Newman, H. Zabel, and J.J. Rush , Phys.Rev. B. to be published.

15. Y.Y. Huang, X.W. Qian, S.A. Solin, J. Heremans, and G.G. Tibbets in Proceedings of NATO Summer School for Advanced Science and Technology, 1986, edited by M.S. Dresselhaus, (Plenum, New York, 1986), [See Appendices].
16. Y.Y. Huang, Y.B. Fan, S.A. Solin, J.M. Zhang, P.C. Eklund, J. Hermans and G.G. Tibbets, submitted to Phys. Rev. Lett.
17. L.S. Singer, in Extended Abstracts of Graphite Intercalation Compounds Section in Fall MRS meetings, 1986, (MRS, Pittsburgh, 1986).
18. G.G. Tibbets, C.P. Beets JR. and C.H. Olk in Extended Abstracts of Graphite Intercalation Compounds Section of Fall MRS meetings, 1986 (MRS, Pittsburgh, 1986).
19. See, for example, Extended Abstracts of Graphite Intercalation Compounds Section of Fall MRS Meeting, 1986, (MRS, Pittsburgh, 1986).
20. See, for example, the review article by M.S. Dresselhaus, and G. Dresselhaus, Adv. in Phys. 30, 130(1980).
21. D.M. Hwang, X.W. Qian, and S.A. Solin, Phys. Rev. Lett. 53, 1473(1984).

PART I

STRUCTURAL PROPERTIES OF POTASSIUM-AMMONIA LIQUIDS IN GRAPHITE

I. Introduction

Metal-ammonia solutions were first intercalated into graphite several decades ago by Rudorff and Schultze,¹ the focus of whose interest was primarily chemical. Interest in metal-ammonia graphite intercalation compounds (GIC's) remained dormant until the recent burst of attention given to such compounds by Solin and coworkers.²⁻⁶ That attention was motivated in part by the expectation that the metal ammonia liquid in metal-ammonia GIC's might be the two-dimensional (2D) structural analogue of bulk three-dimensional (3D) metal-ammonia solutions which are one of the classic systems that have been employed to date to study the metal-insulator transition.⁷ Current interest in metal-ammonia GIC's was also stimulated by the suspicion that they might be novel systems with which to study the effects of dimensionality on localization⁸ and the metal-insulator transition in the crossover regime between 2D and 3D behavior.

Our initial studies of the structural properties of the potassium ammonia GIC,⁹ $\text{K}(\text{NH}_3)_{4.33}\text{C}_{24}$ have confirmed that the K-NH_3 liquid in that compound is indeed the 2D structural analogue of a bulk 3D K-NH_3 solution. Preliminary reports of these initial studies have been published^{9,10} and the purpose of this paper is to provide an in-depth presentation of the experimental and theoretical methods used to deduce the complex structure of the K-NH_3 2D liquid in graphite. Before proceeding, however, it will be useful to briefly summarize the experimental and theoretical information which has been acquired to date on the $\text{K}(\text{NH}_3)_x\text{C}_{24}$, $0 \leq x \leq 4.38$, system and which will provide essential input for the structural analysis which we present below.

The methods used by Rudörff and coworkers¹ and by Solin and coworkers^{2,3} to prepare metal-ammonia GIC's are quite different, and the resultant compounds produced by each method are distinct. Nevertheless, the synthesis of all $K-NH_3-C$ compounds produced to date can be understood in terms of the generalized Gibbs phase diagram¹¹ for the ternary system as represented by an equilateral triangle with K, NH_3 , and C at the vertices.⁶ Details of sample preparation for the specimens studied here will be given later (section II), but the description of current results, including those reported here pertain to samples prepared by the method of York and Solin,³ i.e. vapor phase ammoniation of the stage-2 binary GIC KC_{24} . [A stage n GIC is one in which every pair of nearest neighbor guest layers, e.g. the $K-NH_3$ liquid layer, are separated by n host carbon layers in a stacking sequence that exhibits long-range C-axis order perpendicular to the graphite basal planes.¹²]

The ammoniation of KC_{24} by NH_3 vapor to form $K(NH_3)_x C_{24}$, $0 \leq x \leq 4.38$ corresponding to NH_3 pressures in the range 10^{-13} torr $< P_{NH_3} \leq 9.5$ atm. has been extensively discussed elsewhere.^{3,6,9} It is sufficient for our purpose here to note that the room temperature absorption isotherm exhibits two plateau regions, each of which is initiated by a sharp rise in absorption over a very small change in pressure. These absorption steps occur at an ammonia pressure, P_{NH_3} , of $\approx 10^{-3}$ atm. and ≈ 1 atm., respectively, and the latter corresponds to a stage-2 to stage-1 phase transition.³ In that transition the system evolves from one where every second gallery contains potassium (layer stoichiometry KC_{12} , bulk stoichiometry KC_{24}) with a small amount of ammonia (composition = $K(NH_3)_{.03}C_{24}$) to one where every gallery is occupied by potassium (layer

stoichiometry KC_{24} , bulk stoichiometry KC_{24}) and an excess of ammonia (composition $\approx K(NH_3)_{4.3}C_{24}$). For $P_{NH_3} \geq 1$ atm. the system is essentially pure stage 1, and at $P_{NH_3} = 9.5$ atm. it acquires a composition of $K(NH_3)_{4.33}C_{24}$. It is this "saturated" compound which we focus on here.

Proton nuclear magnetic resonance (NMR) measurements have been carried out on $K(NH_3)_{4.33}C_{24}$ ⁴ and together with x-ray studies^{2,3,9} reveal several key features of the motions of the ammonia molecules in the graphite galleries and of their local orientations relative to the carbon layers, an example of which is depicted in Fig. 1.1. First, it is clear that the NH_3 molecules form only monolayers in the graphite galleries and that at room temperature they are rotating rapidly on the NMR time scale. They are also translating rapidly as are the K^+ ions. Thus, the $K-NH_3$ system exhibits liquid-like behavior although rapid hopping diffusion on lattice sites cannot be ruled out by the NMR measurements. More specifically, the NH_3 molecules are spinning rapidly about their 3-fold axis [C_3 in Fig. 1.1] which is tilted with respect to and precessing about the graphite c-axis [C in Fig. 1.1]. Moreover, the average tilt angle $\langle \alpha \rangle$ between the graphite c-axis and ammonia C_3 axis is, on the basis of both NMR⁴ and x-ray⁹ measurements, approximately 77° and the tilt angle α fluctuates dynamically during the precessional motion of the $NH_3 C_3$ axis. In addition to proton NMR studies, carbon 13 NMR studies¹³ have also been carried out on $K(NH_3)_{4.33}C_{24}$ and these reveal that the samples are indeed stage one, i.e. there is only one type of average local environment for the NH_3 molecule in the graphite gallery.

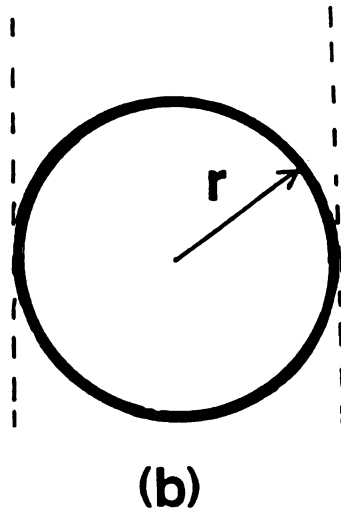
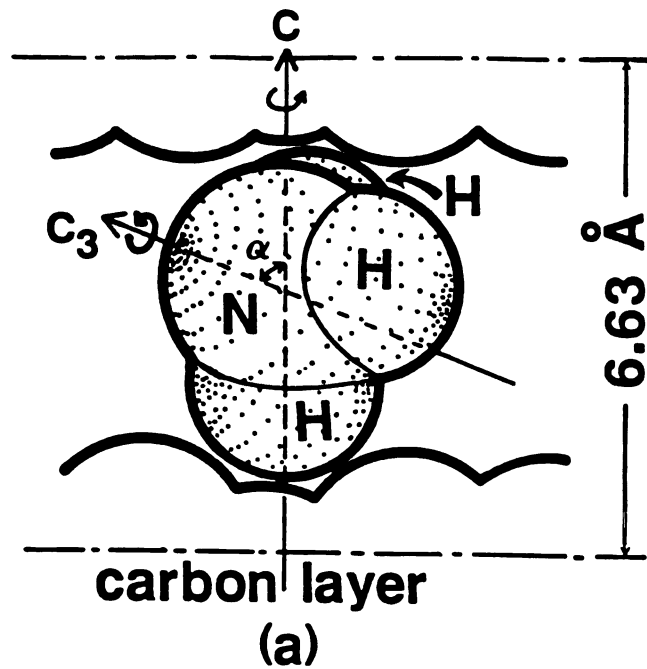


Fig. 1.1. (a) Schematic scaled diagram of the ammonia molecule sandwiched between carbon planes. The tilt angle between the molecular C_3 axis and the graphite c axis is denoted by α . (b) Planar projection of the ammonia molecule showing the resulting "hard" disc of radius r .

Very recently elastic, inelastic, and quasielastic neutron scattering studies of $\text{K}(\text{NH}_3)_{4.3}\text{C}_{24}$ and the deuterated analogue $\text{K}(\text{ND}_3)_{4.3}\text{C}_{24}$ have been carried out¹⁴ and the preliminary quasielastic measurements indicate two distinct diffusional motions, one presumably due to translation and one due to rotation in agreement with NMR results. Other recent measurements of the optical⁵ and electronic¹⁵ properties of the $\text{K-NH}_3\text{-C}$ system confirm, respectively, the staging phase transition and the stage-1 character of the "saturated" compound, but shed no additional light on the structural properties of the K-NH_3 liquid.

The information established in this introductory section will be followed by a description in section II of our experimental results and of the novel experimental methods which we used to measure the in-plane diffuse scattering from $\text{K}(\text{NH}_3)_{4.33}\text{C}_{24}$. In section III, the theoretical methods used to calculate the in-plane diffraction pattern are described. The computer generated structural models to which the theoretical methods are applied are described and discussed vis-à-vis experimental results in section IV. Section V contains a discussion of the radial distribution function deduced from the structural models we have considered while our concluding remarks and acknowledgments are presented in sections VI and VII, respectively.

II. Experimental Techniques and Results

Specimens of KC_{24} were prepared from highly-oriented pyrolytic graphite (HOPG)¹⁶ using the standard two-bulb method¹⁷ and pyrex ampoules. Stage-2 purity was verified by (00 ℓ) x-ray diffraction studies which, together with the in-plane measurements reported here, were carried out using $\text{MoK}\alpha$ radiation from a Rigaku 12kw rotating anode

source coupled through a vertically bent graphite monochromator to a Huber 4-circle diffractometer that housed a NaI detector.

The diffuse in-plane scattering from $K(NH_3)_{4.33}C_{24}$ was very weak and was masked by the diffuse scattering from the pyrex ampoules in which reactive GIC specimens are normally contained.¹² Moreover, because the pressure of the ammonia vapor surrounding the specimen was ≈ 10 atm. it was not feasible to reduce the diffuse scattering from the pyrex envelope by expanding its diameter and/or thinning its wall.¹⁸ Therefore, a sample cell was constructed from a very thin wall ($< .005''$) x-ray transparent aluminum can epoxied to a pyrex tube. The aluminum can not only sustained the high NH_3 pressure, but when it was machined from a single crystal and subsequently annealed at $\approx 500^\circ C$ it yielded a quasi-single crystal diffraction pattern that minimally interfered with the diffuse scattering from the specimen.

The in-plane as-recorded diffraction patterns which we obtained were corrected^{19,20} for several instrumental artifacts in the following way: Let $I_{\text{exp}\perp}(q)$ be the observed in-plane diffraction pattern. This contains Bragg reflections associated with both the aluminum sample can and the ordered carbon layers. A reference pattern acquired from a sample free region of the aluminum can was recorded, appropriately scaled to, and subsequently subtracted from $I_{\text{exp}\perp}(q)$. The Bragg peaks associated with the carbon layers were removed (for clarity) from the resulting pattern to yield $I'_{\text{exp}\perp}(q)$ which is the observed diffuse scattering. The pattern $I'_{\text{exp}\perp}(q)$ was further corrected for absorption and the Lorentz polarization factor to yield $I_{\perp}'(q)$ as follows:

$$I_{\perp}(q) = I'_{\text{exp}\perp}(q) [T/\cos\theta \exp(-\mu T/\cos\theta)]^{-1} \times \\ [(1 + \cos^2 2\theta' \cos^2 2\theta)/(1 + \cos^2 2\theta')]^{-1} . \quad (1)$$

Here, T is the sample thickness, μ is the effective absorption coefficient, θ is the diffraction angle, and θ' is the graphite monochromator diffraction angle for the (004) MoK α reflection. The corrected diffuse scattering function $I'_{\perp}(q)$ was scaled to oscillate about the incoherent scattering contribution

$$I_{\text{Inc}}(q) = \sum_{\text{uc}} f_m^2 + i(m) \quad (2)$$

at high q and from this scaling the ordinate scale, in electron units, was established. In Eq. (2), f_m is the q -dependent atomic scattering factor of the m^{th} atom, $\text{uc} \rightarrow$ unit of composition which in our case is $\text{K}(\text{NH}_3)_{4.33}$ and $i(m)$ is the Compton-modified scattering from the K, N, H, and C atoms.

The results of the application of the above-described procedure to the experimentally measured $I_{\text{exp}\perp}(q)$ with $q \perp c$ are shown in Fig. 1.2 together with the corresponding incoherent scattering contribution. We have also measured a c^* scan¹² to establish the degree of correlation between individual K-NH₃ layers in successive galleries. The results of this scan are shown in Fig. 1.3 which represents the as-recorded uncorrected data. For the scan given in Fig. 1.3, data corrections are not required to extract the information we seek.

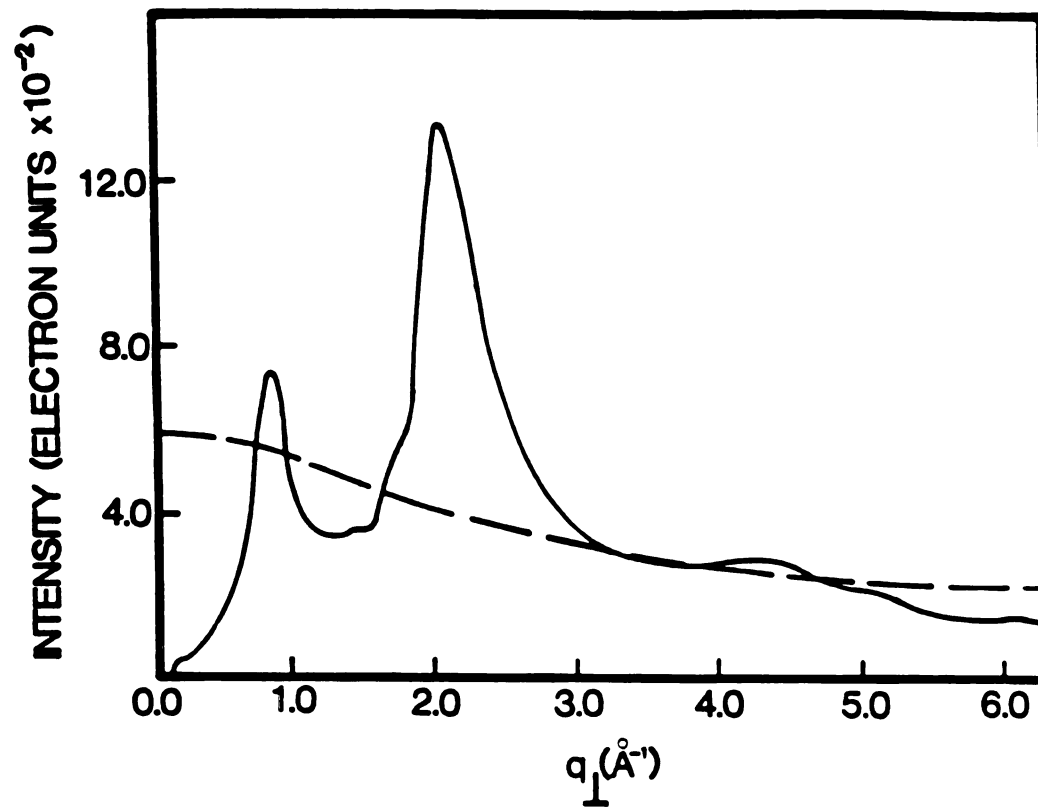


Fig. 1.2. The diffuse in-plane scattering $(\vec{q} \cdot \vec{c}) [I(q)]_{\text{exp}}$ from $\text{K}(\text{NH}_3)_{4.33}\text{C}_{24}$ (solid line) and incoherent contribution from the aluminum sample can and from the crystalline carbon planes have been removed for clarity. The dash line represents the incoherent scattering contribution.

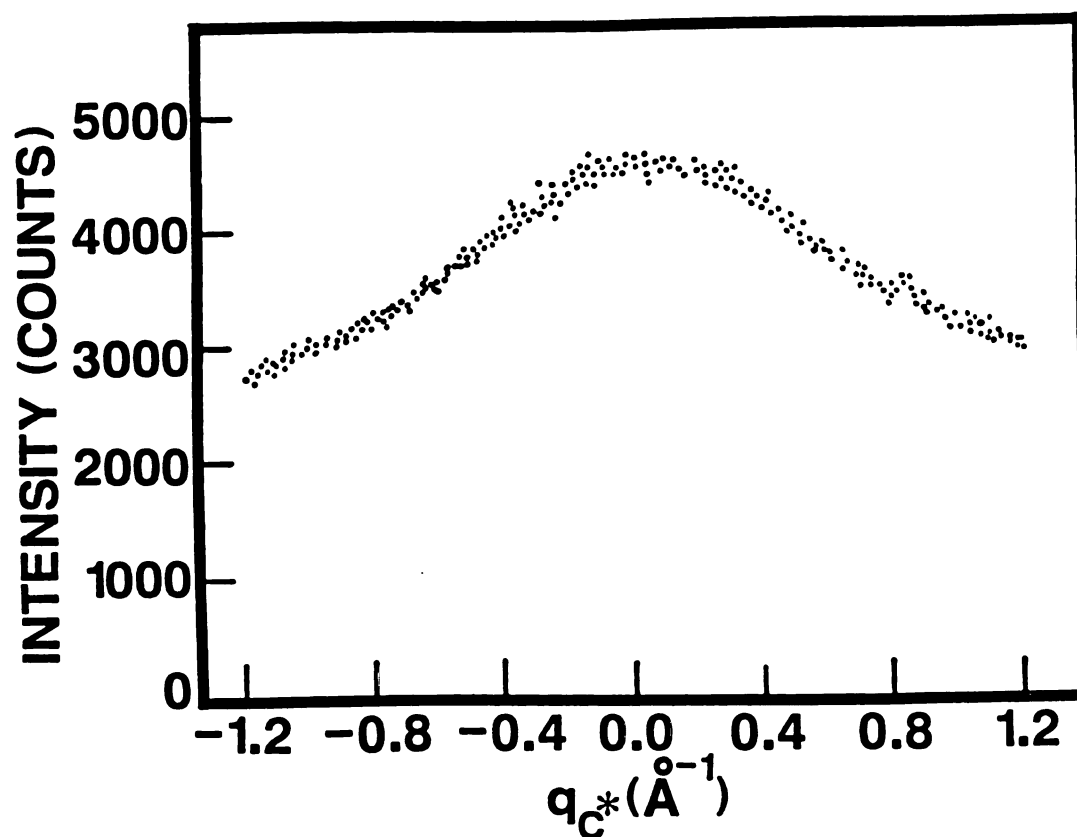


Fig. 1.3. The diffuse C^* scattering ($q_{\perp} = 0.88 \text{ \AA}^{-1}$, $-1.2 \text{ \AA}^{-1} < q_c^* < 1.2 \text{ \AA}^{-1}$) from $K(\text{NH}_3)_{4.33}\text{C}_{24}$. The small peak at $q_c^* = 0.80 \text{ \AA}^{-1}$ is due to a surface contaminant of residual KC_8 . The acquisition time per channel was 32 sec.

III. X-Ray Scattering from Stacked 2D Liquid Layers

Traditionally, there have been two basic approaches taken to analyze data of the type shown in Fig. 1.2. Some authors prefer to use a Bessel function back transform of $I'_{\perp}(q)$ to obtain the in-plane radial distribution function (RDF).²¹ While this approach has been reasonably successful when applied to monatomic 2D²¹ or 3D²⁰ disordered systems it is, in our opinion, seriously deficient for multiatomic systems such as the K-NH₃ liquid in graphite. This deficiency results from the well-known difficulty of deconvolving the pair contributions (e.g. K⁺-K⁺, K⁺-NH₃, and NH₃-NH₃) to the total RDF.²⁰

Another approach, and the one that we believe is superior for multiatomic systems, is to generate a real space model of the structure of the disordered system and from the resultant atomic coordinates calculate the diffraction pattern which is then compared directly to the observed pattern in order to assess the validity of the model. Although this method has obvious advantages, the reader should be cautioned to consider a "good fit" to the experimental data as necessary, but not in and of itself sufficient to verify the correctness of the structural model of choice.²² Only when the diffraction data is taken, together with other experimental evidence (e.g. NMR), can the correctness of a particular structural model be confidently established.

Having chosen the methodology which we will apply to the data of Fig. 2.2, we now address the calculational techniques which will be used to compute the diffraction patterns of the structural models that we have constructed (see below).

The cross-section for x-ray scattering from a collection of atoms or molecules, with x-ray momentum transfer $\vec{h}q$, is

$$\sigma(\vec{q}) = \sigma_T(\vec{q})I(\vec{q}) \quad (3)$$

where $\sigma_T(\vec{q})$ is the Thomson cross-section and $I(\vec{q})$ is the structure function

$$I(\vec{q}) = \left| \sum_k f_k(\vec{q}) e^{i\vec{q} \cdot \vec{r}_k} \right|^2. \quad (4)$$

Here \vec{r}_k is the position of the k^{th} atom and $f_k(\vec{q})$ is the Fourier transform of the electron density of the k^{th} atom.

In our model calculations for x-ray scattering from potassium and ammonia intercalated in graphite we used spherically symmetric form factors $f_K(q)$ and $f_{\text{NH}_3}(q)$. At $q = 0$ the function $f_K(q)$ is equal to the number of electrons in the atom. For the potassium form factor $f_K(q)$ we renormalized the function so that $f_K(0)$ is 18 rather than 19 because the potassium is almost completely (singly) ionized. Similarly, the form factor for NH_3 was assumed isotropic and was normalized so that $f_{\text{NH}_3}(0) = 13$.

For atoms intercalated in graphite, the positions \vec{r}_k are specified by the gallery level n and position of the atom in that layer α . That is, the index $k = (n\alpha)$ and the position is

$$\vec{r}_{n\alpha} = \hat{c}^* n L + \vec{\rho}_{n\alpha} \quad (5)$$

where \hat{c}^* is a unit vector in the C^* direction, L is the spacing between layers, and $\vec{\rho}_{n\alpha}$ is a two-dimensional position vector. The in-plane structure function $I_{\perp}(\vec{q})$, which is $I(\vec{q})$ with $\vec{q} \perp \hat{c}^*$, can be written

$$I_{\perp}(\vec{q}) = \sum_n \sum_{\alpha\alpha'} f_{n\alpha}(q) f_{n\alpha'}^*(q) e^{i\vec{q} \cdot (\vec{\rho}_{n\alpha} - \vec{\rho}_{n\alpha'})}$$

$$+ \sum_{\substack{n, n' \\ (n \neq n')}} \sum_{\alpha, \alpha'} f_{n\alpha}(q) f_{n'\alpha'}^*(q) e^{i\vec{q} \cdot (\vec{\rho}_{n\alpha} - \vec{\rho}_{n'\alpha'})} \quad (6)$$

In Eq. (6) the first term is the intralayer interference, and the second term is the interlayer interference. If there is no correlation between the atomic positions in different layers, then the interlayer interference term is identically zero. In that case, $I_{\perp}(\vec{q})$ is the structure function of a purely two-dimensional system.

Of course, if there is any strong correlation between the atomic positions in different layers, then the interlayer interference term does contribute to $I_{\perp}(\vec{q})$. As an extreme example, suppose the distributions of the atoms in N of the layers is the same except for an overall displacement of the layer in a direction perpendicular to \hat{c}^* . That is, assume that the atomic positions in these N layers are of the form

$$\vec{\rho}_{n\alpha} = \vec{\rho}_{\alpha} + \vec{R}_n, \quad (7)$$

where \vec{R}_n is the displacement of the n^{th} layer, and $\vec{\rho}_{\alpha}$ is independent of n . Then the contribution of these N layers to the structure function $I_{\perp}(\vec{q})$ would be

$$I_{\perp}(\vec{q}) = F_N(\vec{q}) \sum_{\alpha\alpha'} e^{i\vec{q} \cdot (\vec{\rho}_{\alpha} - \vec{\rho}_{\alpha'})} f_{\alpha}(q) f_{\alpha'}^*(q) \quad (8)$$

where

$$F_N(\vec{q}) = \sum_{n, n'=1}^N e^{i\vec{q} \cdot (\vec{R}_n - \vec{R}_{n'})} \quad (9)$$

For example, if the \vec{R}_n 's are distributed randomly with $|\vec{R}_n| \leq d$, then the expected value of $F_N(\vec{q})$ is

$$F_N(\vec{q}) = N + N(N-1) \left(\frac{J_1(qd)}{\frac{1}{2}qd} \right)^2. \quad (10)$$

The second term in Eq. (10), which is the effect of the interlayer interference, is significant for $N > 1$ and a maximum displacement $d \leq 1/q$.

In order to establish the degree of interlayer correlation it is customary to measure a c^* scan in which a diffraction pattern is measured with $\vec{q} = (\vec{q}_\perp, \vec{q}_{c^*})$ with q_\perp fixed, but $q_\perp \neq 0$, and q_{c^*} variable over some range $-Q < q_{c^*} < +Q$. The structure function for such measurements can be written as

$$\begin{aligned} I(\vec{q}) = & \sum_n \sum_{\alpha, \alpha'} e^{i\vec{q}_\perp \cdot (\vec{\rho}_{n\alpha} - \vec{\rho}_{n\alpha'})} f_{n\alpha}(\vec{q}) f_{n\alpha'}^*(\vec{q}) \\ & + \sum_{\substack{n, n' \\ (n \neq n')}} e^{iq_{c^*}(n-n')L} \sum_{\alpha, \alpha'} e^{i\vec{q}_\perp \cdot (\vec{\rho}_{n\alpha} - \vec{\rho}_{n'\alpha'})} f_{n\alpha}(\vec{q}) f_{n'\alpha'}^*(\vec{q}). \end{aligned} \quad (11)$$

Again the second term, which is the q_{c^*} -dependent term, represents the effect of interlayer interference. If there were a correlation of the type represented by Eq. (7), then the interlayer interference term of $I(\vec{q})$ would be

$$\sum_{\substack{n, n' \\ (n \neq n')}} e^{iq_{c^*}(n-n')L} e^{i\vec{q}_\perp \cdot (\vec{R}_n - \vec{R}_{n'})} \sum_{\alpha, \alpha'} e^{i\vec{q}_\perp \cdot (\vec{\rho}_\alpha - \vec{\rho}_{\alpha'})} f_{n\alpha}(\vec{q}) f_{n'\alpha'}^*(\vec{q}).$$

For strong correlations, the factor $e^{i\vec{q}_\perp \cdot (\vec{R}_n - \vec{R}_{n'})}$ is approximately 1; then the major n -dependence in the summand is from the factor $e^{iq_{c^*}(n-n')L}$, so the interlayer interference term would produce diffraction peaks at $q_{c^*} = 2\pi\nu/L$ where ν is an integer.

In the absence of such interlayer interference, the 2nd term in Eq. (11) is identically zero and one expects to observe, for all values of q_\perp such that $\vec{q} = (\vec{q}_\perp, q_{c^*})$ does not intersect a Bragg reflection of the host graphite structure, a monotonically decreasing intensity on either side of $q_{c^*} = 0$ due to the \vec{q} dependent form factor contributing to the first term of Eq. (11). This is exactly what is observed in the $q = 0.88 \text{ \AA}^{-1}$, q_{c^*} scan of $\text{K}(\text{NH}_3)_{4.33}\text{C}_{24}$ which is shown in Fig. 1.3. This particular scan across the "ridge" of the first and most pronounced peak in $I_\perp(q)$ traverses a trajectory in q -space which is free from host lattice Bragg reflections. [Note that the very small peak at $q_{c^*} = 0.8 \text{ \AA}^{-1}$ in Fig. 1.3 is a Bragg reflection from a residual contaminant of KC_8 on the sample surface.] Therefore, we confirm and hereinafter assume that there is no correlation between the K-NH_3 liquid layers in different galleries of the carbon host. These x-ray observations have been independently confirmed by (20 ℓ) c^* neutron scattering scans¹⁴ which also show a monotonic decrease about $q_{c^*} = 0$.

In the absence of interlayer correlation, the in-plane structure function is the same as for a single layer,

$$I_\perp(\vec{q}) = \sum_{\alpha, \alpha'} f_\alpha(q) f_{\alpha'}^*(q) e^{i\vec{q} \cdot (\vec{\rho}_\alpha - \vec{\rho}_{\alpha'})}, \quad (12)$$

apart from the absolute magnitude. Furthermore, if the positions $\vec{\rho}_\alpha$ within the layer are disordered, as in a liquid, then $I_\perp(\vec{q})$ depends only on the magnitude of \vec{q} . In that case, we may average $I_\perp(q)$ over the directions of \vec{q} , with the result

$$I_\perp(q) = \sum_{\alpha, \alpha'} f_\alpha(q) f_{\alpha'}^*(q) J_0(q|\vec{r}_\alpha - \vec{r}_{\alpha'}|) . \quad (13)$$

This is the formula which we use to calculate the structure function in our model calculations. In those calculations the number of particles is 500 potassium atoms and 2165 ammonia molecules. This number is found to be sufficiently large that $I_\perp(\vec{q})$, computed from Eq. (13), is almost independent of the direction of \vec{q} . If a smaller collection of particles is used, then there is some dependence on the direction of \vec{q} , because the close packing of K-NH₃ clusters in our models (see section IV below) creates local ordering on a scale of approximately 50 K-NH₃ clusters. This local ordering produces preferred directions, and only when the number of particles is sufficient to produce a structure whose scale is much larger than the scale of the local ordering is the diffraction pattern independent of the direction of \vec{q} .

IV. Structural Models

In order to model the structure of the K-NH₃ liquid in the graphite galleries, we make several simplifying assumptions which are listed below:

1. The potassium ions and the NH₃ molecules are treated as hard infinitely thin discs oriented with their planes parallel to

the carbon planes and located at the mid-point of the gallery along the graphite C-axis.

2. The radii of the K^+ discs are identical and fixed at a value which is adjusted to give the best fit to the diffraction pattern consistent with the charge exchange to the graphite layer.
3. The radii of the ammonia discs are variable and vary with the tilt angle α according to a probability distribution that is related to the tilt angle distribution.
4. Where N ammonia molecules are bound to a K^+ ion in the liquid, the N-fold coordinated $K-NH_3$ cluster is symmetric. Thus, the lines connecting the center of the K^+ disc to each of the NH_3 discs in a cluster make equal angles of $2\pi/N$.
5. The computer-generated collection of $K-NH_3$ clusters and free NH_3 discs is assembled in such a way as to maximize the in-plane density.
6. The effect of the graphite substrate potential on the structure of the $K-NH_3$ liquid has been ignored.

Consider now the basis and justifications for these assumptions. Hard disc models have been applied with reasonable success to ascertain the structures of 2D disordered systems including the case of a cesium GIC, CsC_{24} .²³ Such models are justified in part because they remove the horrendous complications attendant to a calculation of the diffraction from a dynamic, irregularly-shaped 3D charge distribution (e.g. the diffusing ammonia molecule). In addition, ammonia is a reasonable candidate for disc representation because the H atoms are relatively invisible to x-rays.

We know from other studies^{3,4,9} that all of the K^+ ions are bound in clusters to NH_3 species. Moreover, there is evidence that the charge exchange parameter, f , is almost unity.³ Therefore, it is sensible to assign a fixed radius to all the potassium ions. The radius was chosen as $r_{K^+} = 1.46 \text{ \AA}$, a value greater than the ionic radius of 1.33 \AA ,²⁴ confirming that the potassium ion is not fully ionized. Other fixed values of r_{K^+} gave inferior fits to the experimental results.

As noted in the introduction, the NH_3 molecules in the graphite galleries are simultaneously spinning about their C_3 axes, precessing about the graphite C-axis, and rocking as the tilt angle α fluctuates. These motions are fast on the NMR time scale, $\approx 10^{-5} \text{ sec}$,²⁵ but infinitely slow on the x-ray time scale. Therefore, the x-ray pattern represents the diffraction from an ensemble of $K-NH_3$ layers, each with its own "frozen" configuration of K and NH_3 "discs". The polarization of the lone pair of electrons on the nitrogen atom of the NH_3 molecule by the positively-charged K^+ ion causes the NH_3 molecules to cluster around and tilt towards the ion (i.e. $\langle \alpha \rangle \neq 0$). While at any instant in time the tilt angle of a particular molecule in the specimen is fixed, there is a "static" distribution of those tilt angles between the values of $\alpha_{\min} = 0^\circ$ and $\alpha_{\max} = 90^\circ$. Corresponding to these are the effective radii of the NH_3 molecule, $r_{\min} = 1.3 \text{ \AA}$, the height of the molecule, and $r_{\max} = 2.0 \text{ \AA}$, the radius of the circle inscribing the centers of the three H atoms.

The distribution function $P(r)$ giving the probability of finding an NH_3 disc of radius r was modeled as a Gaussian with a cut on at r_{\min} and a cut off at r_{\max} . Thus

$$P(r) = A \exp[-(r - r_{\min})^2 / \sigma^2] \theta(r - r_{\min}) \theta(r_{\max} - r) \quad (14)$$

where A is a proportionality constant, $\theta(x)$ is a step function [$\theta(x) = 1$ if $x > 0$, $\theta(x) = 0$ if $x < 0$] and the parameter σ is related to the mean radius $\langle r_{\text{NH}_3} \rangle$ by

$$\langle r_{\text{NH}_3} \rangle = \frac{\int_{r_{\text{min}}}^{r_{\text{max}}} \exp[-(r - r_{\text{min}})^2/\sigma^2] r dr}{\int_{r_{\text{min}}}^{r_{\text{max}}} \exp[-(r - r_{\text{min}})^2/\sigma^2] dr} \quad (15)$$

Note from Eq. (14) that $P(r)$ is peaked at r_{min} . This reflects the fact that most of the molecules experience large tilt angles in analogy with bulk K-NH₃ solutions for which the axes of the 6 NH₃ molecules all point through the center of the K⁺ ion.⁷ In further analogy to the bulk K-NH₃ solutions which contain symmetric octahedral clusters we have assumed that the planar K-NH₃ clusters in the graphite galleries are also symmetric [e.g. item 4 of our assumptions above].

In any hard sphere or hard disc model, the assembly procedure (algorithm) used is designed to maximize the contact between the component species.²⁶ This is equivalent to maximizing the areal density for planar models; accordingly, we designed our structure generation routines to maximize density. In addition, to simplify our procedures we ignored the substrate potential as noted above. While this approach cannot be justified a priori, it is retroactively justified by the results which we obtain.

Using the assumptions specified above, a structural model of the K-NH₃ liquid layers in graphite was generated as follows. Each model was constructed from 500 K⁺ discs and 2165 NH₃ discs to satisfy the stoichiometry $\text{K}(\text{NH}_3)_{4.33}\text{C}_{24}$ where $2165/500 = 4.33$. For an N-fold model

exactly 500N molecules were bound symmetrically to K^+ ions to form N-fold coordinated clusters while the remaining 2165-500N molecules were assembled as spacer discs.

By way of example, consider the assembly of a 4-fold coordinated structural distribution illustrated in Fig. 1.4. First, a "pot" of 500 4-fold clusters was created by attaching 4 ammonia discs symmetrically to each K^+ disc. The radii of the 4 NH_3 discs in each cluster were randomly selected by the computer using the probability distribution function $P(r)$. A seed cluster was then moved to the center of the plane. Next, a random number generator made a decision to add either another 4-fold cluster or a single ammonia disc. The initial such decision was weighted by the factors $499/[2165 - 500(4) + 499] = .75$ and $[2165 - 500(4)]/[2165 - 500(4) + 499] = .25$, which represent the respective probabilities of selecting a cluster or a bare NH_3 disc from a combined pot containing 499 clusters and $2165 - 500(4) = 165$ bare NH_3 molecules. Subsequent decisions were always weighted by the remaining numbers of clusters and NH_3 discs in the combined pot so that the rare NH_3 discs were not expended too rapidly.

If a 4-fold cluster was chosen from the combined pot, the computer brought it into contact with the seed cluster through a series of small translations and rotations. Two kinds of rotation were involved, one around the center of the plane and the other around the center of the new cluster (see Fig. 1.4). The newly-added cluster was assembled in such a position that the distance between the center of the seed and of new cluster was minimized, to maximize the in-plane density. If, on the other hand, a single disc was chosen, the computer created a single NH_3 disc with a radius randomly selected using $P(r)$. This newly-generated

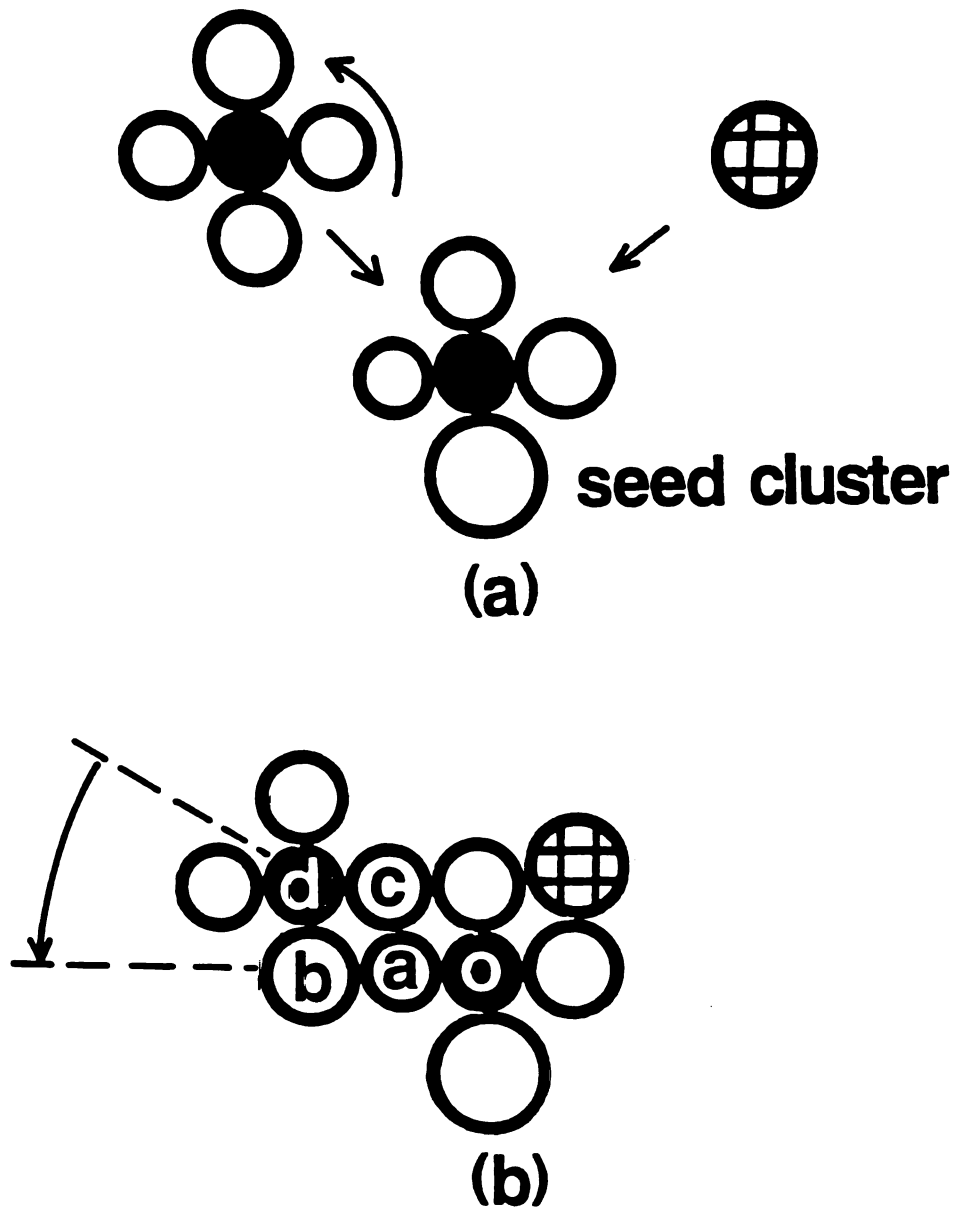


Fig. 1.4. (a) Schematic representation of mechanism used to computer generate a fourfold coordinated hard disc K-NH₃ liquid (see text). Arrows indicate the combined translation and rotation of the clusters which are close packed to the seed cluster. In the case of the packing of a single NH₃ disc, the arrow indicates translation only. (b) Close packing configuration of two fourfold clusters. The letters o, a, b, c, and d indicate positions which are relevant to the discussion in the text.

single NH_3 disc was moved in a series of small translations towards the center of the plane, and positioned in contact with the discs already assembled so as to maximize the in-plane density. Care was taken to prevent overlapping of the assembled discs. This procedure is also depicted in Fig. 1.4, and was repeated until all K^+ and NH_3 discs had been assembled. The central part (about one-sixth) of the resulting structure, which is close-packed and 4-fold coordinated, is shown in Fig. 1.5(a).

Using exactly the same method that was employed to construct the 4-fold structure, we also constructed a 3-fold coordinated structural distribution which consisted of 500 3-fold clusters and 665 single NH_3 discs. This structure is shown in Fig. 1.6(a). A 0-fold (uncoordinated) structure was also constructed by randomly selecting K^+ or NH_3 discs from the "pots" of 500 K^+ ions and 2165 NH_3 molecules starting with a K^+ seed. When subsequent selections yielded an NH_3 disc, its radius was randomly selected using $P(r)$ as described above. Both K^+ and NH_3 discs were translated to the existing assembly and placed in locations which maximized the density. The resultant 0-fold structure is shown in Fig. 1.7(a). For the purpose of further discussion we also show in Figs. 1.5b, 1.6b, and 1.7b the arrangements of only the K^+ ions in the 4-fold, 3-fold, and 0-fold coordinated distributions, respectively.

Equation (13) has been applied to the structures shown in Figs. 1.5a, 1.6a, and 1.7a, and the calculated diffraction patterns $I_{\perp}(q)$ are compared with the experimental measurement in Figs. 5c, 6c, and 7c, respectively. The only adjustable parameter used for these comparisons was a scale factor to optimize the fit at high q ($> 5 \text{ \AA}^{-1}$).

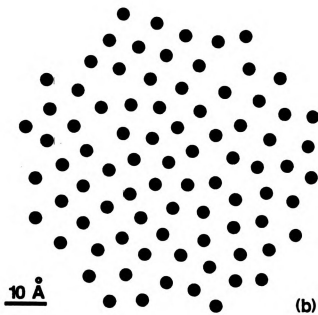
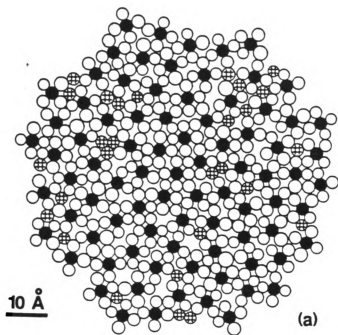


Fig. 1.5(a), (b).

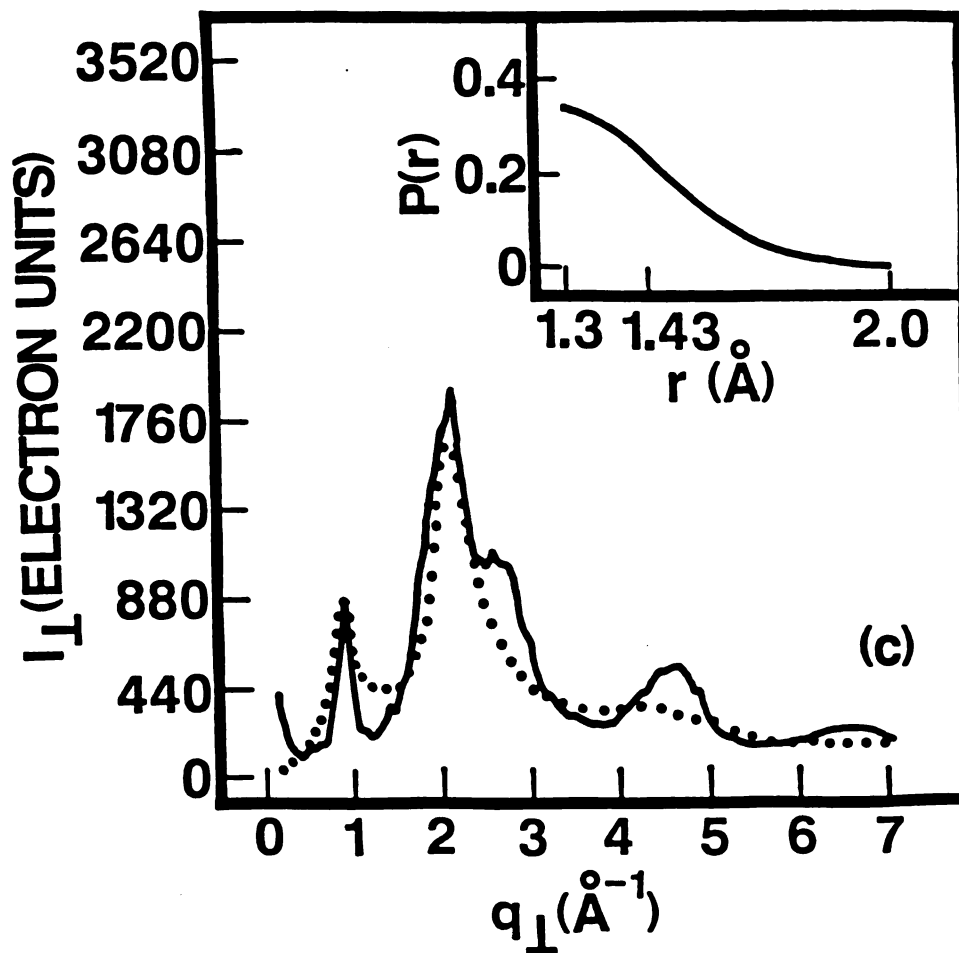


Fig. 1.5. (a) Section of the fourfold coordinated computer-generated distribution for the K-NH₃ liquid in K(NH₃)_{4.33}C₂₄. The K⁺ ions, bound NH₃ molecules, and bare NH₃ molecules are represented by solid circles, open circles, and checkered circles, respectively. (b) Configuration of K⁺ ions for the distribution shown in (a) above. (c) Diffuse in-plane x-ray scattering $I_{\perp}(q)$ (solid line) calculated using the fourfold coordinated distribution shown in (a) above and compared with the experimental measurement of $[I_{\perp}(q)]_{\text{exp}}$ (dots) reproduced from Fig. 1.2. Inset: The probability distribution $P(r)$ (see text) for NH₃ disc radii used to generate the distribution shown in (a) above. The parameters used to compute $P(r)$ were $r_{\text{min}} = 1.3 \text{ \AA}$, $r_{\text{max}} = 2 \text{ \AA}$, $\sigma = 0.23 \text{ \AA}$, and $r_{\text{K}^+} = 1.46 \text{ \AA}$, $\langle r_{\text{NH}_3} \rangle = 1.43 \text{ \AA}$.

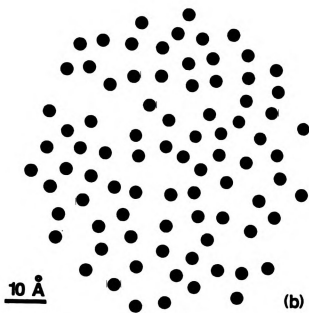
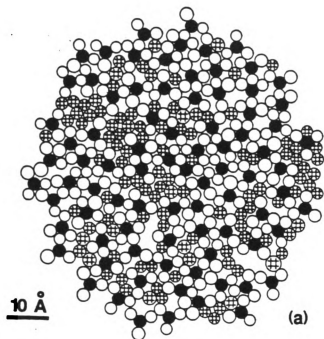


Fig. 1.6(a), (b).

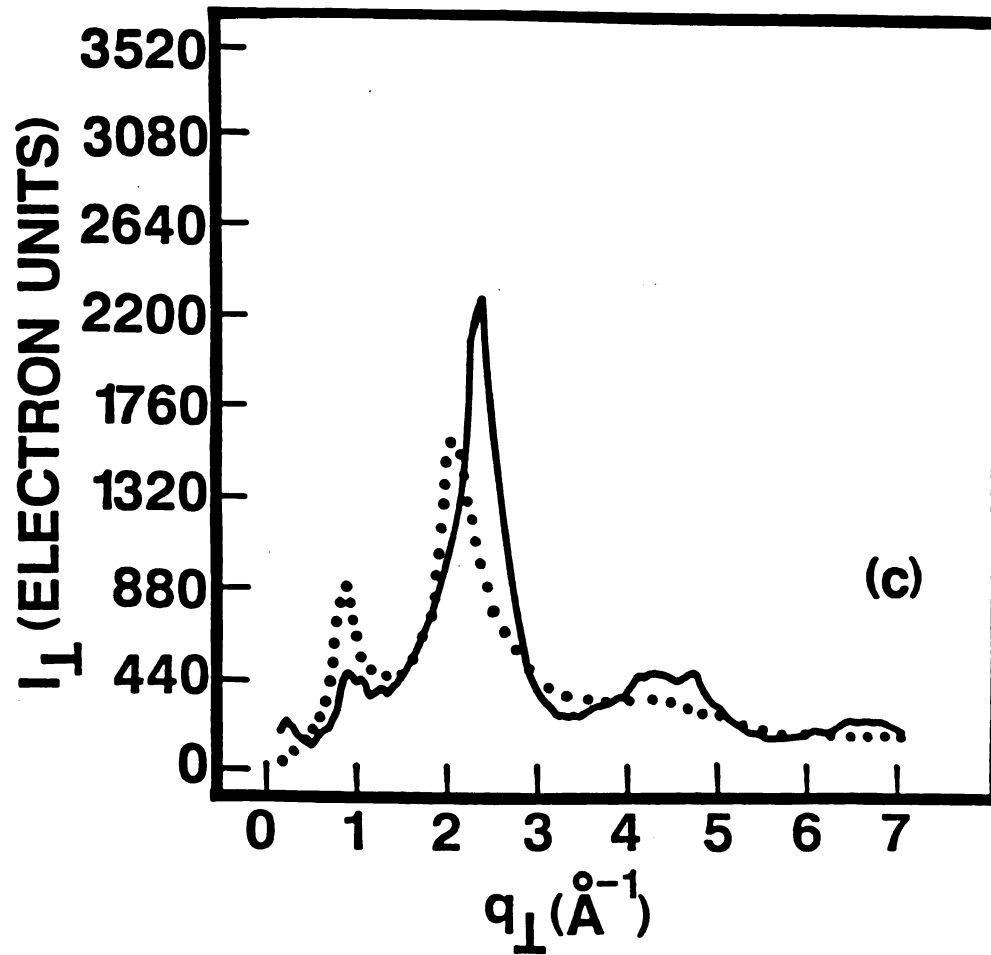


Fig. 1.6. Section of the threefold coordinated computer-generated distribution for (a) the K-NH_3 liquid in $\text{K}(\text{NH}_3)_{4.33}\text{C}_{24}$, (b) together with the resulting distribution of K^+ ions, and (c) a comparison of the corresponding calculated x-ray diffraction pattern with the experimental measurement of in-plane diffuse scattering. See the caption of FIG. 1.5 for an explanation of the symbols used and a listing of the relevant parameters.

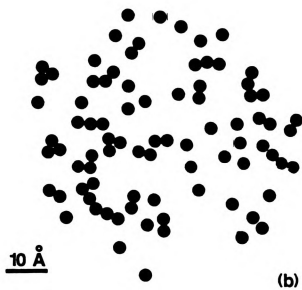
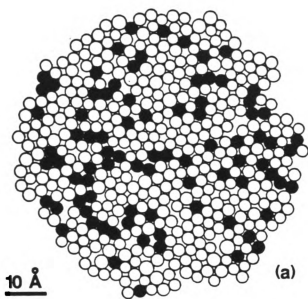


Fig. 1.7(a),(b).

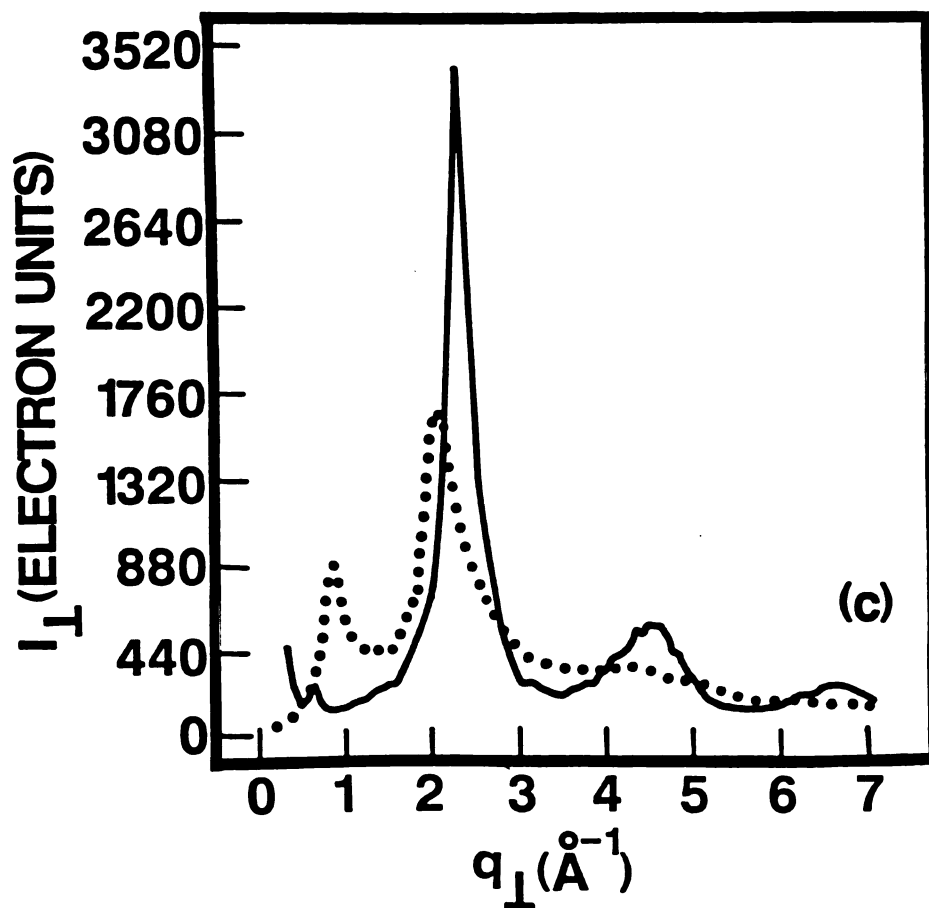


Fig. 1.7. Section of the zerofold coordinated computer-generated distribution for (a) the K-NH_3 liquid in $\text{K(NH}_3\text{)}_{4.33}\text{C}_{24}$, (b) together with the resulting distribution of K^+ ions and (c) a comparison of the corresponding calculated x-ray diffraction pattern with the experimental measurement of in-plane diffuse scattering. Open circles represent bare NH_3 molecules. All other symbols and relevant parameters are the same as those used in Fig. 1.5.

A comparison of Figs. 1.5c, 1.6c, and 1.7c reveals that the best fit is clearly obtained with the 4-fold coordinated distribution which accounts semiquantitatively for all of the observed features in the experimental diffraction pattern, and in particular, the peak at $q = 0.88 \text{ \AA}^{-1}$. This peak is a key, discerning feature of the diffraction pattern and can therefore be used as the major test for the model calculation. Notice that the 0.88 \AA^{-1} peak is very weak in the calculated pattern for the 3-fold structure (see Fig. 1.6c) and is totally absent in the calculated pattern of the 0-fold structure (see Fig. 1.7c). On the other hand, the 3-fold structure does provide the best fit for the $q > 2.0 \text{ \AA}^{-1}$ region, but the serious discrepancy at 0.88 \AA^{-1} is ground for rejecting 3-fold coordination as a dominant structural feature.

We can acquire a considerable degree of insight into the structural origins of various features in the experimental and theoretical diffraction patterns by decomposing the total calculated scattering intensity into three separate contributions from K^+-K^+ correlations, K^+-NH_3 correlations, and NH_3-NH_3 correlations. Thus

$$I_{\perp}(\vec{q}) = i_{\perp K^+-K^+}(q) + i_{\perp K^+-NH_3}(q) + i_{\perp NH_3-NH_3}(q) \quad (16)$$

where

$$i_{\perp K^+-K^+}(q) = \sum_{\substack{\text{all } K^+-K^+ \\ \text{pairs}}} |f_{K^+}(q)|^2 J_0(qr) \quad (17)$$

$$i_{\perp K^+-NH_3}(q) = \sum_{\substack{\text{all } K^+-NH_3 \\ \text{pairs}}} 2\text{Re}(f_{K^+}(q)f_{NH_3}^*(q))J_0(qr) \quad (18)$$

$$i_{\perp \text{NH}_3-\text{NH}_3}(q) = \sum_{\text{all NH}_3-\text{NH}_3 \text{ pairs}} |f_{\text{NH}_3}(q)|^2 J_0(qr) \quad (19)$$

These individual pair contributions to the total scattering intensity can be easily calculated from the model structures and are shown for the 4-fold, 3-fold, and 0-fold distributions in Figs. 1.8, 1.9, and 1.10, respectively.

It is immediately clear that the peaks in $I_{\perp}(q)$ cannot, in general, be simply related to particular correlations of one species to another or to itself in the K-NH₃ liquid. For instance, it can be seen from Fig. 1.8 that all three pair functions contribute significantly (and in one case, with negative amplitude) to the resultant peak at $q = 2.0 \text{ \AA}^{-1}$. Indeed the amplitude, shape, and position of that peak are seriously affected by even small changes in the relative contributions of the three constituents from which it is constructed. However, the peak at $q = 0.88 \text{ \AA}^{-1}$ is dominated by the contribution from $i_{\perp \text{K}^+-\text{K}^+}$ and as a result this peak is the most sensitive to cluster structure as can be seen from Figs. 1.5, 1.6, and 1.7. Notice, for instance, the marked regularity of the spacings between K⁺ discs in the 4-fold distribution as depicted in Fig. 1.5b which shows only those discs. The array of Fig. 1.5b is quasi-crystalline and, as a result, yields a very strong peak in $i_{\perp \text{K}^+-\text{K}^+}$ at $q = 0.88 \text{ \AA}^{-1}$. The K⁺-K⁺ pair separations are so regular in the 4-fold distribution that even the 3rd order reflection of the 0.88 \AA^{-1} peak can be seen in $i_{\perp \text{K}^+-\text{K}^+}(q)$ (Fig. 1.8a). The $q = 0.88 \text{ \AA}^{-1}$ peak has largely disappeared from $I_{\perp}(q)$ for the 3-fold coordinated structure because the K⁺-K⁺ distances are much more irregular as can be seen from

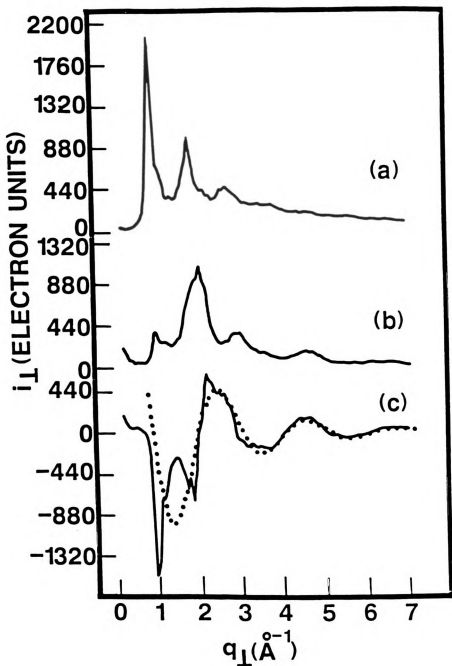


Fig. 1.8. The calculated (solid line) (a) K^+-K^+ , (b) NH_3-NH_3 , and (c) K^+-NH_3 pair contributions $[i_{\perp}(q)]_{K^+-K^+}$, $[i_{\perp}(q)]_{NH_3-NH_3}$, and $[i_{\perp}(q)]_{K^+-NH_3}$ to the in-plane diffuse scattering from the fourfold coordinated distribution shown in Fig. 1.5(a). The dots are a plot of $2f_K(q)r_{NH_3}(q)J_0(qR)$ with $R=2.89$ Å (see text).

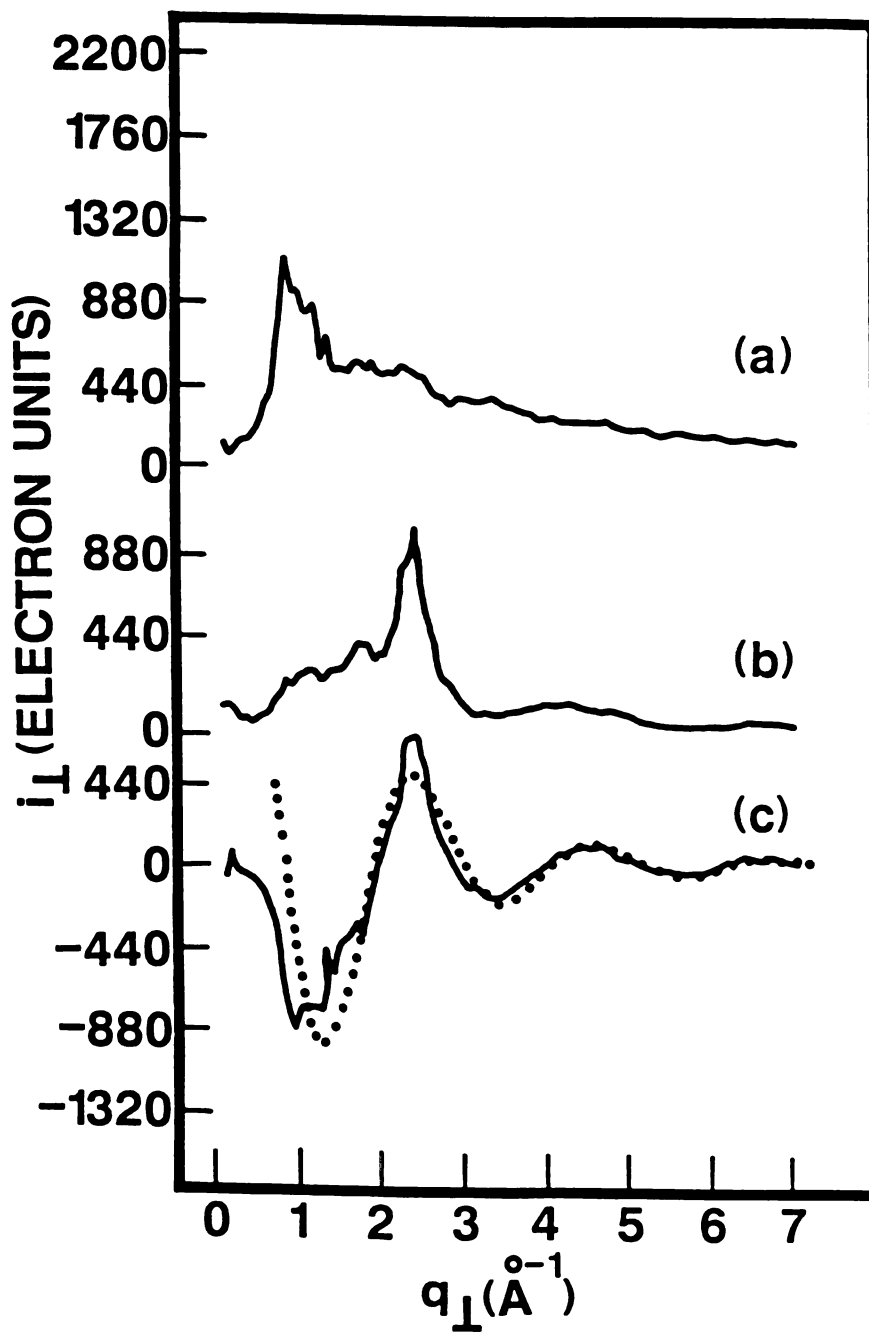


Fig. 1.9. Pair contributions to the in-plane diffuse scattering calculated using the threefold coordinated distribution shown in Fig. 1.6(a). See the caption of Fig. 1.8 for an explanation of the symbols and labels used here.

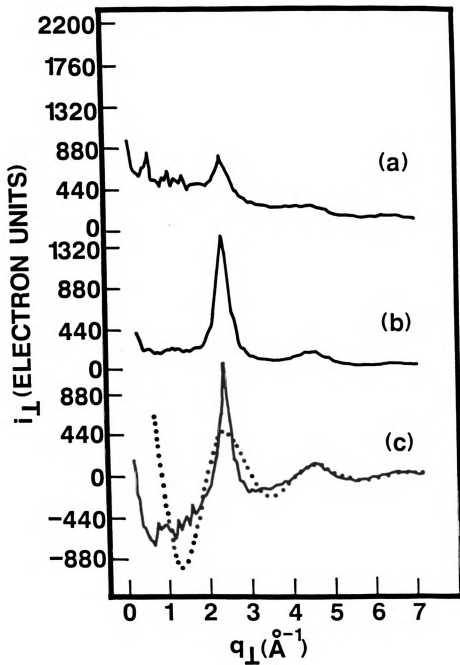


Fig. 1.10. Pair contributions to the in-plane diffuse scattering calculated using the zero-fold coordinated distribution shown in Fig. 1.7(a). See the caption of Fig. 1.8 for an explanation of the symbols and labels used here.

Fig. 1.6b. This peak is completely absent in the 0-fold coordination pattern (Figs. 1.7a and 1.10) because there is no dominant pair separation in the K^+-K^+ configuration [Fig. 1.7b] for that structure.

The regularity of the K^+-K^+ pair separations in the 4-fold coordinated structure provides us with the opportunity to deduce an analytical expression for the position of the K^+-K^+ contribution to the sharp first peak in $I_{\perp}(q)$. As noted above, this peak is dominated by the local ordering of K^+ positions, which form a quasicrystalline array over a region of size approximately 50 clusters. The separation between K^+ ions in this array is the distance od in Fig. 1.4. With the aid of that figure this distance, $r_{O_{K^+-K^+}}$, can be calculated, with the result

$$r_{O_{K^+-K^+}} = \left[\frac{1}{2} R^2 + \left\{ \sqrt{2}R + \left[(2\langle r_{NH_3} \rangle)^2 - \frac{1}{2} R^2 \right]^{1/2} \right\}^2 \right]^{1/2} \quad (20)$$

with

$$R = r_K + \langle r_{NH_3} \rangle \quad (21)$$

where r_K and $\langle r_{NH_3} \rangle$ have been defined above. For momentum transfer \vec{q} along a line parallel to the line od in Fig. 1.4, there is constructive interference of the waves scattered from these K^+ ions if

$$|\vec{q}| = q_0 = \frac{2\pi}{r_{O_{K^+-K^+}}} \quad (22)$$

In a large sample of liquid there are locally ordered regions with arbitrary alignment. Therefore, this constructive interference occurs for any direction of \vec{q} . The values of r_K and $\langle r_{NH_3} \rangle$ in the computer-generated sample of closely packed 4-fold $K-NH_3$ clusters are $r_K = 1.46$

\bar{A} and $\langle r_{\text{NH}_3} \rangle = 1.43 \text{ \AA}$, respectively; the corresponding value of q_0 from Eq. (19) is $q_0 = 0.98 \text{ \AA}^{-1}$. This is the position at which the sharp first peak in $i_{\perp \text{K}^+ - \text{K}^+}(q)$ occurs, as can be seen from Fig. 1.8, and it is this peak which is primarily responsible for the first peak in $I_{\perp}(\vec{q})$ for the 4-fold distribution. Note, however, that the contributions from $i_{\perp \text{K}^+ - \text{NH}_3}(\vec{q})$ and to a lesser extent $i_{\perp \text{NH}_3 - \text{NH}_3}(q)$ are sufficient to cause a slight downward shift of the first peak in $I_{\perp}(\vec{q})$ to 0.88 \AA^{-1} , the exact position at which it is observed experimentally. The next peak in $i_{\perp \text{K}^+ - \text{K}^+}(q)$, which occurs at $\approx (1.9) \text{ \AA}^{-1}$, is the second harmonic of the interference. It is broader than the lowest peak because the structure is not crystalline.

A striking feature of the pair contributions to $I_{\perp}(q)$ is the similarity in the $\text{K}^+ - \text{NH}_3$ contributions shown in Figs. 1.8c, 1.9c, and 1.10c particularly with regard to the peak at $\approx 2.5 \text{ \AA}^{-1}$. This similarity results from the fact that the mean radius of the ammonia discs is the same for each distribution and the NH_3 discs have a relatively small spread in their radii. Therefore, there is a dominant $\text{K}^+ - \text{NH}_3$ distance that manifests itself in each of the distributions we have addressed. To illustrate this point further, we show in Fig. 1.8c the Bessel function contribution $J_0(qR_0)$ to $i_{\perp \text{K}^+ - \text{NH}_3}$ from a single pair separation R_0 (see Eq. 21), where $R_0 = 2.89 \text{ \AA}$. Clearly, this function gives a very good fit to $i_{\perp \text{K}^+ - \text{NH}_3}(q)$ in the range $q > 2 \text{ \AA}^{-1}$ and shows only interference induced deviations from $i_{\perp \text{K}^+ - \text{NH}_3}(q)$ in the region $q < 2 \text{ \AA}^{-1}$. This

result confirms the dominance of the distance R_0 in the 4-fold coordinated distribution. Analogous results for $J_0(qR_0)$ are obtained from the 3-fold and 0-fold distributions as can be seen from Figs. 1.9c and 1.10c.

We have also studied the case in which all NH_3 discs have the same fixed radius. In this case the distribution function $P(r)$ is given by

$$P(r) = \delta(r - \langle r_{\text{NH}_3} \rangle) \quad (23)$$

as is shown in the inset of Fig. 1.11, the full panel of which shows the corresponding calculated $I_{\perp}(q)$. The form of $I_{\perp}(q)$ at small q is similar to that for the 4-fold coordinated structure with a spread in tilt angles (i.e. Fig. 1.5c). However, the peak at $q \sim 4.5 \text{ \AA}^{-1}$ is significantly sharper for the case of a fixed NH_3 radius than for a variable NH_3 radius. As can be seen from Fig. 1.12, this high- q feature is a higher harmonic of features that appear at low q . The 4-fold coordinated structure with fixed NH_3 radius produces a more regular arrangement than the structures described earlier. For example, the K^+ contribution to $I_{\perp}(q)$ (Fig. 1.12a) shows at least five orders of the 0.88 \AA^{-1} reflection because the distances between nearest neighbor K^+ 's are almost equal if the NH_3 radius is fixed. The experimental in-plane x-ray scattering data [Fig. 1.2] does not have a sharp feature at high- q . This is clear evidence that the NH_3 radius is variable, disrupting the order of the closely-packed clusters. The structure shown in Fig. 5a, with an NH_3 radius that varies by approximately $\pm 10\%$, has a broadened peak at $q \sim 4.5 \text{ \AA}^{-1}$; however, even that is qualitatively different from the smooth behavior of the experimental data at high q .

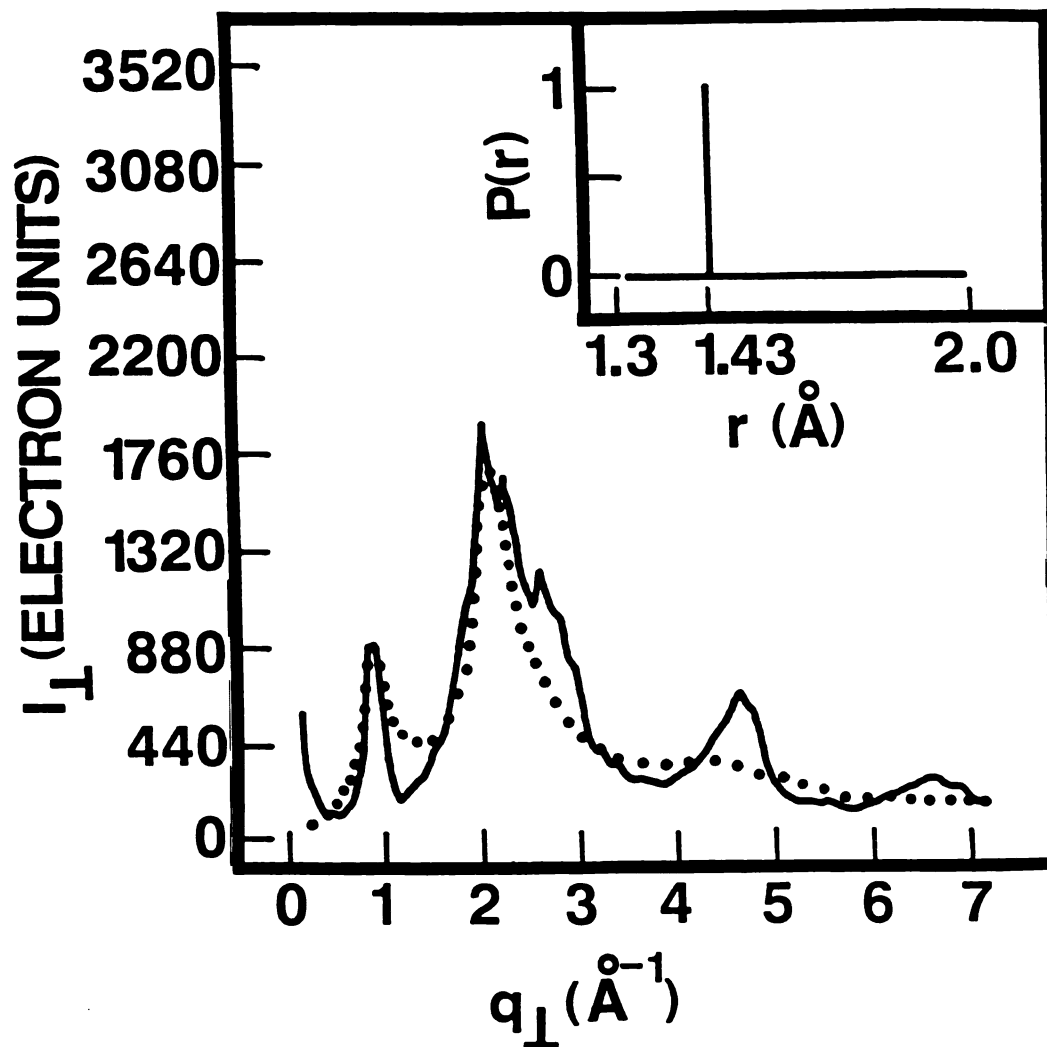


Fig. 1.11. The in-plane diffuse scattering (solid line) calculated using a fourfold coordinated distribution in which both the K^+ radius and the NH_3 radius were fixed at 1.46 and 1.43 \AA , respectively. The latter is reflected in the δ function $P(r)$ shown in the inset. The dots represent the corresponding experimental results given in Fig. 1.2.

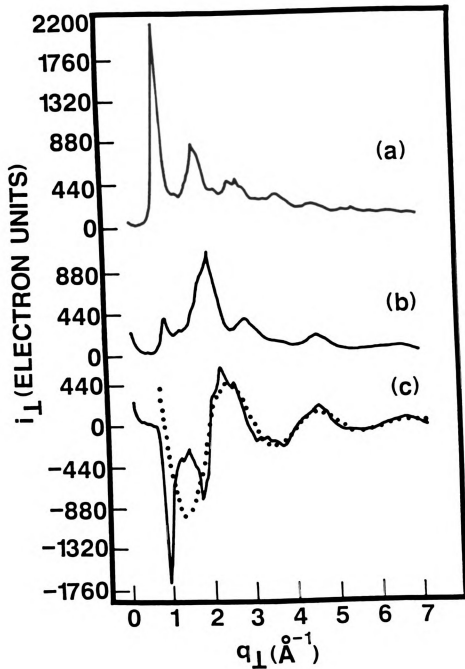


Fig. 1.12. The pair contributions to the in-plane diffuse scattering calculated using the fourfold coordinated distribution whose parameters are given in the caption of Fig. 1.11. See also the caption of FIG. 1.8.

This suggests that the physical variation of the NH_3 radius may be even greater than what we used in our two-dimensional model calculation.

V. Radial Distribution Function

One can obtain a measure of the degree of correlation in the K-NH_3 liquid by computing the mean particle-particle radial distribution function $R_{pp}(r)$ which is proportional to the probability of finding any pair of particles (i.e. K^+ or NH_3) with a pair separation of r . The quantity $R_{pp}(r)$ is defined by

$$\int_{r_1}^r R_{pp}(r) dr = \frac{1}{N} \sum_{i=1}^N \sum_{j=1}^N \theta(r_2 - r_{ij}) \theta(r_{ij} - r_1), \quad (24)$$

where

$$r_{ij} = |\vec{r}_i - \vec{r}_j|; \quad (25)$$

the indices i and j both label all the K^+ ions and NH_3 molecules, and N is the total number of particles in the system.

Figures 1.13a, b, and c, respectively, show the distribution functions $[R_{pp}(r)]_{4\text{-fold}}$, $[R_{pp}(r)]_{3\text{-fold}}$, $[R_{pp}(r)]_{0\text{-fold}}$ for the large computer-generated sample of closely packed 4-fold, 3-fold, and 0-fold coordinated clusters. The existence of sharp spikes at particular values of r indicates the existence of local ordering. The specific values of r where the peaks occur in Fig. 1.13a are associated with characteristic distances of a closely packed pair of 4-fold clusters. Refer again to Figure 1.4. There the letters label the center points of the various disks. The distances $0a$, $0b$, $0c$, $0d$, and so on, are the values of r where $[R_{pp}(r)]_{4\text{-fold}}$ has sharp peaks in Figure 13a. These

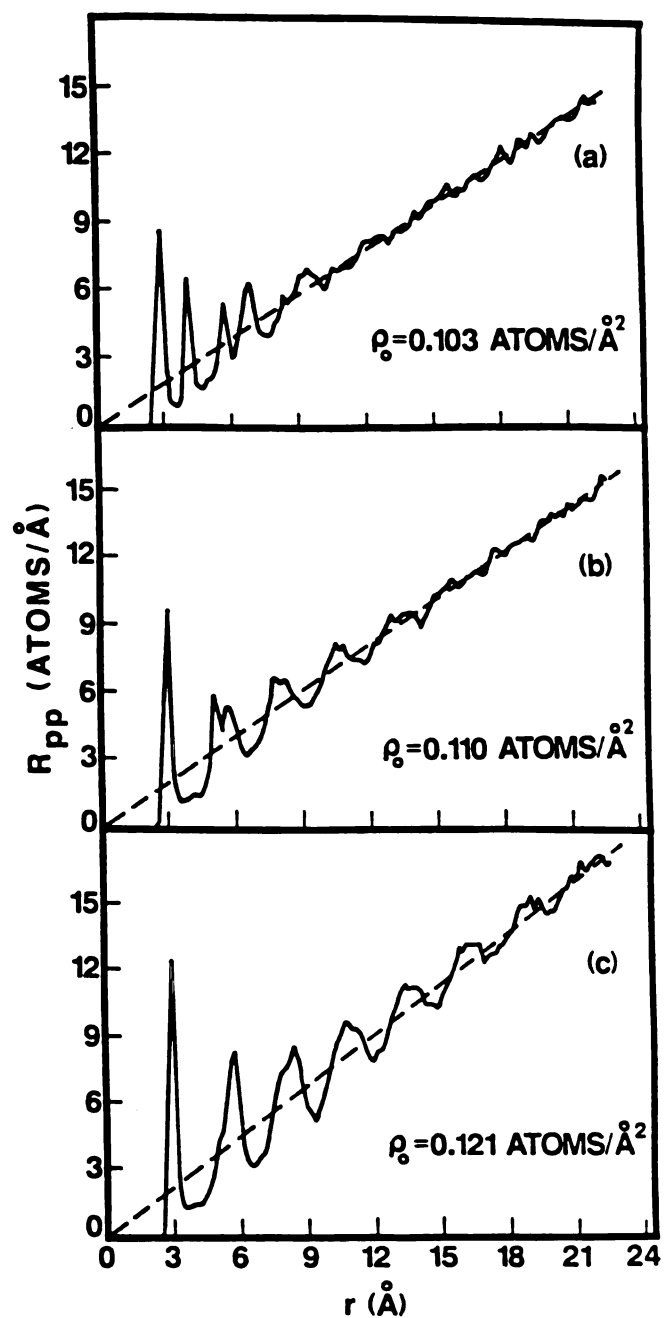


Fig. 1.13. The full particle-particle radial distribution function for the (a) fourfold, (b) threefold, and (c) zero-fold coordinated distributions shown in Fig. 1.5(a), 1.6(a), and 1.7(a), respectively. The dashed lines are plots of $r\rho_0$ where ρ_0 is the mean number density calculated in the manner described in the text.

distances are not precisely equal for all pairs of clusters, because the clusters form a liquid structure, and because in our model we let the radius of the NH_3 disks be somewhat variable. But the close packing of these 4-fold clusters produces sufficient local ordering that the variation in the distances $0a$, $0b$, etc. is small. Thus, $R(r)$ has sharp peaks. The distribution $[R_{pp}(r)]_{0\text{-fold}}$ is quite different than $[R_{pp}(r)]_{4\text{-fold}}$ because the uncorrelated discs just form a close-packed array of particles having approximately equal radii; the peaks in $[R_{pp}(r)]_{0\text{-fold}}$ are just multiples of the near-neighbor hard disc distance. The distribution $[R_{pp}(r)]_{3\text{-fold}}$ is intermediate between the other two cases.

In the liquid state the correlation between particle positions decreases as r increases. Therefore, the peaks in $R_{pp}(r)$ broaden and then disappear as r increases. For $r \geq 20A$ the distribution functions shown in Fig. 1.13 approach

$$R_{pp}(r) \sim 2\pi r \rho_0, \quad (26)$$

where ρ_0 is the mean particle number density. From Fig. 1.13 we can calculate the mean number densities $(\rho_0)_{4\text{-fold}}$, $(\rho_0)_{3\text{-fold}}$, and $(\rho_0)_{0\text{-fold}}$, and we find the values 0.103 \AA^{-2} , 0.110 \AA^{-2} , and 0.121 \AA^{-2} , respectively.

Finally, the K^+-K^+ correlations can be studied by considering the K^+-K^+ pair distribution $R_{K^+-K^+}(r)$ given by

$$\int_{r_1}^{r_2} R_{K^+-K^+}(r) dr = \frac{1}{N_{K^+}} \sum_{\substack{i=1 \\ i \neq j}}^{N_{K^+}} \sum_{j=1}^{N_{K^+}} \theta(r_2 - r_{ij}) \theta(r_{ij} - r_1) \quad (27)$$

where the sum on the right and side of Eq. (24) is now computed using only the $N_{K^+} K^+$ particles in the distribution. It is $R_{K^+-K^+}(r)$ which illustrates so clearly the distinctions between the three distributions we have discussed as can be seen from Figs. 1.14a, b, and c. Only Fig. 1.14a shows well-defined "regularly" spaced peaks characteristic of the high degree of K^+ ordering in the 4-fold coordinated distribution, whereas the 3-fold and 0-fold distributions show little (Fig. 1.14b) and no (Fig. 1.14c) K^+-K^+ correlations respectively.

Recall that the origin of the peak in $I_{\perp}(q)$ at $q \sim 0.88 \text{ \AA}^{-1}$ is the approximate local order of the K^+ ions. The K^+-K^+ radial distribution function in Fig. 1.14a indicates that the nature of the ordering is approximately rhombohedra,. This can also be seen qualitatively by inspection of the K^+ positions in Fig. 1.5a, but it can be made quantitative by inspection of the K^+-K^+ radial distribution function. A square lattice is a rhombohedral lattice with a rhombohedral angle of 90° ; the corresponding radial distribution function has peaks at $r = a$, $\sqrt{2}a$, and $2a$ (where a is the lattice spacing), each with total area 4. A triangular lattice is a rhombohedral lattice with a rhombohedral angle of 60° ; the corresponding radial distribution function has peaks at $r = a$ and $\sqrt{3}a$, each with area 6. An intermediate rhombohedral lattice with a rhombohedral angle α , where $90^\circ > \alpha > 60^\circ$, has peaks at a , $2a \cos \alpha/2$, $2a \sin \alpha/2$, and $2a$, with areas 4, 2, 2, and 4, respectively. The K^+-K^+ radial distribution function shown in Figure 14a has broad peaks with maxima at 6.8 \AA and 14.4 \AA and areas approximately 4.5 and 6, and a plateau in the region $8 \text{ \AA} < r < 13 \text{ \AA}$ with area 3.5. This indicates that the K ions are approximately ordered in an intermediate rhombohedral lattice, at least over distances of about 20 \AA .

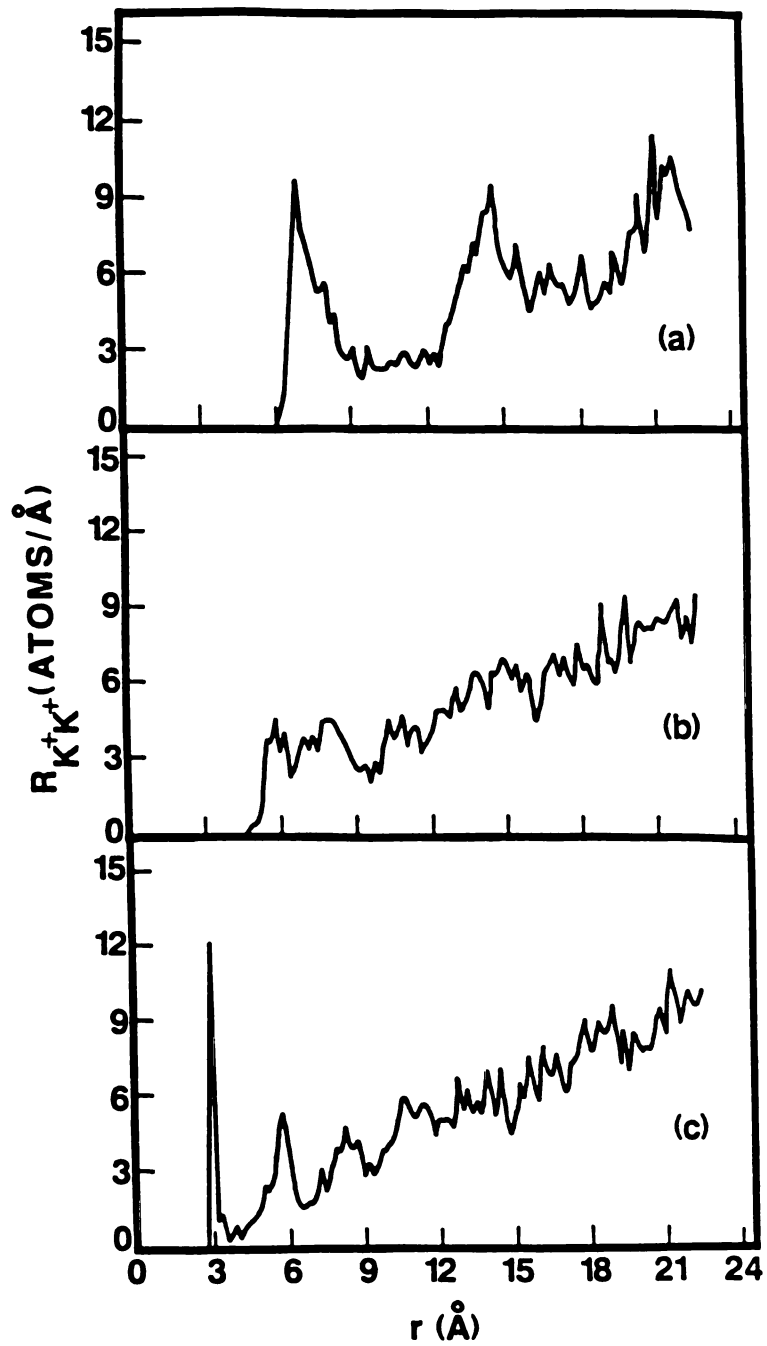


Fig. 1.14. The partial K^+-K^+ radial distribution function for the (a) fourfold (b) threefold, and (c) zerofold coordinated distributions shown in Figs. 1.5(a), 1.6(a), and 1.7(a), respectively.

VI. Concluding Remarks

Although the best fit to the experimental diffraction data was obtained with a 4-fold coordinated distribution, that fit (see Fig. 1.5c) must still be characterized as semiquantitative. The major departure from experiment exhibited by our model structure is in the high q shoulder to the 2.0 \AA^{-1} peak and the larger amplitude of the 4.8 \AA^{-1} peak, both of which are absent in the data. These discrepancies could no doubt be reduced, if not completely eliminated, if we were to introduce additional parameters or equivalently more flexibility into our model.

The high q shoulder on the 2.0 \AA^{-1} peak derives mainly from K-NH_3 and $\text{NH}_3\text{-NH}_3$ contributions both of which could be noticeably perturbed if we had allowed the angular positions of the NH_3 discs about the K^+ ions in a cluster to vary--perhaps according to a distribution function $P(\theta)$. Even more fitting parameters could have been added by taking account of the dynamic nature of the K-NH_3 liquid and the resultant fact that it will simultaneously contain clusters with differing coordination numbers. Though the introduction of additional parameters would sharply improve the agreement between the experimental and calculated diffraction patterns, we feel that such a procedure is not justified by the data and that it would mask the essential structural features--the dominance of the 4-fold coordinated clusters and the distribution in NH_3 C_3 axis tilt angles.

It is not surprising that the model which we have used does not yield a quantitative fit to the data. Rather, it is very surprising that such a simple model produces such a good semiquantitative fit.

The reader may wonder why we did not introduce and test clusters with higher coordination than 4. Such clusters are essentially precluded by the size of the ammonia discs. While 5 and even 6 such discs, each of radius $r_{\min} = 1.3 \text{ \AA}$, could just fit symmetrically around a potassium ion without overlapping, such a configurations are extremely rare in our computer-generated structures. Moreover, it is not possible to make a N-fold coordinated distribution with $N > 4$ and have all K^+ ions exactly N-fold coordinated since for our specimen $K(NH_3)_{4.38}C_{24}$, the maximum number of available ammonia molecules, 4.33 per K^+ ion, is less than 5. Thus, configurations with higher than 4-fold coordination can be ruled out.

The upper bound on cluster coordination in the 2D liquid is analogous to the situation which obtains in bulk 3D metal-ammonia solutions.⁷ In $K-NH_3$ 3D solutions, the K^+ is octohedrally 6-fold coordinated to the NH_3 molecules, the number 6 being determined by the space available around the ion to pack in NH_3 molecules. Thus, in $Li-NH_3$ 3D solutions the coordination is tetrahedral 4-fold since Li is smaller than potassium, whereas the coordination is believed to be 7-fold for the larger Cs ion in $Cs-NH_3$ 3D solutions. Also note that the 4-fold coordination of the 2D liquid $K-NH_3$ clusters is a natural consequence of the 6-fold coordination in the 3D liquid. The gallery height in $K(NH_3)_{4.33}C_{24}$ is insufficient to accommodate a $K(NH_3)_6$ octohedron.^{1,2,3} However, this height can naturally accommodate a planar $K(NH_3)_4$ cluster which is derived by removing opposite apical NH_3 molecules from a $K(NH_3)_6$ octohedral cluster.

As an additional comment, we would like to address the relationship between the in-plane areal density of the 2D $K-NH_3$ liquid, the liquid

structure, and the layer stoichiometry. Each of the computer-generated structures which we tested was assembled to satisfy the K-NH₃ stoichiometry of our samples, i.e. the ratio of the numbers of K⁺ discs and NH₃ discs was fixed at 1/4.33 independent of the cluster coordination number used. However, the in-plane density was very model-dependent because the packing fraction depended on cluster coordination. In fact, only the 4-fold distribution which yielded a density 0.10 Å⁻² which was equal, within experimental error, to the known in-plane density of our K(NH₃)_{4.33}C₂₄ sample, 0.09 ± 0.01 Å⁻². The other distributions resulted in in-plane densities of 0.11 Å⁻² (3-fold coordinated) and 0.12 Å⁻², both of which are significantly higher than the actual density.

While fitting the experimental in-plane diffraction pattern to the pattern calculated from the 4-fold coordinated distribution, we discovered that the relative intensity of the 0.88 Å⁻¹ and 2.0 Å⁻¹ peaks was dependent upon the size of the K⁺ ion and that the best results were obtained with r_{K⁺} = 1.46 Å. We can use this result to estimate the charge transfer, f, in the K(NH₃)_{4.33}C₂₄ sample if we adopt the linear relationship which has been employed by Enoki, et al.²⁷ to relate charge transfer to ion size,

$$f r_{K^{+1}} + (1 - f) r_{K^0} = r_{K^+}. \quad (25)$$

In Eq. (25) r_{K⁺¹} = 1.33 Å is the ionic radius of singly ionized potassium, r_{K⁰} = 2.38 Å²⁸ is the atomic radius of potassium and r_{K⁺} is the radius of the partially-ionized species. Using the value r_{K⁺} = 1.46 Å

in Eq. (25) we find a charge exchange $f = 0.88$. This value is gratifyingly close to the value of charge exchange determined by x-ray³ and other measurements.¹³

VII. Acknowledgments

This work is done in collaboration with D.R. Stump, S.A. Solin. We gratefully acknowledge useful discussions with B.R. York, Y.B. Fan, and S.D. Mahanti. This work was supported by the NSF under grant #DMR82-11554.

REFERENCES

1. W. Rudorff and E. Schultze, *Angew. Chem.* 66, 305 (1954).
2. S.K. Hark, B.R. York, S.D. Mahanti, and S.A. Solin, *Solid State Comm.* 50, 545 (1984).
3. B.R. York and S.A. Solin, *Phys. Rev.* B31, 8206 (1985).
4. H.A. Resing, B.R. York, S.A. Solin, and R.M. Fronko, *Proc. of the 17th Carbon Conf., Louisville, 1985* (in press).
5. D.M. Hoffman, A.M. Rao, G.L. Doll, P.C. Eklund, B.R. York, and S.A. Solin, *Mats. Res. Soc. Bull.*, 1984 (in press).
6. Y.B. Fan and S.A. Solin, *Proc. of the 17th Carbon Conf., Louisville, 1985* (in press).
7. J.C. Thompson, *Electrons in Liquid Ammonia* (Clarendon, Oxford, 1976).
8. E. Abrahams, P.W. Anderson, D.C. Licciardello, and T.V. Ramakrishnan, *Phys. Rev. Lett.* 43, 673 (1979).
9. X.W. Qian, D.R. Stump, B.R. York, and S.A. Solin, *Phys. Rev. Lett.* 54, 1271 (1985).
10. S.A. Solin, in *Localization and Metal-Insulator Transitions*, ed. by H. Fritzsche and D. Adler (Plenum Press, New York, 1985), p. 393.
11. P. Hansen, *Physical Metallurgy* (Cambridge University Press, Cambridge, England, 1978).
12. S.A. Solin, *Adv. in Chem. Phys.* 49, 455 (1982).
13. R.M. Fronko, H. Resing, Y.B. Fan, and S.A. Solin, to be published.
14. D. Neumann, H. Zabel, Y.B. Fan and S.A. Solin (unpublished).
15. Y.Y. Huang, S.A. Solin, and J. Heremans (unpublished).

16. A. Herold, in Proceedings of the International Conference on the Physics of Intercalation Compounds, edited by L. Pietronero and E. Tosatti (Springer, New York, 1981) p.7.
17. H. Herold, Bull. Soc. Chim. Fr., p.999(1955).
18. R. Clarke, N. Caswell, and S.A. Solin, Phys. Rev. Lett. 42, 61(1979).
19. H.P. Klug and L.E. Alexander, X-ray Diffraction Procedures for Polycrystalline and Amorphous Materials (Wiley, New York, 1974).
20. B.E. Warren, X-ray Diffraction (Addison-Wesley, Reading, Mass., 1969), pp. 264-275.
21. R. Clarke, N. Caswell, S.A. Solin, and P.M. Horn, Phys. Rev. Lett. 43, 886(1979).
22. S.A. Solin, in Structure and Excitations of Amorphous Solids (Williamsburg, Va., 1976), proceedings of an International Conference, AIP Conference Proceedings, No. 31, Williamsburg, Va. 1976), edited by G. Lucovsky and F.L. Galeener (AIP, New York, 1976), p. 205.
23. M. Plischke and W.D. Leckie, Can. J. Phys. 60, 1139 (1982).
24. L. Pauling, The Nature of the Chemical Bond (Conell, Ithaca, 1960).
25. T.C. Farrar and E.D. Becker, Pulse and Fourier Transform NMR(Academic, New York, 1971).
26. G.S. Cargill III, in Solid State Physics, edited by H. Ehrenreich, F. Seitz, and D. Turnbull (Academic, New York, 1957), Vol. 30, p. 227.
27. T. Enoki, M. Sano, and H. Inokuchi, J. Chem. Phys. 78, 2017 (1983).
28. N. Glinka, General Chemistry (Gordon and Breach, New York, 1965), p. 146.

PART II

The Microstructure-Derived Macroscopic Residual Resistance
of Brominated Graphite Fibers

1.

2.

3.

4.

5.

6.

7.

8.

9.

10.

11.

12.

13.

14.

15.

16.

17.

18.

19.

20.

21.

22.

23.

24.

25.

26.

I. INTRODUCTION

During the past few decades, pitch-based graphite fibers prepared at high temperature by the graphitization of precursor material such as mesophase pitch have attracted considerable interest and attention primarily as a result of potential practical applications which are based on their novel physical properties ¹. For instance, it is now well known that pitch-based graphite fibers are not only light weight and very strong mechanically as evidenced by a high tensile strength and high Young's modulus ² but they also exhibit modest electrical conductivity ³.

The relatively recent discovery that the electrical properties of pitch-based graphite fibers (herein after referred to as PB fibers) can be greatly modified by the intercalation of guest species without concomitant degradation of their desirable mechanical properties has further heightened the already established keen interest alluded to above ³⁻⁵. While many chemically distinct types of intercalated PB fibers have been synthesized in an empirical effort to improve their electrical properties, the fundamental relationship between the microscopic distribution of guest species in the fiber and its macroscopic resistance has, to our knowledge, not been addressed. Yet, for a given species of guest its microscopic distribution in the fiber critically determines the ultimate conductivity. Accordingly, we report in this paper a detailed scanning transmission electron microscope (STEM) study of the distribution of one selected (see below) chemical species, Br, inserted into PB fibers. Our experimental results together with a wealth of information on the companion material, Br intercalated highly oriented pyrolytic graphite (HOPG) ^{6,7} and other graphite

intercalation compounds (GIC's) ⁸, have provided the input for a theoretical model which we have developed to deduce the macroscopic fiber resistance from a knowledge of the guest species and it's microscopic distribution.

To date the evidence that Br is actually intercalated into the PB fiber rather than absorbed on internal surfaces is weak since no convincing X-ray data in support of intercalation have been presented. Whatever the insertion mechanism, the unusual air stability and electrical properties of PB fibers clearly warrant investigation by the method employed here. However we are reluctant to characterize the modified fibers as intercalation compounds and hereinafter employ the descriptive phrase "brominated" to signify the physical alteration associated with exposure to Br.

Bromine intercalated PB fiber is one of the few fiber GIC's which has a stable residue phase in air and in vacuum ^{5,9,10}. (Here a residue compound is one in which desorption of the intercalant species by reaction with the environment, pumping off etc. is incomplete. The residual intercalant may be pinned to defects in the host graphitic material.) Thus Br-PB fiber is an ideal material for a STEM study of the type reported here. When exposed to and maintained in a Br vapor of sufficient vapor pressure, PB fibers form a saturated compound with a typical resistivity of $\sim 15 \mu\Omega\text{-cm}$. This represents an 18- fold decrease over the resistivity of the pristine fiber of $253 \mu\Omega\text{-cm}$. When the saturated fibers are removed from the Br vapor and subsequently exposed to ambient environment to form a Br deficient residue compound, their resistivity rises by a factor of three to $\sim 45 \mu\Omega\text{-cm}$ ¹¹.

In order to understand the resistivity changes between the saturated and residual PB fiber we adopted the following approach: First the microscopic Br distribution in the residual fiber is determined using the STEM . Then a model which relates the local conductivity of the fiber to the local density of Br is developed and used to calculate the resistivities of the residual and saturated fibers. The calculated results are then compared to experimental results to test the validity of the model.

II. EXPERIMENTAL TECHNIQUES AND JUSTIFICATION

A. Samples and Preparation

The pristine PB fibers which were used in this study had a typical cross-sectional dimension of about 10 μm , a density of (1.99 ± 0.05) gm/cm^3 and were obtained from Union Carbide Corporation . Morphologically, they are composed of highly graphitized carbon ribbons which are bundled together in such a way that on average the carbon layers align radially outward from the center longitudinal axis of the fiber ^{1,11}.

To achieve bromination PB fibers were exposed to Br vapor at a pressure in excess of the threshold pressure for reaction ^{9,10}. The compounds formed after equilibrium is obtained are referred to as "saturated", and have a density of (2.39 ± 0.05) gm/cm^3 corresponding to a composition of $\text{C}_{22.5}\text{Br}^{12}$. These saturated PB fibers were subsequently removed from the Br vapor and exposed to air at ambient temperature ⁹. The resulting debrominated "residual" fibers which have a density of (2.19 ± 0.05) gm/cm^3 corresponding to a composition of $\text{C}_{45}\text{Br}^{3,12}$ were found to be stable in air vis à vis their electrical

properties and were even stable in a 100% relative humidity environment^{9,10}. It is these residual Br-PB fibers which were the major focus of this study.

The longitudinal resistance of each fiber was measured in-situ during each stage of its synthesis using techniques that are described in detail elsewhere¹⁰. In Table 1. we present the results of these measurements for seven of the fiber specimens used in this study. It is interesting to note that the variation in the ratio of the resistance of the residual fiber to that of the saturated fiber is partially correlated with the ratio of the resistance of the pristine fiber to that of the saturated fiber. For instance, the fiber with the lowest ratio R_r/R_s (see Table 1) also has the lowest value of R_p/R_s . Since R_p/R_s is a measure of the degree of bromination of the fiber, and R_r/R_s characterizes the degree of debromination, this partial correlation shows that the easier the Br can be inserted, the easier it can be released. This suggests that bromination of the fiber is a physical absorption process which depends heavily on the defects of the material.

To prepare the residual fibers for STEM studies segments (typical length 0.5mm) of the single strands that were affixed to a ceramic plate at four points with the electrically conductive glue used for the electric resistance measurements were cut from the regions between glue dots with a razor blade. After cutting, the fiber pieces were floated off of the plate onto the surface of doubly distilled deionized water and picked up with folded copper electron microscope grids (mesh size 200) of standard dimension 3mm. These grids were mounted to a dual gimble beryllium nosed tiltable cartridge for microscope studies.

Table 1. Resistances and Resistance Ratios of Brominated P100 Pitch-Based Graphite Fiber

Sample #	Pristine Fiber $R_p (\Omega)$	Saturated Fiber $R_s (\Omega)$	Residual Fiber $R_r (\Omega)$	R_r/R_s	R_p/R_s
1	71.99	3.99	13.04	3.26	18.04
2	59.74	3.41	10.95	3.21	17.52
3	55.99	5.15	10.70	2.07	10.87
4	79.30	5.42	16.00	2.95	14.63
5	83.44	4.44	15.57	3.5	18.79
6	88.21	5.29	16.83	3.18	16.67
7	77.02	4.83	14.46	2.99	15.95

I
C
r
:
e
h
C
t
i
s
C
B
O
t
-
r
e
a
c
e
b
t
P
be

B. Apparatus

The measurements reported here were made with a 100-kV Vacuum Generators Model HB501 analytical scanning transmission electron microscope equipped with a field-emission tip, digital beam control, a 30-mm² Li-drifted Si energy-dispersive X-ray (EDX) detector with an energy resolution of 157 eV, an annular dark-field detector (collection half-angle θ , $0.01 \text{ rad} \leq \theta \leq 0.5 \text{ rad}$), and an energy loss spectrometer capable of 0.5 eV resolution. The vacuum level in the sample space was typically between $7 \cdot 10^{-10}$ and $3 \cdot 10^{-9}$ torr. This instrument is interfaced with a Tracor Northern Model 2000 computerized detection system which provides both signal processing and digital beam control.

C. Method and Analysis

In Fig. 2.1a the experimental configuration used to ascertain the Br distribution in brominated PB fibers is illustrated. The fiber is oriented with its axis perpendicular to a 100 kV electron beam which is tightly focussed to a diameter of approximately 50 Å. A beam current of $\sim 1 \cdot 10^{-9}$ amp was used and was found to be below the threshold for radiation damage in our specimens. As is depicted in Fig 2.1a., energetic electrons traverse the specimen and in so doing excite Br atoms in their pathway to emit inner-shell X-ray photons which are collected by an EDX detector. An example of the X-ray emission spectrum created by this process is shown in Fig. 2.1b which also shows the bromine $K\alpha_1$ line that is used as a fingerprint of the Br distribution in the fiber. Notice that for a given lateral position (e.g. horizontal position in the figure) the integrated X-ray intensity from the entire beam path traversed is collected. By digitally repositioning the beam

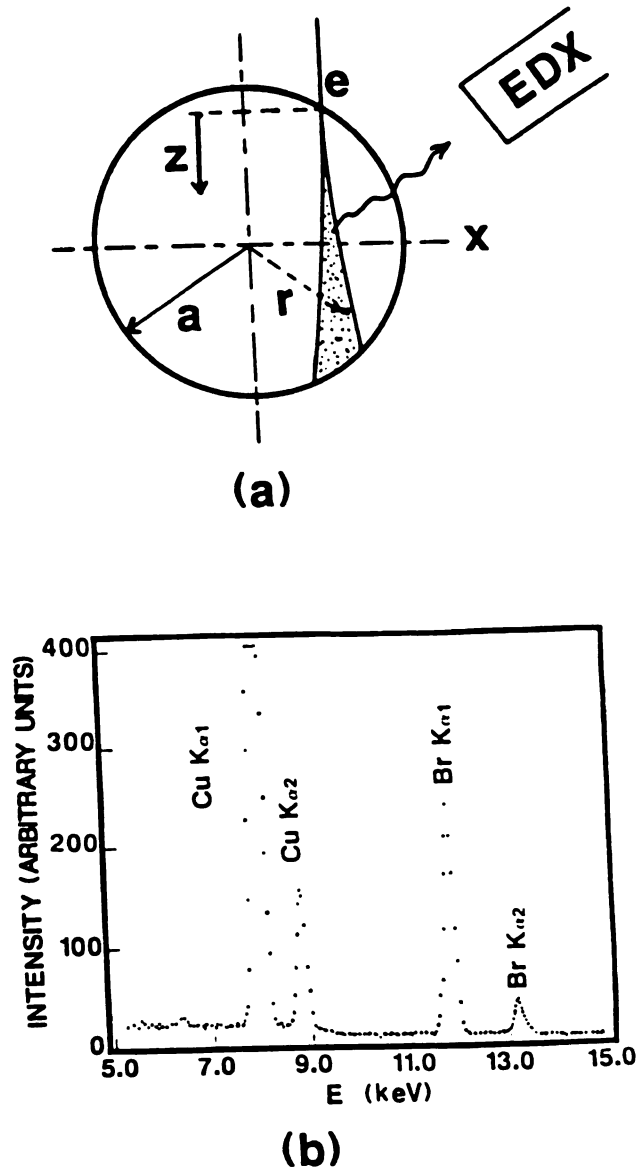


Fig. 2.1. (a) A schematic diagram of the experimental configuration. The circle represents the cross-section of a 10 μm PB fiber the dotted region of which is the volume containing 90% of the incident electrons whose lateral position of entry into the fiber is measured along the x axis. The label EDX represents the energy dispersive X-ray detector. (b) The energy dispersive X-ray spectrum of the fiber showing the Br K α lines from the specimen and spurious Cu K α lines from the supporting microscope grid.

to a new lateral location and again accumulating X-ray signal for a fixed preset time, the later spatial profile of the X-ray intensity can be determined. It is this profile which provides quantitative information on the microscopic Br distribution in the fiber.

To establish the Br distribution from the above described EDX measurement we must be able to relate the X-ray intensity to the electron beam depth profile and range in the specimen. For instance, the bromine cross-sectional distribution could not be measured by EDX if the electron beam only penetrated to a depth which was a small fraction of the fiber radius. Fortunately this is not the case.

When electrons strike a bulk material, they strongly interact with the material through both elastic and inelastic scattering processes and as a result their propagation direction deviates from the direction of the incident beam. (Of these several processes, only the inner shell excitation which generates the EDX spectrum is of immediate relevance here.) The path traversed by the interacting electrons in the material, and in particular those that are capable of generating X-ray photons, has been extensively studied using both experimental methods¹³ and theoretical Monte Carlo techniques¹⁴. It is found that though the electrons lose energy and scatter away from the incident direction during penetration they nevertheless remain confined to a bulbous region as depicted schematically in Fig. 2.2. For X-ray generation, the excitation range R (in μm) can be deduced from the following equation¹⁵

$$R = \frac{1}{\rho} t (E_0^{1.68} - E_c^{1.68}) \quad (1)$$

Here E_0 (in keV) is the energy of the incident electrons, E_c (in keV) is the critical excitation energy for the inner shell X-ray emission line, t is a constant and is equal to $6.4 \times 10^{-6} \text{ gm}/(\text{cm}^2 \text{ keV})$, ρ (in gm/cm^3) is

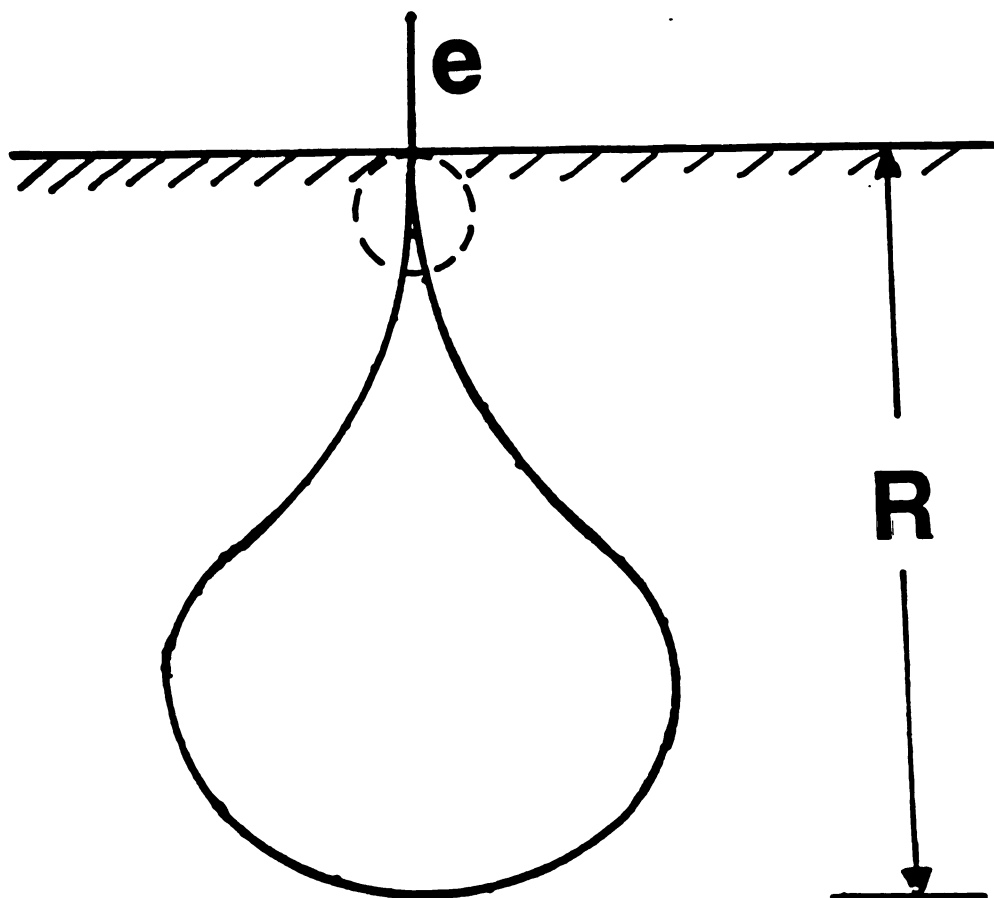


Fig. 2.2. A schematic scaled diagram of the Br K_{α} X-ray excitation region of a bulk $C_{45}Br$ material by a 100 KeV electron beam. The dashed circle represents the 10 μm diameter fiber cross-section. R is the excitation range defined in the text.

the mass density of the material and R is the mean distance that the electron travels when it loses energy to a value of E_c . Notice that R is significantly larger than λ , the mean free path of an electron where λ is defined by the mean distance the electron can travel between two subsequent collisions. In contrast, the electron can undergo many collisions with the atoms before its energy is reduced to E_c at which point it ceases to cause inner shell excitation.

The residual Br-PB fibers studied here have an average mass density of $2.19 \pm 0.05 \text{ gm/cm}^3$ corresponding to a composition $C_{45}Br$. Also in our case $E_0 = 100 \text{ keV}$ and $E_c = 11.94 \text{ keV}$ for the Br $k\alpha_1$ line. Using these values in Eq. 1. we find a value of $R = 71 \text{ }\mu\text{m}$. This value is very large compared to the $10 \text{ }\mu\text{m}$ diameter of the fiber; thus, the X-ray generating electron beam completely penetrates the sample.

To determine the Br profile quantitatively it is necessary to know the detailed path of the electrons through the fiber. We computed this path using a Monte Carlo calculation program developed by Joy¹⁶. The results of this calculation are shown in Fig 2.1a. where the dotted region depicts the volume through which 90% of the incident electrons pass. The computer-generated cross-sectional radius of the beam, b , can be expressed empirically as an analytic function of the penetration depth, z , using the following equation¹⁷:

$$b(z) = C \cdot \frac{1}{E(z)} z^{3/2} \quad (2)$$

Here $E(z)$ is the depth-dependent energy of the electron in KeV, b and z are given in μm , and C is a constant which depends on atomic number, atomic weight, and fiber density and for the Br-PB fibers studied here has a value of $6.7 \text{ keV}/(\mu\text{m})^{1/2}$. Moreover, it can be shown that for the

fibers studied here, the Monte Carlo calculation yields an electron energy variation with depth which can be empirically written as

$$E(z) = E_0 - \gamma z \quad (3)$$

for

$$0 \leq z < 10\mu\text{m}$$

where $\gamma = 0.6 \text{ keV}/\mu\text{m}$. In deriving Eqs (2) and (3) we assumed a uniform density of Br in the fiber corresponding to a composition of C_{45}Br or equivalently, an effective atomic number and atomic weight of 6.64 and 13.5, respectively. This assumption is quite reasonable because the intercalant is so sparsely distributed in the fiber (the average density of Br is 0.2 gm/cm^3) that the density variation due to Br is negligible.

Having determined the electron beam-path in the fiber, we can now calculate the X-ray intensity profile. Consider a small excitation region located at a penetration depth z with a lateral position x , an incremental cross-sectional area ds and a thickness dz (see Fig. 2.1a.). The incremental X-ray intensity generated by the interaction of the electron beam with this small volume will be

$$\delta I(x) = \text{const.} \cdot \theta(E) \eta_e \rho_{\text{Br}} (ds)(dz) \quad (4)$$

where $\theta(E)$ is the Br K-shell ionization cross section, η_e is the incident electron current density, and ρ_{Br} is the density of Br only. The functional form of $\theta(E)$ has been deduced by Powell¹⁸ who finds

$$\theta(E) = \text{const.} \cdot \frac{1}{E} \ln \left(\frac{E}{E_c} \right). \quad (5)$$

The electron current is of course maintained constant during an X-ray acquisition scan. Thus

$$\eta_e = \text{const.} \cdot \frac{(ds)}{\pi[b(z)]^2}. \quad (6)$$

Now Eqs. (4)-(6) can be combined to yield the total X-ray intensity, $I(x)$, measured with the electron beam at a lateral position, x , in the fiber

$$I(x) = \text{const.} \cdot \iiint \frac{\rho_{\text{Br}}(r(x), z) \ln\left[\frac{E(z)}{E_c}\right]}{E(z)[b(z)]^2} (ds)(dz). \quad (7)$$

The integration in Eq. (7) is carried out over the excitation volume which contains 90% of the incident electrons as discussed above.

In the derivation of Eq (7) we have justifiably neglected the self absorption of the $\text{Br K}\alpha_1$ emission as it exits the fiber. The absorption length for an X-ray line is given by $L = 1/\mu$ where μ is the mass absorption coefficient¹⁹. For the $\text{Br K}\alpha_1$ line of C_{45}Br , $L = 2000\mu\text{m}$ which is much much greater than the fiber diameter. Therefore self absorption can indeed be neglected in this case.

One can, in principle, deduce the Br distribution $\rho_{\text{Br}}(r)$ from Eq. (7) if $I(x)$ is known. However this is difficult in practice as a result of the complex integrations involved. Instead, we adopted a more tractable procedure in which a functional form of the Br distribution is first assumed and then tested by comparing the resultant calculated profile $I(x)$ with the measured X-ray profile. The application of this procedure will be discussed below.

III. THE FIBER RESISTANCE CALCULATION

In order to calculate the macroscopic resistance of the Br-PB fiber we must know the relation between the Br density and the bulk conductivity of a host material homogenously saturated with bromine. Since the Br concentration in our fibers is very low even at saturation

we make the reasonable assumption that the axial conductivity of the brominated fiber relative to that the pristine fiber is linearly proportional to bromine content. This assumption is supported by the work of Sasa⁶ who studied the electrical properties of natural graphite intercalated with Br. He found that for the low concentration range the composition-dependent relative conductivity varied as

$$\frac{\sigma}{\sigma_0} = 1 + \alpha \rho_{\text{Br}} \quad (8)$$

where σ_0 is the conductivity of the pristine material, σ is the conductivity of the GIC, ρ_{Br} is the Br density as before, and α is a coefficient of linearity. Equation (8) is valid in the range $0 \leq \rho_{\text{Br}} \leq 0.56 \text{ g/cm}^3$ for which the value of α appropriate to our case is $\alpha = 0.023 (\text{Br/C})^{-1}$.

If we assume that the Br density is cylindrically symmetric, i.e. $\rho_{\text{Br}} = \rho_{\text{Br}}(r)$, then the total conductance of a fiber with radius a and length l is

$$G = \frac{\sigma_0}{l} \int_0^a [1 + \alpha \rho_{\text{Br}}(r)] 2\pi r dr \quad (9)$$

and the corresponding macroscopic resistance is

$$R = \frac{l}{\pi a^2 \sigma_0} \left[1 + \frac{2\alpha}{a} \int_0^a \rho_{\text{Br}}(r) r dr \right]^{-1} \quad (10)$$

To illustrate the application of this result, suppose that the Br distribution is Gaussian-like. Then

$$\rho_{\text{Br}}(r) = \rho_0 e^{-r^2/(\beta a^2)} \quad (11)$$

where ρ_0 is a constant and β is a Gaussian width parameter. On inserting Eq. (11) into Eq. (10) and carrying out the integration, one finds a total fiber resistance given by

$$R = \frac{l}{\pi a^2 \sigma_0} \left[1 + \alpha \rho_0 \beta (1 - e^{-1/\beta}) \right]^{-1} \quad (12)$$

IV. EXPERIMENTAL RESULTS AND DISCUSSION

A. Intensity Profiles

X-ray cross-sectional line profile measurements were carried out on several different segments along the length of a fiber section using the STEM. It was found that on most areas examined, the X-ray line profile had a very round or bell-shape form as shown in Fig. 2.3a. Such regions always exhibited a relatively high Br content and will therefore be referred to as Br-rich. A few of the segments examined along the fiber length yielded X-ray profiles which were Gaussian-like as depicted in Fig. 2.4a. Moreover, in these Gaussian-like regions the X-ray signals are relatively weak indicating a deficiency of Br. Accordingly, the Gaussian-like regions will be referred to as Br-poor. Note that the Br-poor regions are very significant because the longitudinal resistance of the fiber is primarily determined by these regions.

One additional feature of the Br-poor regions warrants attention. These regions exhibit a marked depletion layer extending radially inward from the fiber surface to a depth of approximately $1\mu\text{m}$. An expanded scale X-ray line scan of one such depletion layer region is shown in Fig. 2.5. and reveals a complete absence of Br in the depleted area. It is probable that the depletion layer results from the fiber morphology itself. That morphology produces a surface structure with a local porosity which varies along the fiber length. The most porous areas cannot effectively confine residual Br or shield it from reaction with the ambient environment.

Using Eq. (7) derived in the previous section and the assumption of a Gaussian-like or uniform Br cross-sectional distribution we have carried out computer calculations of the X-ray intensity profile for Br $K\alpha_1$

(a)

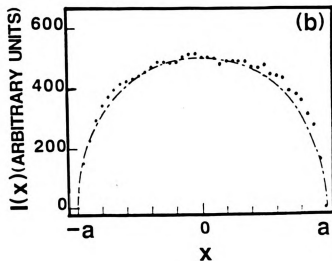
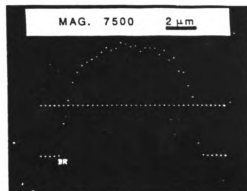


Fig. 2.3. (a) The Br $K_{\alpha 1}$ X-ray intensity profile of a Br-poor region of a PB fiber superposed on the bright field image of the fiber. The straight and curved dotted lines have the same meaning as in Fig. 2.3(a) above. (b) A plot of the Br $K_{\alpha 1}$ X-ray intensity vs. beam position (solid dots as in Fig. 2.3(a)). The dashed line is the calculated result from a uniform Br distribution and the solid line is the calculated intensity from the gaussian distribution given in panel (c). (c) A plot of the Br density vs. radial coordinate in the fiber. The dashed line is a uniform distribution, and solid line is a Gaussian form with $\beta = 0.45$.

Fig. 2.4. (a) The Br $K_{\alpha 1}$ X-ray intensity profile (curved line of dots) of a Br-rich region superposed on the bright field image of a PB fiber the longitudinal axis of which lies in a plane that is perpendicular to the incident electron beam. The straight dotted line denotes the lateral position of the electron beam as it is digitally scanned across the fiber cross-section. The magnification scale is indicated in the upper right portion of the figure. (b) A plot of the Br $K_{\alpha 1}$ X-ray intensity vs. the lateral position of the incident beam as indicated by the straight line of dots in (a) above. The solid dots represent the experimental data points from (a) and the dashed line is the calculated intensity from a uniform Br distribution,

(a)

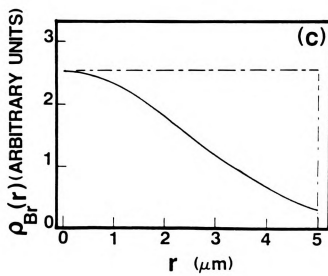
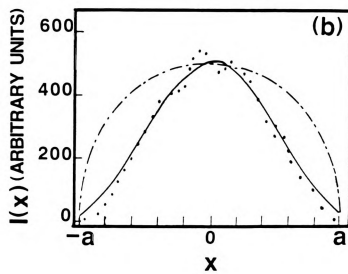


Fig. 2.4.

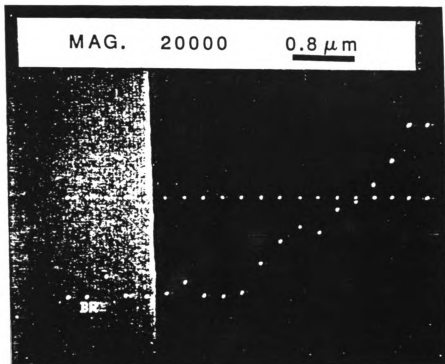


Fig. 2.5. The Br K_{α} X-ray intensity profile of a region near the edge of a PB fiber superposed on the bright field image of the fiber. See also the caption of Fig. 2.3(a).

radiation and compared our results with the above described experimental measurements. These comparisons are shown in Figs. 2.3b and 2.4b. As can be seen, the agreement between theory and experiment in Fig. 2.3b is excellent and provides direct confirmation of the uniformity of the Br distribution in the Br-rich regions. Most revealing about Fig. 2.3b is the fact that the rounded shape of the X-ray profile, if not properly analyzed, could easily be misconstrued to represent a Br density which decreases with increasing radial distance from the fiber axis. In fact the real cause of the observed profile is the reduced thickness of the fiber sampled by the electron beam as its lateral distance from the fiber axis is increased.

In Fig. 2.4b the measured X-ray intensity profile of a Br- poor region is compared with calculations in which both a uniform distribution and a Gaussian distribution were used in Eq. (7). Clearly the Gaussian distribution yields a much better fit although marked discrepancies between theory and experiment can be noted at the edges of the profile which correspond to the surface of the fiber. In that area, the theoretical results give a significant excess intensity relative to experiment. This discrepancy is a direct manifestation of the Br depletion layer.

As previously noted, we also measured the Br distribution along the length of a fiber section. The results of this measurement, in which the electron beam was laterally aligned to pass through the fiber axis, are shown in Fig. 2.6 which clearly reveals a distinct inhomogeneity characterized by extended Br-rich regions interspersed with short Br-poor regions.

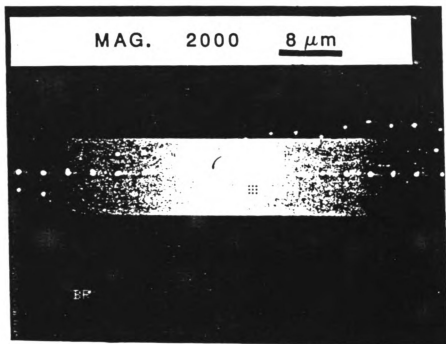


Fig. 2.6. The Br K_α X-ray intensity variation along a PB fiber superposed on the bright field image of the fiber the axis of which is perpendicular to the incident electron beam and horizontal in the figure. See also the caption of Fig. 2.3(a).

B. Fiber Resistance

We now address the change in resistance which occurs when saturated Br-Pb fibers transform to residual fibers upon prolonged exposure to air. Assume that in the saturated fiber, Br is uniformly distributed across the fiber with a density ρ_s while the Br distribution in the residual fiber is taken as Gaussian radially but uniform longitudinally. This latter assumption is supported by the fact that the overall resistance of the fiber is largely determined by the Br-poor regions in which the conductivity is low, and in these regions the Br distribution is Gaussian. With the just noted assumptions and Eqs. (9)-(12) we find the ratio of the residual fiber resistance, R_r , to the saturated fiber resistance, R_s , to be

$$\frac{R_r}{R_s} = \frac{1 + \alpha \rho_s}{1 + \alpha \rho_r \beta (1 - e^{-1/\beta})} . \quad (13)$$

In deriving Eq. (13) the very small change in fiber radius engendered by the transition from saturated to residue form has been neglected.

From the measured densities of the parent saturated fibers and the daughter residue fibers used in this study we find the corresponding Br densities to be $\rho_s = 0.40 \pm 0.05 \text{ g/cm}^3$ and $\rho_r = 0.20 \pm 0.05 \text{ g/cm}^3$, respectively. Using these values together with a value of $\beta = 0.45$ deduced from Fig. 2.4. we find from Eq. (13) a calculated value of $R_r/R_s = 3.2$. This result is in fortuitously good agreement with the corresponding measured value of 3.02 ± 0.16 deduced from the data of Table 1.

V. CONCLUDING REMARKS AND SUMMARY

The excellent agreement between the theoretical and experimental values of R_r/R_s is, we believe, encouraging but as noted probably fortuitous given the fact that there are at least three major sources of discrepancy in the calculation. First, it is impossible to obtain an extended three-dimensional map of the Br distribution using the STEM because the sample stage has a relatively small translation range and because such a map would require extended acquisition times during which the microscope would be unavailable for other pressing experimental studies. As a result, the volume fraction of Br-poor regions is unknown and we are forced to overestimate the role played by these regions in limiting the macroscopic conductivity of the fiber. Second, the in-situ Br density distribution of the saturated fiber cannot be directly measured because the Br vapor pressure required to stabilize the saturated compound is incompatible with the ultra high vacuum environment of the STEM. Third, the linear relation between conductivity and Br composition given in Eq. 8 was based on measurements of natural graphite which was pitch-bound and heat-treated to 3000°C. This material is electrically distinct from PB fibers and in pristine form has a considerably larger resistivity of 1100 $\mu\Omega$ -cm compared to 253 $\mu\Omega$ -cm. Thus any attendant nonlinearity in the conductivity-density relation of Eq. (8) would contribute to an error in the calculated value of R_r/R_s .

We could, in principle have measured the absolute Br density profile of our fiber specimens. But such a measurement is fraught with difficulty in practice and involves a detailed knowledge of many experimental parameters such as detector collection efficiency, detector

window absorption, the takeoff angle for collection, the detailed X-ray line shape, the absolute electron beam current at the sample, etc. Fortunately, these factors which are presumed to be constant do not affect the relative intensity measurements which we have carried out here.

Additional comments on the measurement method used here are in order. Equation (2) shows that the beam broadening inside the material is inversely proportional to the energy of the electrons. This is the reason we used the maximum excitation energy available in the STEM to generate the X-ray spectrum. Obviously, the smaller the sample volume probed by the electron beam for a given lateral position, x , the higher is the spatial resolution of the X-ray profile measurement. Thus the use of a higher voltage microscope such as the commercially available 400kV machines would significantly improve the resolution. Furthermore, at higher energies the relative energy loss of the electron will be small and the ionization cross section $\theta(E)$ in Eq. (7) can be treated as energy independent. As a result the task of extracting ρ_{Br} from $I(x)$ would be greatly simplified.

Finally we note that the significance of the results reported here lies with the procedure outlined for relating the macroscopic relative resistance of the fiber to the microscopic distribution of the inserted Br. In principle, the accuracy of our procedure is limited only by the detail of the X-ray intensity profile.

VI. ACKNOWLEDGEMENTS

This work is done in collaboration with S.A. Solin and J.R. Gaier. We thank D.M. Hwang for several useful discussions and for providing a copy of the Monte Carlo program. We are also grateful to D. Jaworski for helpful comments and to V. Shull for valuable technical assistance. This work was supported by the National Aeronautics and Space Administration under grant #NAG-3-595. Partial support by Michigan State University through its internally funded Analytical Electron Microscope Laboratory, and by the the National Science Foundation under grant #DMR 85-17223 is also acknowledged.

References

1. L.S. Singer and I.C. Lewis, Carbon 16, 409(1978).
2. J.B. Donnet and R.C. Bansal, Carbon Fibers (Marcel Dekker, New York and Basel, 1984).
3. J.R. Gaier and D. Marino, NASA TM-87016, 1985.
4. C. Herinckx, R. Perret and W. Ruland, Carbon 10, 711(1972).
5. J.G. Hooley and V.R. Diets, Carbon 16, 251(1978).
6. T. Sasa, Bull. Chem. Soc. Japan 34, 43(1970).
7. M.S. Dresselhaus and G. Dresselhaus, Adv. in Phys. 30, 130(1980).
8. S.A. Solin, Adv. Chem. Phys. 49, 455(1982).
9. J.R. Gaier, NASA TM-86859, 1984.
10. J.R. Gaier and D.A. Jaworske, NASA TM-87025, 1985.
11. J.R. Gaier, NASA TM-87275, 1986.
12. J.R. Gaier, in Proceedings of the Materials Research Society Meeting, ed. by M.S. Dresselhaus, G. Dresselhaus and S.A. Solin (Boston, 1986).
13. V.E. Cosslett and R.N. Thoms, in The Electron Microprobe, edited by K.F.J. Heinrich and D.B. Wittry, (Wiley, New York, 1966).
14. L. Curgenven and P. Duncomb, Tube Investments Lab Reports, 303 (1971).
15. J.I. Goldstein, in Practical Scanning Electron Microscope, ed. by J.I. Goldstein and H. Yakowitz, Ch.3, (Plenum Press, New York and Landon, 1975).
16. D.C. Joy, unpublished.
17. J.I. Goldstein, in Introduction to Analytical Electron Microscopy, edited by J.J. Hern, J.I. Goldstein and D.C. Joy. (Plenum Press, New York and Landon, 1979).

18. C.J. Powell, NBS Special Publication 460, edited by K.F.J. Heinrich,
97(1976).

19. International Table for X-ray Crystallography, edited by C.H.
Macgillavry and G.D. Rieck, V.3, 162(1962).

APENDICES

Physics and Chemistry of Spatially Resolved Microdomains in SbCl_5 -Intercalated Graphite

D. M. Hwang^(a)

Department of Physics, University of Illinois at Chicago, Chicago, Illinois 60680

and

X. W. Qian and S. A. Solin

Department of Physics and Astronomy, Michigan State University, East Lansing, Michigan 48824

(Received 5 June 1984)

We report on the first spatially resolved study of the chemical and electronic properties of microdomains in molecular monolayers. Analytical electron-microscope measurements of stage-4 SbCl_5 -intercalated graphite show Sb-rich islands of lateral dimension 500–1000 Å. Energy-loss spectra yield a 6-eV graphite π plasmon modulated by the domain structure, but the 25-eV $\pi + \sigma$ plasmon and the carbon core excitations are spatially invariant. The derived island and background compositions are $(\text{SbCl}_3)_{1/18}(\text{SbCl}_4^-)_{1/32}$ and $(\text{SbCl}_3)_{9/16}(\text{SbCl}_4^-)_{9/32}$.

PACS numbers: 61.16.Di, 71.45.Gm, 82.65.-i

The study of the properties of quasi-two-dimensional (quasi-2D) molecular or atomic monolayers in the presence of a rigid substrate potential constitutes a fundamental problem of considerable current interest.¹ To date primary attention has been focused on the multiphase-multidomain structures and associated order-disorder phenomena² which such monolayers often exhibit. For many systems, and in particular the acceptor-type graphite intercalation compounds (GIC's), the microscopic chemical and physical properties can play a critical role in domain formation. Those properties have not yet been explored because conventional probes do not provide sufficient spatial resolution to examine individual domains directly. We report here the first analytical electron-microscope study of the physical and chemical properties of directly observed microdomains in quasi-2D molecular monolayers.

SbCl_5 -intercalated graphite was chosen for this study for several reasons. It is the most air stable of the GIC's known to date.³ Therefore, SbCl_5 -intercalated graphite has been examined by a myriad of conventional techniques⁴ and is easily transferred into an electron microscope. Diffraction studies⁵ show that SbCl_5 -intercalated graphite forms novel, in-plane microdomain structures, one of which is a glass phase.⁶

It has been proposed⁷ that SbCl_5 behaves chemically like AsF_5 ⁸ upon intercalation into graphite, and disproportionates into $(\text{SbCl}_3)_{1-x}(\text{SbCl}_3)_{x/3}(\text{SbCl}_4^-)_{2x/3}$, $0 \leq x \leq 1$. The SbCl_3 and SbCl_4^- species apparently form a complex in which the Cl^- ion is dynamically exchanged.⁷ There is also evidence for an SbCl_4^- disproportionation product.⁹

The uniformity of the distribution of these molecular species in the graphite galleries has not been established. Obviously, the microscopic homogeneity of disproportionation may affect both domain formation and the bulk electronic properties.

Stage-4 SbCl_5 -intercalated graphite was prepared from highly oriented pyrolytic graphite by the two-bulb technique. The samples were intercalated at an extremely low rate over a period of two months to avoid exfoliation and to maximize homogeneity.¹⁰ X-ray diffraction indicated that the stage purity was greater than 99%. Specimens were cleaved from the bulk, glued to a glass slide with water soluble glue, thinned with adhesive tape, floated off, and then picked up with microgrids. The measurements reported here were made with a 100-kV Vacuum Generators Model HB501 analytical scanning transmission electron microscope (STEM) equipped with a field-emission tip, digital beam control, a 30-mm² Li-drifted Si energy-dispersive x-ray detector, an annular dark-field detector (collection half-angle θ , $0.01 \text{ rad} \leq \theta \leq 0.05 \text{ rad}$), and an energy-loss spectrometer capable of 0.5-eV resolution. Spectrometer instability as determined by the variation of the width of the zero-loss peak of single short scans (< 400 ms) and summed multiple short scans (total acquisition time $\sim 5 \text{ min}$) was less than 0.2 eV.

A typical dark-field image of stage-4 SbCl_5 -intercalated graphite is shown in Fig. 1 and clearly exhibits high-density islands of dimension 500–1000 Å. Essentially identical bright-field images of the same region were also obtained. The islands occupied $(11 \pm 2)\%$ of the total imaged area. Energy-dispersive x-ray (EDX) spectra of the island

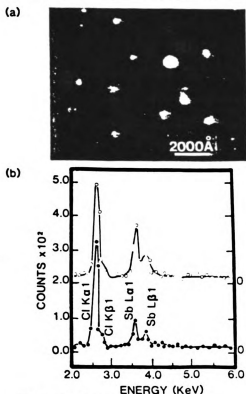


FIG. 1. (a) Dark-field STEM image of stage-4 SbCl_5 -intercalated graphite. (b) Energy-dispersive x-ray spectra of the island (open circles) and background (closed circles) regions.

and background regions (beam spot size $\approx 50 \text{ \AA}$) are shown in Fig. 1(b) in the range which incorporates the Cl K lines and the Sb L lines. We have used these lines to deduce the Sb:Cl ratio in the island and background regions following standard thin-specimen analysis procedures.¹¹ The composition in the island region is $\text{SbCl}_{1.1 \pm 0.3}$, while that of the background region is $\text{SbCl}_{1.0 \pm 0.2}$. The uncertainty in composition arises from the variation from island to island and background region to background region and from a statistical fluctuation associated with the relatively low count levels engendered by the need to limit sample contamination during signal acquisition. Note that our specimens have a nominal thickness of 500 \AA , which is less than the electron mean free path. Therefore structural differences of the island and background regions (see below) have a negligible effect on the EDX analysis. Moreover, the data reported here were acquired with a convergent electron beam ($2\alpha \approx 17 \text{ mrad}$) that generated many Bragg reflec-

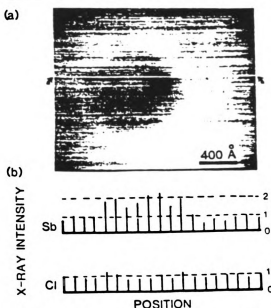


FIG. 2. (a) Bright-field image showing an island, the surrounding background, and a scan line (denoted by arrows). (b) Sb L -line and Cl K -line integrated x-ray intensities along the scan line.

tions. Thus the modulations in EDX signals or channeling effects associated with individual Bragg reflections observed with collimated incident beams were averaged out.¹¹ Accordingly we recorded STEM images that were insensitive to sample tilt angle¹¹ and the error in EDX analysis attributable to channeling was also negligible.

We propose that the islands are composed of Sb-rich $\text{SbCl}_3/\text{SbCl}_4^-$ -like material whereas the background consists of Sb-deficient $\text{SbCl}_2/\text{SbCl}_3^-$ -like material. To further verify this we refer to Fig. 2 which shows a digital-beam-control line scan across an island and the relative Sb L -line and Cl K -line signals acquired from such a scan. Note that Cl yields a constant signal and is thus uniformly distributed over the line of scan, whereas the Sb signal doubles in the region of the island. These observations are additionally confirmed by two-dimensional x-ray mapping studies of SbCl_3 GIC's.¹²

Preliminary microdiffraction studies¹³ show that the islands are disordered and yield diffuse rings, whereas the background exhibits a pattern which can be associated with a $(\sqrt{7} \times \sqrt{7})R19.1^\circ$ structure and some as yet unindexed additional spots. These results indicate that the island and background regions extend through the (uniform) thickness of the sample with the former adopting an irregularly

shaped columnar structure which gives rise to the high-contrast dark- and bright-field images of Figs. 1 and 2, respectively. This columnar structure which might be directly imaged with cross-sectioned samples can be attributed to a nucleation process which is driven by the dipole strain field¹⁴ associated with the intercalate intraplane and interplanar interaction. The nucleation density, the equilibrium of disproportionation, and defects intrinsic to the graphite itself all influence island formation. The interaction between these several effects is extremely complex and difficult to quantify.

By examining the electron energy-loss spectra (EELS) we have probed the effect of chemical segregation on the electronic band structure of stage-4 SbCl_5 -intercalated graphite. The EELS obtained from selected spots in the island and background regions with momentum transfer $q \approx 0$ are shown in Fig. 3. In the 0–10-eV range these spectra are very similar to the EELS calculated by Eklund *et al.*¹⁵ from optical measurements of the complex dielectric function of stage-4 SbCl_5 -intercalated graphite. We have observed, but not resolved, the intraband plasmon at ≈ 1 eV.

As can be seen from Fig. 3, the broad $\pi + \sigma$ electron peak at ≈ 25 eV is essentially independent of the acquisition region whereas the π plasmon peak at ≈ 6 eV shows a 17% intensity decrease and a possible slight energy upshift for the island region relative to the background. This upshift, though small, is nevertheless observable as a relative change in EELS patterns which are themselves internally referenced to the zero-loss peak. (The π

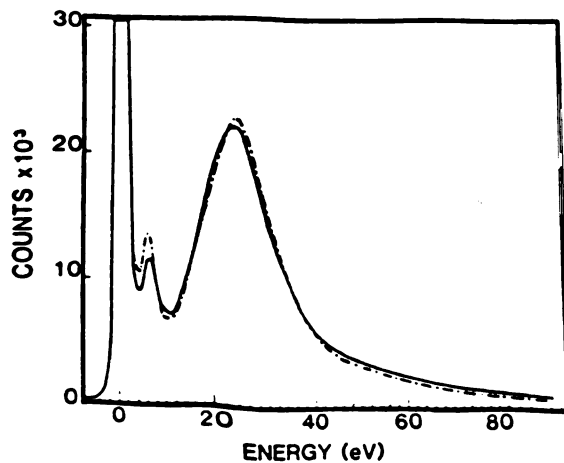


FIG. 3. Plasmon electron energy-loss spectra of the island (solid line) and background (dashed line) regions acquired with a spectrometer resolution of 1 eV.

and $\pi + \sigma$ plasmon peaks occur at 7 and 25 eV, respectively, in pristine graphite.) Moreover, the EELS of islands ranging in lateral size from 500 to 1000 Å were indistinguishable. Therefore, the analyzed regions of our specimens were sufficiently thick and uniform to render negligible configuration-effect contributions¹⁶ to the 17% variation of the 6-eV plasmon intensity. Note also that the spectra of Fig. 3 show no trace of the $\pi + \sigma$ plasmon multiple-scattering peak at ≈ 50 eV which is usually seen in thicker specimens. We have also recorded carbon 1S-core-excitation EELS from the island and background regions.¹² These spectra are indistinguishable and exhibit a broad peak at 289 eV and a weak, sharper peak at 281 eV. Such features are typical of acceptor GIC's.¹⁷

The gross downshift and marked intensity reduction in the 6-eV plasmon of GIC's relative to pristine graphite is due to the reduction in oscillator strength of the 4.5-eV $\pi - \pi^*$ transition associated with the reduced number of carbon layers per unit volume in the intercalated material.¹⁷ The reduced intensity of the 6-eV plasmon of the island relative to the background evidenced in Fig. 3 has a more subtle origin related to the detailed energy band structure of different intercalant domains.

Any intercalant interband transition of lower energy than 4.5 eV will lower the intensity of the 6-eV plasmon. This effect is more pronounced if the transition is close in energy to 4.5 eV and/or has a larger oscillator strength. We expect the interband transitions closest to but lower in energy than the 4.5-eV transition to derive from $\text{SbCl}_3/\text{SbCl}_4^-$ since these molecules are more tightly bound than $\text{SbCl}_2/\text{SbCl}_6^-$. Therefore, the 6-eV plasmon of the island should be less intense than the corresponding plasmon of the background. In contrast, the σ electrons of graphite are much more localized and more tightly bound than the π electrons. They are less perturbed by the intercalant and the $\pi + \sigma$ plasmon is insensitive to the chemical differences between the island and background regions.

The spatial invariance of the carbon 1S core excitation,¹² particularly with regard to the intensity of the 281-eV satellite peak indicates that, within our experimental accuracy, the island and background regions have the same Fermi energy shift with respect to the rigid carbon electronic bands and thus the same carbon layer charge density. This charge delocalization in conjunction with the island area occupancy of 11% and the uniform Cl distribution leads¹² to a unique intercalant macroscopic chemical composition $(\text{SbCl}_3)_{1/8}(\text{SbCl}_4^-)_{1/32}(\text{SbCl}_2)_{9/16}(\text{SbCl}_6^-)_{9/32}$. The microscopic stoichiometries are

then $\text{SbCl}_{3,2}$ in the islands and $\text{SbCl}_{3,33}$ in the background, and the degree of the disproportionation is 0.44. The charge transfer per SbCl_5 molecule is 0.31 (0.0055 hole per carbon atom based on the composition of $\text{C}_{4 \times 14} \text{SbCl}_5$), well within the range of reported values.^{9,18} Note that the derived chemical composition is in reasonable agreement with Mössbauer studies of the stage-2 compound which give $\text{SbCl}_4^-:\text{SbCl}_3$ and $\text{SbCl}_6^-:\text{SbCl}_3$ ratios of 0.25 and 1.9, respectively, but indicate a higher degree of disproportionation.

We are grateful to P. Eklund for providing optical data prior to publication and for useful conversations. The technical assistance of V. Shull was invaluable. We thank A. W. Moore of Union Carbide for providing pyrolytic graphite. This research has been supported by the National Science Foundation through Grant No. DMR83-11154, by Michigan State University through its internally funded Analytical Electron Microscope Laboratory, and by the Research Board of the University of Illinois at Chicago.

^(a)Present address: Bell Communications Research, Murray Hill, N.J. 07974.

¹See, e.g., *Ordering in Two Dimensions*, edited by S. K. Sinha (Elsevier-North-Holland, New York, 1980).

²S. A. Solin, *Adv. Chem. Phys.* **49**, 455 (1982).

³V. R. K. Murthy, D. S. Smith, and P. C. Eklund, *Mater. Sci. Eng.* **45**, 77 (1980).

⁴See for example "Graphite Intercalation Compounds," edited by S. Tanuma and H. Kamimura, sum-

mary report of project No. 56122027 of the Ministry of Education, Science, and Culture, Japan, March 1984 (unpublished).

⁵R. Clarke, M. Elzinga, J. N. Gray, H. Homma, D. T. Morelli, M. J. Winokur, and C. Uher, *Phys. Rev. B* **26**, 3312 (1982).

⁶G. Timp, M. S. Dresselhaus, L. Salamanca-Riba, A. Erbil, L. W. Hobbs, G. Dresselhaus, P. C. Eklund, and Y. Iye, *Phys. Rev. B* **26**, 2323 (1982).

⁷L. B. Ebert, D. R. Mills, and J. C. Scanlon, *Mater. Res. Bull.* **18**, 1505 (1983).

⁸N. Bartlett, R. N. Biagioni, B. W. McQuillan, A. S. Robertson, and A. C. Thompson, *J. Chem. Soc. Chem. Commun.* **1978**, 200.

⁹P. Boolchand, W. J. Bresser, D. McDaniel, K. Sisson, V. Yeh, and P. C. Eklund, *Solid State Commun.* **40**, 1049 (1981).

¹⁰D. M. Hwang and G. Nicolaidis, *Solid State Commun.* **49**, 483 (1984).

¹¹*Introduction to Analytical Electron Microscopy*, edited by J. J. Hren, J. I. Goldstein, and D. C. Joy (Plenum, New York, 1979). Also, D. Cherns, A. Howie, and M. H. Jacobs, *Z. Naturforsch.* **28A**, 565 (1973); P. Duncumb, *Philos. Mag.* **7**, 2101 (1962).

¹²D. M. Hwang, X. W. Quan, and S. A. Solin, to be published.

¹³D. M. Hwang and J. Cowley, unpublished.

¹⁴S. A. Saffran and D. P. Hamann, *Phys. Rev. Lett.* **42**, 1410 (1979).

¹⁵P. C. Eklund, D. M. Hoffman, G. L. Doll, and R. E. Heinz, to be published.

¹⁶P. E. Batson, in *Proceedings of the Thirty-Eighth Annual Electron Microscopy Society of America Meeting*, edited by G. W. Baily (Claitor's, Baton Rouge, 1980), p. 124; P. E. Batson and M. M. J. Treacy, *ibid.*, p. 126.

¹⁷J. J. Ritsko and E. J. Mele, *Synth. Met.* **3**, 73 (1981).

¹⁸R. E. Heinz, G. Doll, P. Charron, and P. C. Eklund, *Mat. Res. Soc. Symp. Proc.* **20**, 87 (1983).

Molecular Clustering in a Two-Dimensional Metal-Ammonia Solution

X. W. Qian, D. R. Stump, B. R. York,^(a) and S. A. Solin

Department of Physics and Astronomy, Michigan State University, East Lansing, Michigan 48824

(Received 21 November 1984)

We have measured the in-plane x-ray diffraction pattern of the two-component K^+ - NH_3 liquid layers in the ternary graphite intercalation compound $K(NH_3)_{4.33}C_{24}$. The measured pattern is in semiquantitative agreement with the scattering calculated for a random distribution of coplanar hard K^+ and NH_3 disks, provided that the K^+ ions are bound symmetrically to four NH_3 molecules. We show that the K - NH_3 layers constitute the two-dimensional structural analog of the well-known bulk three-dimensional K - NH_3 metal-ammonia solutions.

PACS numbers: 61.25.Em, 61.10.-i

During the past decade there have been numerous studies of the structures and structural phase transitions of atomic, ionic, and molecular monolayers which have been either adsorbed¹ on or intercalated between² the layers of graphite. Much attention has been devoted to solid-liquid transitions in the quasi-two-dimensional guest layer and to novel disordered phases such as the liquid states associated with melting^{2,3} and wetting.³ The two-dimensional (2D) liquid state has usually been inferred from the temperature, pressure, and/or coverage dependence of the width and shape of selected diffraction peaks.¹⁻³ In only one case (KC_{24}),⁴ to our knowledge, has a complete 2D liquid scattering intensity been calculated and compared with experiment. The calculated pattern reproduced some of the experimental features but was based on a structure which is not consistent with recent diffraction studies.⁵ In this Letter we present a successful calculation of the full diffraction pattern from a 2D liquid, the two-component K - NH_3 solution which occupies the galleries between graphite layers in the stage-1 ternary graphite intercalation compound (GIC) $K(NH_3)_{4.33}C_{24}$. The K - NH_3 layers in $K(NH_3)_{4.33}C_{24}$ constitute the 2D structural analog of the heavily studied bulk metal-ammonia solutions.⁶ Furthermore, their 2D liquid scattering intensity is surprisingly sensitive to the formation of particular types of K - NH_3 clusters.

Samples of $K(NH_3)_{4.33}C_{24}$ were prepared by exposing stage-2 KC_{24} (derived from highly oriented pyrolytic graphite) to NH_3 vapor at a pressure ≈ 10 atm. Details of sample preparation and of the x-ray apparatus used for the measurements reported here are given elsewhere.⁷

The in-plane $q \perp C$ diffuse scattering intensity for $K(NH_3)_{4.33}C_{24}$ is shown as a dotted line in Fig. 1. This pattern, $I_{\perp}(q)$, has been corrected⁸ for the Lorentz-polarization factor, absorption, and for all background effects. The ordinate scale in Fig. 1 was established in the usual way by fitting the diffraction profile at high q to the calculated sum of the Compton and coherent scattering contributions.⁸ Also the intense Bragg reflections of the graphite host layers have been re-

moved from $I_{\perp}(q)$ for clarity. As can be seen from Fig. 1, $I_{\perp}(q)$ is characterized by a relatively sharp peak at $q = 0.88 \text{ \AA}^{-1}$ followed by a broad asymmetric intense peak centered at $q = 2.07 \text{ \AA}^{-1}$ and another broad weak feature at $q \approx 4.24 \text{ \AA}^{-1}$.

We now discuss a structural model which semiquantitatively accounts for the in-plane scattering intensity of the K - NH_3 2D liquid intercalant in $K(NH_3)_{4.33}C_{24}$. We assume that the NH_3 molecules and the K^+ ions can be represented as coplanar hard disks. If r_m is the position of the center of the m th particle (i.e., NH_3 or K^+ disk) and f_m its q -dependent scattering factor, where $f_{NH_3}(0) = 10$ and $f_{K^+}(0) = 18$, then the scattered intensity for any distribution of disks will be

$$I(q) = \sum_m f_m \exp(iq \cdot r_m) \sum_n f_n^* \exp(-iq \cdot r_n). \quad (1)$$

Let there be L layers of K - NH_3 in the scattering volume with N particles (disks) in each layer. Then if

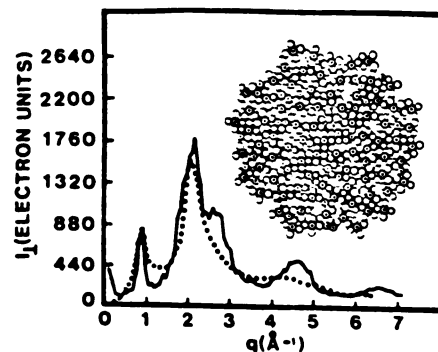


FIG. 1. The calculated (solid line) in-plane diffraction patterns of the K - NH_3 liquid in $K(NH_3)_{4.33}C_{24}$ scaled at $q = 0.88 \text{ \AA}^{-1}$ to the measured room-temperature (dotted line) pattern. The calculated pattern was deduced by applying Eq. (4) of the text to the fourfold coordinated distribution shown in the inset which depicts K^+ ions (circles with pluses) bound to four NH_3 ions (circles) and unbound NH_3 ions (circles with dots). The parameters used were $r_{max} = 2.00 \text{ \AA}$, $r_{min} = 1.30 \text{ \AA}$, $\delta r = 0.23 \text{ \AA}$, and $r_{K^+} = 1.46 \text{ \AA}$.

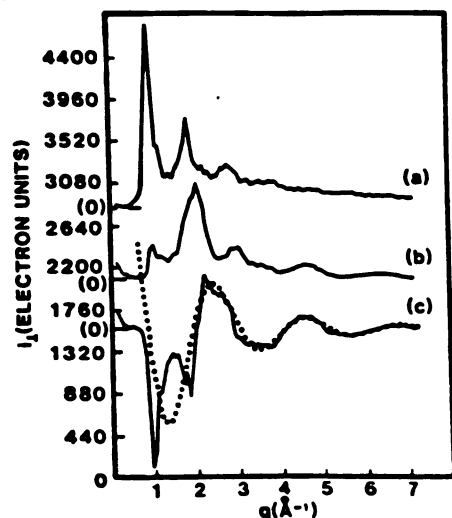


FIG. 2. The (a) K^+-K^+ , (b) NH_3-NH_3 , and (c) K^+-NH_3 in-plane pair-scattering functions calculated using the parameter set given in the caption of Fig. 1, Eq. (4), and the distribution shown in the inset of Fig. 1. The dots are a plot of $J_0(q \times (R_{nm} = 2.89 \text{ \AA}))$ (see text).

The total calculated in-plane scattering intensity is the sum of the pair scattering profiles, i.e., $I_L(q) = i_L^{K^+-K^+}(q) + i_L^{NH_3-NH_3}(q) + i_L^{K^+-NH_3}(q)$. These individual pair contributions are quite revealing as can be seen from Fig. 2. The sharp peak in $I_L(q)$ at 0.88 \AA^{-1} results from the dominance of the K^+-K^+ contribution over the K^+-NH_3 contribution of opposite sign at that q value. The former results from the fact that the K^+-K^+ nearest-neighbor distances show little variation in the fourfold coordinated distribution as is evident from the inset of Fig. 1. The sharp negative K^+-NH_3 contribution at 0.88 \AA^{-1} results from the fact that the ammonia and potassium disks have roughly the same diameter. Also note from Fig. 2(c) that the K^+-NH_3 contribution consists of correlations superposed on $J_0(q \times (R_{nm} = 2.89 \text{ \AA}))$. This Bessel-function background results from the presence of many K^+-NH_3 near-neighbor pairs separated by 2.89 \AA in the fourfold coordinated distribution. It is evident from Fig. 2(c) that the Bessel-function contribution is responsible for the enhanced amplitude of $I_L(q)$ at the high- q shoulder of the 2.07 \AA^{-1} peak and at the 4.24 \AA^{-1} peak. These enhancements represent a minor deficiency in our model which we associate with its oversimplified structural character.

The physical size of the NH_3 molecules limited to four the number which could be symmetrically bound to potassium in a planar configuration. Therefore, as noted above we tried to fit the data of Fig. 1 with distributions having $n < 4$. Two such distributions with

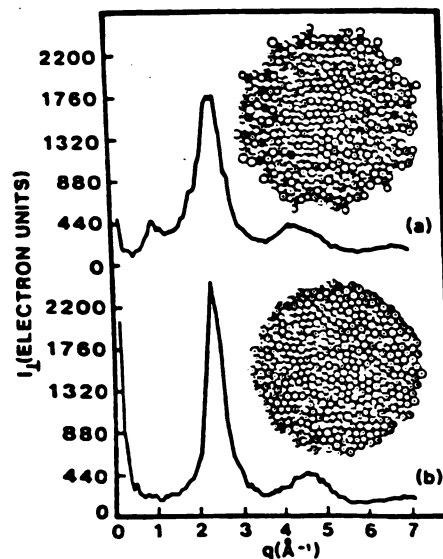


FIG. 3. The calculated in-plane diffraction patterns for the threefold coordinated $K-NH_3$ distributions [(a) and inset] with parameters $r_{max} = 2.00 \text{ \AA}$, $r_{min} = 1.30 \text{ \AA}$, $\delta r = 0.30 \text{ \AA}$, and $r_{K^+} = 1.33 \text{ \AA}$ and the zerofold coordinated, free ammonia, distribution [(b) and inset] with parameters $r_{max} = 2.00 \text{ \AA}$, $r_{min} = 1.30 \text{ \AA}$, $\delta r = 0.30 \text{ \AA}$, and $r_{K^+} = 1.33 \text{ \AA}$. The symbols used for the insets are the same as in Fig. 1.

$n = 3$ and $n = 0$ are shown together with their corresponding best fits in Figs. 3(a) and 3(b), respectively. It is obvious from Fig. 3 that these other distributions yield fits inferior to the $n = 4$ fit, particularly with regard to the sharp peak at 0.88 \AA^{-1} , and that the observed diffraction pattern is quite sensitive to the cluster coordination.

The real 2D $K-NH_3$ liquid is dynamic and almost certainly contains $K-NH_3$ clusters with differing coordination number. We could have accounted for this effect by introducing several additional fitting parameters to characterize the probability $P(n)$ of finding an n -fold coordinate cluster in the liquid. Even more parameters could have been introduced to model asymmetries in the angular distributions of the NH_3 molecules about the K^+ cores. While such procedures would improve the fit to the data of Fig. 1, they would also tend to mask the essential structural features of the 2D $K-NH_3$ liquid. These are the predominance of the symmetric fourfold coordinated cluster and the distribution in tilt angles for the C_3 axes of the NH_3 molecules. It is not surprising that the simple model we have employed does not yield a fully quantitative fit to the data of Fig. 1. But it is significant that this model produces as good a semiquantitative fit as is observed.

a_z is the C axis repeat distance and $r_m = R_{mS} + Sa_z \hat{k}$ for the S th layer, Eq. (1) can be rewritten as

$$I(q) = L \sum_{m,n} f_{mS} f_{nS}^* \exp[iq \cdot (R_{mS} - R_{nS})] + \sum_{m,n} \sum_{S,S'} f_{mS} f_{nS'}^* \exp[iq \cdot (R_{mS} - R_{nS'})] \exp[iq \cdot (S - S') a_z \hat{k}] \quad (2)$$

which for in-plane scattering with $q = q\hat{x}$ becomes

$$I_{\perp}(q) = L \sum_{m,n} f_{mS} f_{nS}^* \exp[iq(x_{mS} - x_{nS})] + \sum_{m,n} \sum_{S,S'} f_{mS} f_{nS'}^* \exp[iq(x_{mS} - x_{nS'})]. \quad (3)$$

If there is no interlayer correlation, i.e., x_{mS} and $x_{nS'}$, are uncorrelated, the second term in Eq. (3) is equal to zero. We have verified the lack of interlayer correlation in $K(\text{NH}_3)_{4.33}\text{C}_{24}$ by recording "flat"² ($hk = \text{const}$, l) c^* x-ray scans.⁹ For a sufficiently large system which is amenable to cylindrical averaging, the first term in Eq. (3) can be recast in the familiar² form

$$I_{\perp}(q) = L \sum_{m,n} f_m f_n^* J_0(qR_{mn}), \quad (4)$$

where $R_{mn} = |R_m - R_n|$, J_0 is the zeroth-order Bessel function, and we have dropped the subscript S . The second term in Eq. (3), which has been omitted in previous treatments of in-plane diffuse scattering,^{10,11} can significantly influence both the calculated $I_{\perp}(q)$ ¹¹ and the pair correlation function deduced from the Bessel transform of the observed $I_{\perp}(q)$ ¹⁰ if interlayer correlations are non-negligible. Such correlations may be present in a lattice gas model¹¹ of GIC structure and in a system that is about to undergo a 2D-3D order-disorder transition.²

In order to account for the observed diffraction pattern $I_{\perp}(q)$ shown in Fig. 1 we have applied Eq. (4) to several computer generated structural distributions of K and NH_3 disks. Because K^+ ions can effectively polarize and bind up to six NH_3 molecules⁶ we concentrated on distributions of symmetric planar n -fold coordinated clusters. For reasons which will be made clear below, $n \leq 4$. In order to satisfy the stoichiometry of our specimens, each distribution contained exactly 500 K^+ disks and 2165 NH_3 disks. In an n -

fold coordinated distribution each K^+ disk was in contact with n NH_3 disks such that the lines of centers between the K^+ and NH_3 disks make equal angles of $2\pi/n$.

An n -fold coordinated distribution was generated as follows: A seed cluster was nucleated around a K^+ by symmetrically attaching n NH_3 disks with different radii randomly selected from a Gaussian distribution (see below). Then a K^+ or NH_3 disk was randomly selected from the remaining collection of 499 K^+ disks and 2165 NH_3 disks. If the selection yielded a K^+ disk, n NH_3 disks were attached to it and the rigid cluster was moved, in a series of small translational and rotational steps, towards the seed cluster until the distance between the K^+ centers of the seed and the added cluster was minimized. If the next randomly selected particle was an NH_3 disk it was moved in a series of translational steps until it was as close as possible to the center of the seed cluster. The above described process was repeated until all of the particles had been assembled.

It is known from NMR measurements¹² that at room temperature the NH_3 molecules spin rapidly about their C_3 axes which in turn are tilted with respect to the graphite C axis. The tilt angle varies rapidly in time such that at any instant there is a distribution in the orientations of the NH_3 molecules. Thus the cylindrical projections, of the surfaces of revolution about the C_3 axes onto the graphite basal plane, have a distribution in radii which we have modeled on the basis of NMR measurements¹² as

$$P(r) \propto \exp[-(r - r_{\min})^2/(\delta r)^2] - \exp[-(r_{\max} - r_{\min})^2/(\delta r)^2],$$

where $r_{\max} = 2.00 \text{ \AA}$, $r_{\min} = 1.30 \text{ \AA}$, $r_{\min} \leq r \leq r_{\max}$, and $0 \leq \delta r \leq 0.3 \text{ \AA}$. The radii of all K^+ ions in a distribution were fixed at a value r_{K^+} approximately equal to the ionic radius of potassium. For each n -fold coordinated distribution the parameters δr and r_{K^+} were varied to achieve the best fit to the data of Fig. 1 using Eq. (4). The fits obtained were quite sensitive to r_{K^+} and n , but were relatively insensitive to the other parameters and were size independent, i.e., macroscopic, for distributions containing more than 50 K^+ disks.

The fourfold coordinated distribution shown in the

inset of Fig. 1 yielded the best fit (solid line) to the data. Notice that the amplitudes, positions, and widths of the features of the measured $I_{\perp}(q)$ are reasonably accounted for, the only exceptions being the shoulder on the high- q side of the 2.07-\AA^{-1} peak and the peak at $\approx 4.24 \text{ \AA}^{-1}$. Also note that the theoretical areal density calculated from the distribution shown in the inset of Fig. 1 is equal, within experimental error, to the experimentally determined density. This is not the case, for example, for the distribution of Fig. 3(b) even though the same stoichiometry obtains.

The success of the $n=4$ distribution is in part a manifestation of the structure of 3D metal-ammonia solutions.⁶ For bulk K-NH₃ liquids, the K⁺ ion is octahedrally (sixfold) coordinated to NH₃. But the gallery height in K(NH₃)_{4.33}C₂₄ is such that only a monolayer of NH₃ molecules can occupy the interlayer space.⁷ The resultant fourfold coordinated planar K⁺-NH₃ cluster is derived from the octahedron by the removal of two apical ammonia molecules. Thus it is evident that the K-NH₃ layers in K(NH₃)_{4.33}C₂₄ do indeed constitute the 2D structural analog of a bulk K-NH₃ solution.

As a final point, we note that to date the structures of all 2D "liquids" intercalated into graphite have been dominated by the host potential.⁵ The 2D liquid-like character was a minor feature in comparison to the role played by substrate-induced registry, modulations, etc. In contrast, the K-NH₃ layers intercalated into graphite are essentially simple 2D liquids at room temperature. Substrate effects, though no doubt present, are of secondary importance.

We thank S. D. Mahanti and Y. B. Fan for useful discussions and kindly thank A. W. Moore of Union Carbide Corporation for providing graphite. This work was supported in part by the National Science Foundation under Grant No. DMR82-11554.

⁽⁶⁾Present address: IBM San Jose Research Laboratory, San Jose, Cal. 95114.

¹*Ordering in Two Dimensions*, edited by S. K. Sinha (North-Holland, New York, 1980).

²S. A. Solin, *Adv. Chem. Phys.* **49**, 455 (1982).

³M. Wortis, R. Pandit, and M. Schick, in *Melting, Localization, and Chaos*, edited by R. Kalia and P. Vashista (Elsevier, Lausanne, 1982), p. 13.

⁴M. Plischke and W. D. Leckie, *Can. J. Phys.* **60**, 1139 (1982).

⁵R. Clarke, J. N. Gray, H. Homma, and M. J. Winokur, *Phys. Rev. Lett.* **47**, 1407 (1981).

⁶J. C. Thompson, *Electrons in Liquid Ammonia* (Clarendon, Oxford, 1976).

⁷B. R. York, S. K. Hark, and S. A. Solin, *Solid State Commun.* **50**, 595 (1984); B. R. York and S. A. Solin, *Phys. Rev. B* (to be published).

⁸H. P. Klug and L. E. Alexander, *X-Ray Diffraction Procedures for Polycrystalline and Amorphous Materials* (Wiley, New York, 1974).

⁹D. Stump, X. W. Qian, B. R. York, and S. A. Solin, to be published.

¹⁰R. Clarke, N. Caswell, S. A. Solin, and P. M. Horn, *Phys. Rev. Lett.* **43**, 2018 (1979).

¹¹H. Zabel, Y. M. Jan, and S. C. Moss, *Physica (Utrecht)* **99B**, 453 (1980).

¹²H. Resing, B. R. York, and S. A. Solin, *Bull. Am. Phys. Soc.* **29**, 294 (1984), and to be published.

ION SIZE EFFECTS IN ALKALI-AMMONIA TERNARY GRAPHITE INTERCALATION COMPOUNDS

S.A. SOLIN, Y.B. FAN and X.W. QIAN

Department of Physics and Astronomy, Michigan State University, East Lansing, MI 48824-1116 (U.S.A.)

ABSTRACT

The dependence of the composition and sandwich thickness of $M(\text{NH}_3)_x\text{C}_{24+\Delta}$, $M = \text{K, Rb, Cs}$, stage-1 alkali-ammonia ternary graphite intercalation compounds on ion size has been determined using (00 l) x-ray diffraction measurements together with both gravimetric and volumetric measurements of NH_3 weight uptake. The measured compositions can be quantitatively accounted for with a three-dimensional (3D) "volume available" model similar to the Setton model for the molecular composition dependence of $\text{K}(\text{molecule})_x\text{C}_{24}$ provided a packing fraction α_{3D} is introduced. We find that $\alpha_{3D} = 0.35$ and that the effective ammonia radius is $r_A = 1.50 \text{ \AA}$. A two-dimensional (2D) model fails to yield reasonable results.

INTRODUCTION

Ternary alkali-ammonia graphite intercalation compounds (GICs) were first prepared by Rüdorff and coworkers¹ about four decades ago, but only recently have these materials attracted the attention of physicists and physical chemists. This attention was stimulated primarily by two factors. First and foremost, it was suspected that alkali-ammonia GICs would be the 2D structural analogues of bulk 3D metal-ammonia solutions.^{2,3} This suspicion has recently been confirmed in the case of potassium-ammonia GICs.⁴ Bulk metal-ammonia solutions are the classic systems for the study of the metal-insulator transition.⁵ Thus, the alkali-ammonia GICs may constitute a novel system for the study of the metal-insulator transition in 2D. The second stimulus for interest in alkali-ammonia GICs was the realization that the intercalant layer may represent a simple 2D liquid in the graphite gallery^{4,6} in contrast to the much more complex disordered structures exhibited by binary alkali GICs.⁷ This second stimulus has also been justified by recent x-ray diffraction studies of potassium-ammonia GICs.⁴

Rudörf and coworkers apparently concluded from their early studies of alkali-ammonia GICs that their (structural) properties, e.g. the sandwich thickness of the galleries, were determined by the NH_3 species and that the alkali metal was incidental.¹ Preliminary x-ray⁸ and NMR⁹ studies of the K, Rb, and Cs metal-ammonia GICs indicated the contrary. Accordingly, in this paper we report the results of x-ray diffraction studies of the metal ion size effects in ternary metal-ammonia GICs. Collaterally, the work which we report here represents the first study of cation size effects in any ternary GIC system whereas molecular size effects in potassium-molecular ternary GICs have been extensively studied by Setton and coworkers.¹⁰

EXPERIMENTAL

Pure stage-1 alkali-ternary GICs of K, Rb, and Cs were prepared by exposing the HOPG-derived (Highly Oriented Pyrolytic Graphite) stage-2 binary compounds $\text{MC}_{24+\Delta}$, $-2.5 \leq \Delta \leq 0.6$ to pure NH_3 vapor at a pressure of ~ 8.5 atm. The value of $\Delta \neq 0$ was measured by direct weighing of the binary compound and is indicative of its non-stoichiometric character. The x compositions of the ternary compounds $\text{M}(\text{NH}_3)_x \text{C}_{24+\Delta}$, $\text{M} = \text{K, Rb, Cs}$ were determined by both gravimetric and volumetric techniques using the apparatus shown schematically in Fig. 1 [here x equals the moles of NH_3 absorbed by the binary compound per mole of potassium]. In the former method, a quartz spring (spring constant ~ 1 mgm/mm) McBain balance⁴ was used in conjunction with a Cathetometer to obtain an absolute accuracy of 20 μgm corresponding to an x accuracy of ± 0.05 . Further details of the McBain balance measurement are given elsewhere.⁶

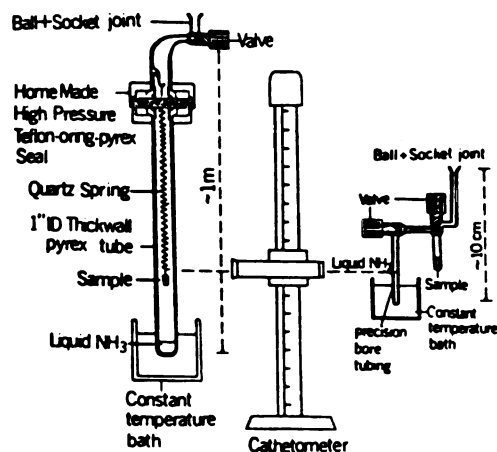


Fig. 1. Schematic diagrams of the apparatus for gravimetric (left panel) and volumetric (right panel) measurements of x in $\text{K}(\text{NH}_3)_x \text{C}_{24+\Delta}$ alkali-ternary GICs.

The apparatus shown schematically on the right of Fig. 1 was used for the volumetric measurement of x and also for the (001) x-ray determination of the sandwich thicknesses d_s . To determine x volumetrically, the change in height of liquid NH_3 in the precision bore tubing was determined when the binary GIC was exposed to NH_3 vapor. Correction was made for the height change associated with the NH_3 gas that fills the sample space. From the measured change in height of the NH_3 liquid, its known density and the bore size of the capillary tube, the value of x in $\text{K}(\text{NH}_3)_x\text{C}_{24+\Delta}$ could be determined to an accuracy of ± 0.1 .

RESULTS AND DISCUSSION

The results of our measurements of x , Δ , and d_s for $\text{M}(\text{NH}_3)_x\text{C}_{24+\Delta}$ are given in Table 1. The values for the latter will be discussed in detail elsewhere,¹³ but show a clear, if small, systematic dependence of d_s on ion size. These results are qualitatively compatible with recent NMR studies¹³ which relate the change in d_s to the orientation of the NH_3 molecules in the graphite gallery.

We now focus our attention on the variation of x with the alkali-metal ionic radii which are tabulated in the row labeled r_{M^+} in Table 1. Setton and coworkers have shown that the approximate value of x for potassium-molecular ternary GICs $\text{K}(\text{molecule})_x\text{C}_{24}$ can be deduced from a very simple model¹⁰ and that this model is remarkably successful for a large variety of molecules.

Table 1. Parameters of the 3D "volume available" and 2D "area available" models for ternary alkali-ammonia GICs $\text{M}(\text{NH}_3)_x\text{C}_{24+\Delta}$. The parameters x , $\langle\Delta\rangle$, and d_s (at 20°C) were experimentally measured. Values for r_{M^+} were obtained from the literature¹² and r_A , the effective radius of the ammonia molecule, α , the packing fraction, and cc , the correlation coefficient of the least-squares fits to Eqs. (4) and (6), were deduced using the models described in the text.

	K	Rb	Cs
x	4.33 ± 0.05	4.10 ± 0.05	3.65 ± 0.05
$\langle\Delta\rangle$	-0.6	-0.7	-0.5
d_s	$(6.620 \pm 0.005) \text{ \AA}$	$(6.640 \pm 0.005) \text{ \AA}$	$(6.671 \pm 0.005) \text{ \AA}$
r_{M^+}	1.33	1.46	1.67
$r_{M^+}^2$	1.77	2.13	2.79
$r_{M^+}^3$	2.35	3.11	4.66
	<u>2D Model</u>	<u>3D Model</u>	
r_A	1.22 \text{ \AA}	1.50 \text{ \AA}	
α	0.41	0.35	
cc	0.99986	0.99995	

Specifically, Setton showed that if V_1 is the volume available for all intercalant species in a gallery of height d_s and crosssection corresponding to $(24+\Delta)$ carbon atoms, then

$$V_1 = (24+\Delta) \frac{a^2\sqrt{3}}{4} [d_s - 3.35]A^3 \quad (1)$$

where $a = 2.46 \text{ \AA}$ is the lattice parameter of graphite and 3.35 \AA is the Van der Waals radius of a carbon atom. Now in Setton's model

$$V_1 = V_K + xV_{\text{molecule}} \quad (2)$$

where V_K is the volume of the potassium ion which depends on its ionic radius and V_{molecule} is the effective volume of the molecule. Finally, by establishing V_{molecule} independently (e.g. from the density of the molecular liquid) the value of x in $K(\text{molecule})_x C_{24}$ could be deduced from a combination of Eqs. (1) and (2)

$$x = \frac{V_1 - V_K}{V_{\text{molecule}}} \quad (3)$$

For our case in which the molecule NH_3 is kept fixed and the metal ion is varied, the equivalent form of Eq. (2) of Setton's 3D model is

$$\alpha_{3D} (24+\Delta) \frac{a^2\sqrt{3}}{4} (d_s - 3.35) = \frac{4}{3} \pi r_{M^+}^3 + x \left(\frac{4}{3} \pi r_A^3 \right) \quad (4)$$

where α_{3D} is a packing fraction (assumed = 1 by Setton), r_{M^+} is the ionic radius of the singly ionized metal and r_A is the effective radius of the intercalated ammonia molecule. If in addition to the assumption of complete charge exchange we make the reasonable approximations $\langle \Delta \rangle = 0$ and $\langle d_s \rangle = 6.65 \text{ \AA}$, then a plot of $r_{M^+}^3$ vs. x [see Table 1] should be linear and should yield the values of α_{3D} and r_A . Such a least-squares plot is shown in the lower panel of Fig. 2. This plot is clearly linear and the deduced value of $r_A = 1.50 \text{ \AA}$ is in excellent agreement with the effective ammonia radius of 1.48 \AA deduced from diffuse in-plane x-ray diffraction studies of $K(\text{NH}_3)_{4.33} C_{24}$. Moreover, the deduced packing fraction $\alpha = 0.31$ is quite reasonable since Setton's model¹⁰ underestimates V_1 by not including the cavity volume available in the lateral spaces between carbon atoms in the same layer.

The effective ammonia radius found in the x-ray studies cited above⁴ was based on a two-dimensional planar disc model for the structure of the 2D potassium-ammonia liquid. It is therefore appropriate to test the 2D analogue of Setton's 3D model. This 2D version can be simply written as equations (5) and (6) which follow:

$$A_1 = A_{M^+} + xA_{\text{molecule}} \quad (5)$$

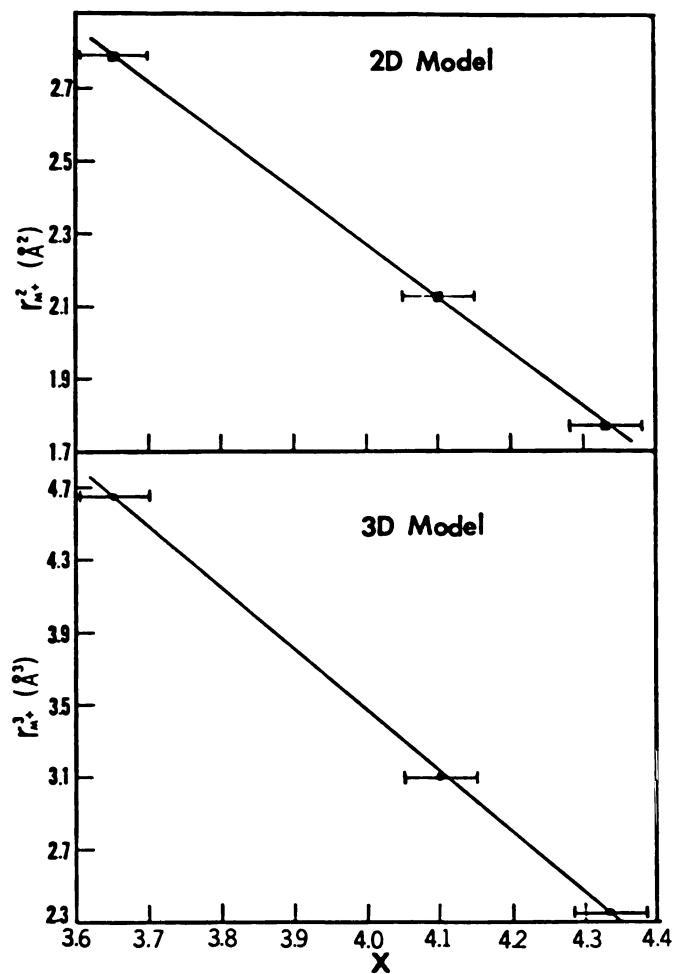


Fig. 2. Least-squares fits (solid lines) of the data of Table 1 to Eq. (4) (3D model, lower panel) and to Eq. 6 (2D model, upper panel) of the text.

where A_1 , A_{M+} , and A_{molecule} are the areas available for all intercalants, the metal ion and the molecule, respectively. Then

$$\alpha_{2D}^{(24+\Delta)} \frac{a^2\sqrt{3}}{4} = \pi r_{M+}^2 + x(\pi r_A^2) \quad (6)$$

where α_{2D} is the 2D packing fraction. With the assumption that $\langle \Delta \rangle = 0$, Eq. (6) predicts a linear variation of x with r_{M+}^2 (see Table 1 for values) and this variation is indeed observed as can be seen from the least-squares fit shown in

the upper panel of Fig. 2. Thus, the 2D and 3D models cannot be distinguished on the basis of linearity alone since their correlation coefficients are essentially the same [see Table 1]. However, both the ammonia radius and the packing fraction deduced from the 2D model are much too small and are well outside the range of experimental uncertainty. Therefore, the 3D model is the most appropriate.

CONCLUDING REMARKS

The simple "volume available" Setton approach to the determination of the composition of ternary GICs works extremely well for variations of both the molecular and metal ion species provided that a packing fraction is introduced to calculate the volume occupied by intercalant species. Moreover, the size of the metal ion has a noticeable effect on the amount of a given molecule which can be cointercalated into an alkali binary GIC. Finally, the composition of alkali-ammonia ternary GICs is dominated by the above described ion-size/volume effects and not by the tendency to form $M-(NH_3)_n$ -fold clusters, e.g. $K(NH_3)_4$.^{4,6} If cluster formation dominated the composition, the larger the ion, the larger would be the corresponding x value in contrast to observation.

ACKNOWLEDGMENTS

We are grateful to B.R. York, S.D. Mahanti, H.R. Resing, and R. Fronko for useful discussions. This work was supported by the U.S. National Science Foundation under grant DMR-82-11554.

REFERENCES

- 1 W. Rudorff and E. Schultze, *Angew. Chem.* **66**, 305 (1954).
- 2 J.C. Thompson, *Electrons in Liquid Ammonia* (Clarendon Press, Oxford, 1976).
- 3 J. Jortner and N.R. Kester, editors, *Electrons in Fluids: The Nature of Metal-Ammonia Solutions* (Springer-Verlag, New York, 1973); J.C. Thompson, *Rev. Mod. Phys.* **40**, 704 (1968).
- 4 X.W. Qian, D.R. Stump, B.R. York, and S.A. Solin, *Phys. Rev. Lett.* **54**, 1271 (1985).
- 5 N.F. Mott and E.A. Davis, *Electronic Processes in Non-Crystalline Materials* (Clarendon Press, Oxford, 1971).
- 6 B.R. York and S.A. Solin, *Phys. Rev.*, in press; B.R. York, S.K. Hark, and S.A. Solin, *Solid State Comm.* **50**, 595 (1984).
- 7 S.A. Solin, *Adv. Chem. Phys.* **49**, 455 (1982); R. Clarke, J.N. Gray, H. Homma, and M.J. Winokur, *Phys. Rev. Lett.* **47**, 1407 (1981).
- 8 B.R. York and S.A. Solin, *Bull. Am. Phys. Soc.* **30**, 284 (1985).
- 9 H.A. Resing, B.R. York, S.A. Solin, and R.M. Fronko, Proc. of the 17th Carbon Conference, Louisville, 1985, in press.
- 10 R. Setton, F. Béguin, J. Jegondez, and C. Mazières, *Rev. Chim. Miner.* **19**, 360 (1982).
- 11 J.W. McBain and A.M. Baker, *J. Am. Chem. Soc.* **48**, 690 (1926).
- 12 R.D. Shannon, *Acta. Cryst.* **A32**, 751 (1976).
- 13 Y.B. Fan, S.A. Solin, R. Fronko, and H.R. Resing, to be published.

APPLICATION OF MICROSCOPIC PROBES TO THE STUDY OF GRAPHITE INTERCALATION
COMPOUNDS

D.M. HWANG

Bell Communications Research, Murray Hill, NJ 07974, (U.S.A.)

R. LEVI-SETTI, G. CROW, Y.L. WANG, N.W. PARKER* and R. MITTLEMEN

The Enrico Fermi Institute and Department of Physics,
The University of Chicago, Chicago, IL 60637, (U.S.A.)

X.W. QIAN and S.A. SOLIN

Department of Physics and Astronomy
Michigan State University, East Lansing, MI 48824, (U.S.A.)

ABSTRACT

Ion and electron microprobes with the highest spatial resolution available today were used to investigate the nature of graphite intercalation compounds with multiphase multidomain structures. Secondary ion maps of $^{35}\text{Cl}^-$ from freshly cleaved surfaces of SbCl_5 intercalated graphite were obtained using a scanning ion microprobe capable of 20 nm lateral resolution. The maps exhibit discrete features of nearly parallel lines and bead-like domains. The sample-dependent lines are attributed to the accumulation of SbCl_5 along the surface defects. The bead-like domains have a typical dimension ~ 200 nm and are interpreted as the Daumas-Hèrold domains one graphite monolayer underneath the surface. Specimens of ~ 50 nm thickness for analytical scanning transmission electron microscopic studies were cleaved from the same bulk materials. Lateral distribution of elements integrated through the specimen thickness was obtained using energy dispersive x-ray spectroscopy. It is found that Cl distributes uniformly, while Sb forms high concentration islands of typical dimension ~ 70 nm. Electron energy loss spectra indicate that the low energy plasmons are modulated by the island structure while the carbon core excitations are spatially invariant. We suggest that the islands consist of an $\text{SbCl}_3/\text{SbCl}_4^-$ -like material while the background consists of an $\text{SbCl}_5/\text{SbCl}_6^-$ -like material.

INTRODUCTION

Many graphite intercalation compounds are synthesized at elevated temperatures at which the in-plane structures are disordered. Any in-plane phase transition occurring during cooling would result in a multiphase multidomain structure owing to the constraint of maintaining a constant average in-plane density. The nature of the resulting heterogeneous compounds is difficult to characterize using traditional diffraction probes. In general, the observed diffraction patterns are superpositions of patterns from several coexisting phases and the domain sizes exceed the limitation of diffraction line-width analysis [1]. Microscopic probes, with the probe beam size smaller

*Present address: MicroBeam Inc., 1077 Business Center Dr., Newbury, CA 91320.

than the domain size, are indispensable tools for establishing the physics and chemistry of individual microdomains. The probe beam can be rastered across the sample while monitoring various induced signals for constructing two-dimensional images.

A scanning ion microprobe (SIM) can focus an ion beam to 20 nm in diameter [2]. Because of the shallow escape depth of the induced secondary electrons and secondary ions (~ 0.5 nm), only the top few surface layers are probed. The ion-induced secondary electron (ISE) images exhibit topographic and channeling contrast. The channeling contrast is raised by the preferred channeling directions of the primary ion beam in crystalline materials and reveals information about the crystalline orientation [3]. The secondary ions can be energy and mass filtered, yielding a secondary ion mass spectrometric (SIMS) map which represents the lateral distribution of the selected isotope on the sample surface.

An electron beam can be focused down to 0.3 nm in diameter. Various electron induced secondary particles are used for sample characterization, such as elastic scattered electrons for electron diffraction and dark field imaging, energy-loss electrons for electron energy loss spectroscopy (EELS), x-rays for x-ray emission spectroscopy (XES) including energy dispersive x-ray spectroscopy (EDS), and visible light for cathodoluminescence. Because of the deep penetration depth of the primary electrons and the long escape length of the secondary particles, high spatial resolution is achieved only by using electron transparent thin samples so that the multiple-scattering broadening of the primary electron beam is minimized. Therefore, the sample thickness should be less than the electron mean free path in the material which is in the order of 50 nm for 100 keV electrons. In scanning transmission electron microscopy (STEM), images with lateral resolution of 0.3 nm can be obtained. For structural determination (convergent beam electron diffraction) and chemical analysis (EDS and EELS), the resolution is also limited by the instrument stability and the electron beam is usually defocused to reduce possible electron beam induced damage. The information obtained with STEM is integrated through the sample thickness.

SbCl_5 intercalated graphite was chosen in this study for its stability in air and in vacuum, as well as for its vast variety of structural phase transitions reported in the literature [4-8]. Above -180 C, the in-plane structure is disordered. At room temperature, it consists of at least a disordered phase and an ordered phase. The ordered phase has been identified as $\sqrt{T} \times \sqrt{T}$ and/or $\sqrt{39} \times \sqrt{39}$ commensurate superlattices. There are several phase transitions observed below room temperature [4-8]. Evidence for the disproportionation of SbCl_5 into SbCl_3 , SbCl_4^- , and SbCl_6^- has been reported [9,10].

Recently, we have characterized the structural and chemical properties of stage-2 and stage-4 SbCl_5 intercalated graphite using ion and electron microprobes [11,12]. In this article, detailed morphology of the multiphase multidomain structures of SbCl_5 -graphite deduced from these observations is presented and its implications on the nature of graphite intercalation compounds are discussed.

EXPERIMENTAL

Stage-2 and stage-4 SbCl_5 intercalated graphite samples were synthesized by the conventional two-temperature technique with a very slow intercalation rate [8] from highly oriented pyrolytic graphite (HOPG). For SIM studies, the samples were cleaved to expose fresh surfaces before inserting into the SIM chamber which was then evacuated to 10^{-6} Torr within 30 minutes, later to 10^{-9} Torr. STEM samples were prepared by repeated cleaving with adhesive tape and then mounted on copper or titanium supporting grids.

The high resolution SIM used in this study was developed jointly by the University of Chicago and Hughes Research Laboratories [2]. This instrument can focus a 40 keV beam of Ga^+ ions from a liquid metal source to a spot of 20 nm in diameter. Secondary electrons and ions are collected for imaging of surface topographic, crystallographic, and chemical contrast. A high transmission secondary ion energy analyzer and transport system, coupled to an RF quadrupole mass filter, is used to perform SIMS. An ion current of 1.5 pA was used for high resolution SIMS imaging and approximately half a graphite monolayer was sputtered away in taking each elemental map [12].

Analytical STEM studies were performed with a Vacuum Generators Model HB501 100 keV dedicated STEM equipped with a field-emission tip, an energy-dispersive x-ray detector, and an electron energy loss spectrometer of 0.5 eV resolution. Bright and dark field images were recorded with 0.3 nm resolution. An electron beam of ~5 nm diameter was used for EDS and EELS analysis.

RESULTS AND DISCUSSION

A typical $^{35}\text{Cl}^-$ SIMS map of stage-4 SbCl_5 intercalated graphite is shown in Fig. 1. The map indicates that the distribution of chlorine (and presumably intercalant) is highly discrete. The chlorine concentration in the bead-like domains and the sample-dependent lines is ~10 times that of the background. The bead-like domains distribute randomly and occupy ~25% of the total area, except that the bead density is usually depleted on one side of the lines. Stage-2 SbCl_5 -graphite yields similar SIMS maps except for a higher bead and line density and a lower peak to background ratio (~3).

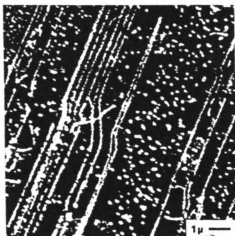


Fig. 1. $^{35}\text{Cl}^-$ secondary ion mass spectrometric map of a freshly cleaved surface of stage-4 SbCl_5 -graphite. The lines and bead-like domains have a Cl concentration ~ 10 times that of the background.

Sequential SIMS mapping of the same SbCl_5 -graphite surface indicates the loss of intercalant as expected since the sputtering yield of Cl compounds is much higher than that of graphite. We also noticed that the line pattern diminishes before the bead-like domains do [12], indicating that the bead-like domains are underneath the line pattern. Therefore, we suggest that the beads represent the Daumas-Hérol domains [13] one graphite monolayer underneath the surface and the lines represent the accumulation of SbCl_5 on surface steps as illustrated in Fig. 2. Near a surface step, the beads can diffuse toward the step and coalesce eventually into solid lines.



Fig. 2. An elaborated version of the Daumas-Hérol domain model which allows for the random nature of the domain size and lateral distribution. It also shows the depletion of the intercalant near a surface step.

A STEM dark field image of a stage-4 SbCl_5 -graphite thin flake is shown in Fig. 3, exhibiting high density islands of typical dimension ~ 70 nm. Two-dimensional EDS imaging indicates that the Cl distribution is uniform over the probed area and the high density islands are due to the high concentration of Sb. Quantitative analysis yields an Sb:Cl ratio of 0.32 ± 0.03 for the islands and of 0.14 ± 0.04 for the background regions [11]. EELS studies reveal that the low energy plasmons are modulated by the island structure while the carbon core

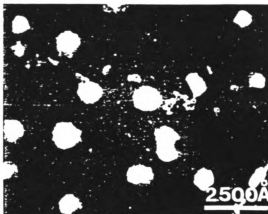


Fig. 3. Dark field scanning transmission electron microscopic image of a stage-4 SbCl_3 -graphite thin flake. It is found that Cl distributes uniformly while Sb has twice the concentration in the islands than in the background.

excitations are spatially invariant [11]. The latter indicates that both the island and background regions have the same degree of Fermi level downshift with respect to the graphite bands, and therefore, have the same degree of charge transfer. We thus suggest that the island consists of $(\text{SbCl}_3)_4(\text{SbCl}_4^-)$, while the background consists of $(\text{SbCl}_5)_2(\text{SbCl}_6^-)$, both having one negative charge per 16 Cl atoms.

Transmission electron diffraction indicates that the dominant phase of our stage-4 sample is of $\sqrt{7} \times \sqrt{7}$ structure, consistent with other studies [4-7]. Convergent beam electron diffraction from individual islands exhibits diffuse rings [14], indicating that the islands are of amorphous structure and the in-plane structure is correlated along the c-axis. It has been reported that the ordered phase can be converted into a glassy state by electron bombardment at low temperatures [7]. Since the glassy state changes back to the ordered phase at room temperature, that phenomenon is not related to the chemical and structural segregation observed in our studies.

Note that Fig. 1 is the Cl distribution on the sample surface while Fig. 3 is the through-thickness mass projection. The uniform through-thickness Cl distribution deduced from STEM EDS analysis is consistent with the model shown in Fig. 2. The typical bead dimension observed in Fig. 1 is ~ 200 nm which is comparable to the typical island separation observed in Fig. 3. This fact suggests that the chemical segregation of $\text{SbCl}_3/\text{SbCl}_4$ and $\text{SbCl}_5/\text{SbCl}_6$ is limited to within individual Daumas-Hérold domains, i.e., each Daumas-Hérold domain has an Sb-rich core of $\text{SbCl}_3/\text{SbCl}_4^-$ which is spatially aligned along the c-axis through the sample thickness of ~ 50 nm.

ACKNOWLEDGMENTS

We would like to thank S. A. Schwarz of Bell Communications Research for useful discussions and A. W. Moore of Union Carbide for providing the HOPG material. The work done at the University of Chicago is supported by the National Science Foundation under Grant No. DMR-8007978 and the Materials Research Laboratory at the University of Chicago. The work done at Michigan State University is supported by the National Science Foundation under Grant No. DMR83-11554 and by Michigan State University through its internally funded Analytical Electron Microscope Laboratory.

REFERENCES

- 1 S. A. Solin, Adv. Chem. Phys. **49**, 455 (1982).
- 2 R. Levi-Setti, Y. L. Wang, and G. Crow, J. Physique **45**, C9 (1984).
- 3 R. Levi-Setti, T. R. Fox, and K. Lam, Nucl. Instrum. Methods **205**, 299 (1983).
- 4 G. Timp, M. S. Dresselhaus, L. Salamanca-Riba, E. Erbil, L. W. Hobbs, G. Dresselhaus, P. C. Eklund, and Y. Iye, Phys. Rev. **B26**, 2323 (1982).
- 5 R. Clarke, M. Elzinga, J. N. Gray, H. Homma, D. T. Morelli, M. J. Winokur, and C. Uher, Phys. Rev. **B26**, 3312 and 5250 (1982).
- 6 R. Clarke, in Graphite Intercalation Compounds, ed. P. C. Eklund, M. S. Dresselhaus, and G. Dresselhaus (Materials Research Society, Pittsburgh, 1984), p. 152.
- 7 G. Roth, L. Salamanca-Riba, A. R. Kortan, G. Dresselhaus, and R. J. Birgeneau, in Graphite Intercalation Compounds, ed. P. C. Eklund, M. S. Dresselhaus, and G. Dresselhaus (Materials Research Society, Pittsburgh, 1984), p. 158.
- 8 D. M. Hwang and G. Nicolaides, Solid State Commun. **49**, 483 (1984).
- 9 P. Boolchand, W. J. Bresser, D. McDaniel, K. Sisson, V. Yeh, and P. C. Eklund, Solid State Commun. **40**, 1049 (1981).
- 10 L. B. Ebert, D. R. Mills, and J. C. Scanlon, Mater. Res. Bull. **18**, 1505 (1983).
- 11 D. M. Hwang, X. W. Qian, and S. A. Solin, Phys. Rev. Lett. **53**, 1473 (1984).
- 12 R. Levi-Setti, G. Crow, Y. L. Wang, N. W. Parker, R. Mittlemen, and D. M. Hwang, to be published.
- 13 N. Daumas and A. Hérol, C. R. Acad. Sci. **C268**, 373 (1969).
- 14 D. M. Hwang and J. Cowley, to be published.

MEASUREMENT OF THE MICROSCOPIC DISTRIBUTION OF BR
IN THE BROMINATED PITCH BASED GRAPHITE FIBERS

X.W. QIAN†, S.A. SOLIN*, and J.R. GAIER**

*Department of Physics and Astronomy, Michigan State University, East Lansing,
MI 48824-1116

**NASA Lewis Research Center, 21000 Brook Park Road, Cleveland, OH 44135

Brominated pitch based graphite fibers have been shown to have enhanced conductivity over that of pristine pitch-based fibers [1]. Two phases of the brominated fibers corresponding to different compositions exist, i.e. the saturated fibers and the residual fibers with the composition of $C_{2.2}Br$ and $C_{1.3}Br$, respectively. While the saturated fibers have a maximal reduction in the resistivity relative to that of the pristine material (-18 times) [1], saturation can only be maintained by constant contact with Br vapor. In contrast, the residual fibers made by removing the saturated fiber from the external Br bath are stable in air and even in vacuum [2], but they exhibit a smaller resistivity decrease relative to pristine fibers (-6 times) than do the saturated fibers [1]. To understand these resistivity reductions we have studied the microscopic Br distribution in the fiber compounds and related that distribution to the macroscopic resistance [3]. In this brief report we focus on the stable residual fibers.

A field emission scanning transmission electron microscope (FESTEM) equipped with an X-ray energy dispersive spectrometer (EDX) detector was used to establish the Br distribution. The fiber under examination was illuminated by a well-focused 100 KeV electron beam (beam diameter $\sim 50\text{\AA}$) in such a way that the direction of the beam was perpendicular to the longitudinal axis of the fiber. The electrons in the beam excited Br atoms along their pathway through the fiber. The Br K X-ray emission which resulted from inner shell excitation of the Br atoms^a by the energetic electrons was then collected by the EDX detector. When the electron beam was digitally controlled to scan across or along the axis of the fiber, the cross-sectional or longitudinal X-ray intensity profile could be recorded. Of course, the deduction of the real Br distribution from the observed X-ray intensity profile critically depends on the distribution of incident electrons in the fiber. We determined this distribution by a computer simulation.

A Monte Carlo simulation [3] shows that, as the electrons penetrate a material with an average composition corresponding to that of the residual fiber (density 2.2 gm/cm^3), they are effectively confined to a conical region under the impinging point as shown in the inset of Fig. 1. Statistically, as a result of the multiple scattering process, the energy of the incident electrons varies linearly with the penetration depth within a range corresponding to the diameter of our fibers, and the beam radius defined by the circular cross section of the cone that contains 90% of the incident electrons varies with the penetration depth according to a power law with an exponent of 1.5 [4]. At the penetration depth equivalent to the diameter of the fiber ($\sim 10\ \mu\text{m}$), the electron energy is reduced to 94 KeV and the beam cross section has increased to $2\ \mu\text{m}$ in radius. With the pathway of the incident electrons inside the fiber known, we can calculate the cross-sectional X-ray intensity profile for any assumed Br distributions [3]. When the calculated intensity profiles are compared with the experimental results, the Br distribution of the fiber can therefore be deduced.

Experimentally, two distinct cross-sectional X-ray intensity profiles were measured as indicated in Fig. 1 by dots (•) and crosses (+) which are associated, respectively with Br-rich and Br-poor regions of the fiber. The rounded profile of the Br-rich regions was observed from the vast majority of cross-sectional areas sampled and is characterized by intense emission at its peak. In contrast, the Gaussian-like profile of the Br-poor regions was observed from very few cross-sectional measurements and always exhibited a

peak intensity considerably smaller than that of the Br-rich region. In addition, in the Br-poor regions a Br-free surface depletion layer of typical thickness $1\mu\text{m}$ could be detected.

It can be shown [3] using the above cited Monte Carlo computer simulation that for the configuration and parameters defined in Fig. 2 the X-ray intensity profile $I(x)$ is given by

$$I(x) = \text{const.} \cdot \iiint \frac{\rho_{\text{Br}}[r(x)] \ln\left[\frac{E(z)}{E_c}\right]}{E(z)[b(z)]^2} (ds)(dz) \quad (1)$$

where ds is a cross-sectional area increment, $\rho_{\text{Br}}(x)$ is the bromine density distribution, $E(z)$ is the electron energy at a penetration depth z , $b(z)$ is the beam cross-sectional radius and E_c is the critical excitation energy for the inner shell X-ray emission line.

If we assume a uniform Br distribution $\rho_{\text{Br}}(r) = \text{const.}$, in Eq. (1), we obtain the excellent scaled fit to the X-ray intensity profile of the Br-rich region shown as a broken line (— — —) in Fig. 1. But a uniform distribution gives a very poor fit to the profile of the Br-poor region as can be seen from the dashed line (-----) in Fig. 1. However, if we assume a Gaussian distribution $\rho_{\text{Br}}(r) = \exp[-r^2/(0.45 a^2)]$ for the Br-poor region we obtain the very good fit shown as a solid line (————) in Fig. 1. The discrepancies in the wings of the Gaussian fit are due to the surface depletion layer.

ACKNOWLEDGEMENTS

We thank D.M. Hwang and D.A. Jorowski for useful discussions. This work is supported by NASA under grant #NAG-3-595.

†Exxon Fellow

REFERENCES

1. J.R. Gaier, NASA TM-87275. 1986.
2. J.R. Gaier, NASA TM-86859, 1984.
3. X.W. Qian, S.A. Solin, and J.R. Gaier, Phys. Rev., submitted.
4. J.I. Goldstein in Introduction to Analytic Electron Microscopy, edited by J.J. Hern, J.I. Goldstein and D.C. Joy (Plenum Press, New York and London, 1979).

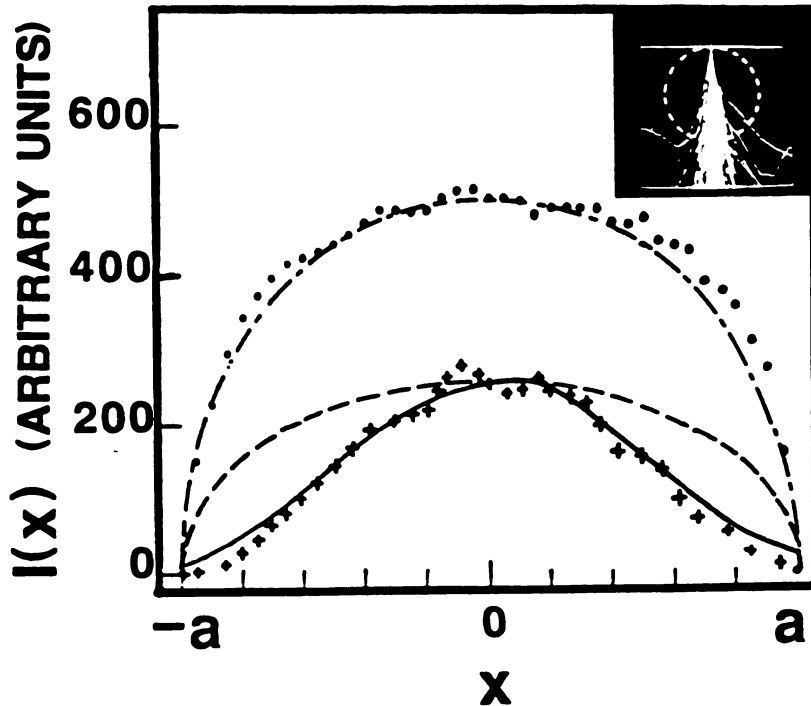


Fig. 1. Plots of the Br K X-ray intensity vs. the lateral position (x) of the incident electron beam. The dots (\cdot) denote the experimental data for the Br-rich region, and the broken line (— — —) was calculated from Eq. (1) using a radially uniform Br distribution. The crosses ($+$) represent the experimental data points in the Br-poor region, and the solid line (—) [dashed line (-----)] was calculated from Eq. (1) using a Gaussian (uniform) Br distribution. The inset shows an output of the computer simulated paths of 100 keV incident electrons through a 15 μm thick slab of brominated fiber. The dashed circle represents the cross section of the fiber.

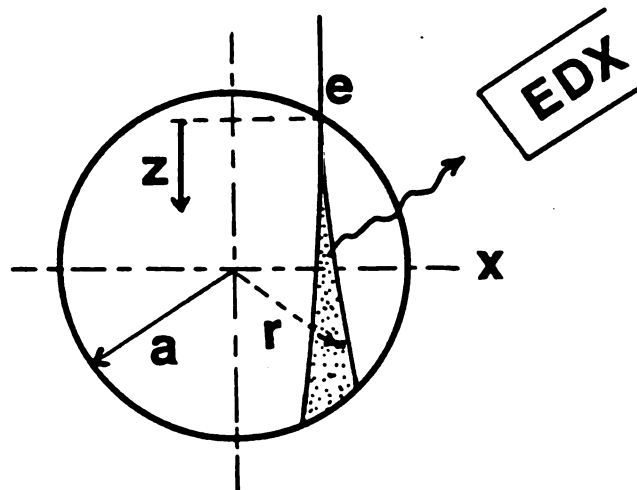


Fig. 2. A geometric designation of the parameters and variables used in Eq. (1) of the text.

EVIDENCE FOR A 2-DIMENSIONAL METAL-INSULATOR TRANSITION IN POTASSIUM-
AMMONIA GRAPHITE

Y.Y. Huang, X.W. Qian*, and S.A. Solin

Department of Physics and Astronomy
Michigan State University
East Lansing, MI 48824-1116

J. Heremans and G.G. Tibbets

Physics Department
General Motors Corporation
Warren, MI 48090-9055

We have studied the ammonia pressure dependence and composition dependence of the a-axis electrical resistivity of the potassium-ammonia ternary graphite intercalation compounds $K(NH_3)_x C_{24}$, $0 < x < 4.33$. Our results show evidence of the 2D analog of the well-studied bulk 3D metal-insulator transition [1] in bulk K-NH₃ solutions.

In order to probe the electrical properties of the intercalate layer in $K(NH_3)_x C_{24}$, we measured the in-plane a-axis resistivity as a function of ammonia pressure [2]. For convenience, we used a benzene-derived onion skin-like graphite fiber [3] rather than HOPG. Thus, the fiber axis is approximately coaxial with the cylindrical graphite planes. From the (001) x-ray diffraction patterns of a single fiber (see Fig. 1) we determined the basal spacing of the pristine fiber ($d_a = 3.35\text{\AA}$), of stage-2 KC_{24} , potassium binary GIC ($d_b = 8.74\text{\AA}$) and of the stage-1 ternary GIC $K(NH_3)_{4.33} C_{24}$ ($d_c = 6.64\text{\AA}$). These results indicate that the graphite fiber has the same Gibbs phase diagram [4] as HOPG.

A four-probe measurement technique was developed for monitoring the pressure dependence of the a-axis relative resistance (R/R_0) of $K(NH_3)_x C_{24}$, using a pressure up-quenching technique. [Here $R(R_0)$ is the a-axis resistance of the ammoniated (KC_{24}) compound.] The result is plotted in Fig. 2. Note that the relative resistance ratio remains a constant below one atmosphere and then starts to increase in the stage-2 to stage-1 phase transition region at ≈ 0.5 atm. [5]. The increasing resistivity in a stage-2 to stage-1 phase transition is a common feature of binary GIC's [5]. But when NH_3 is added to KC_{24} , some delocalized electrons in the carbon layer are back-transferred to the intercalate layer [6] so that the conductivity of the carbon layers decreases. However, R/R_0 starts to decrease dramatically at about 3-4 atm. at which pressure x is greater than four [6]. This phenomenon may be a consequence of a 2D metal-insulator transition. When $x = 4$, there are enough NH_3 molecules to completely solvate potassium and form a 4-fold coordinated K-NH₃ clusters [7]. Higher NH_3 concentration leads to a sufficient amount of electron back-transfer

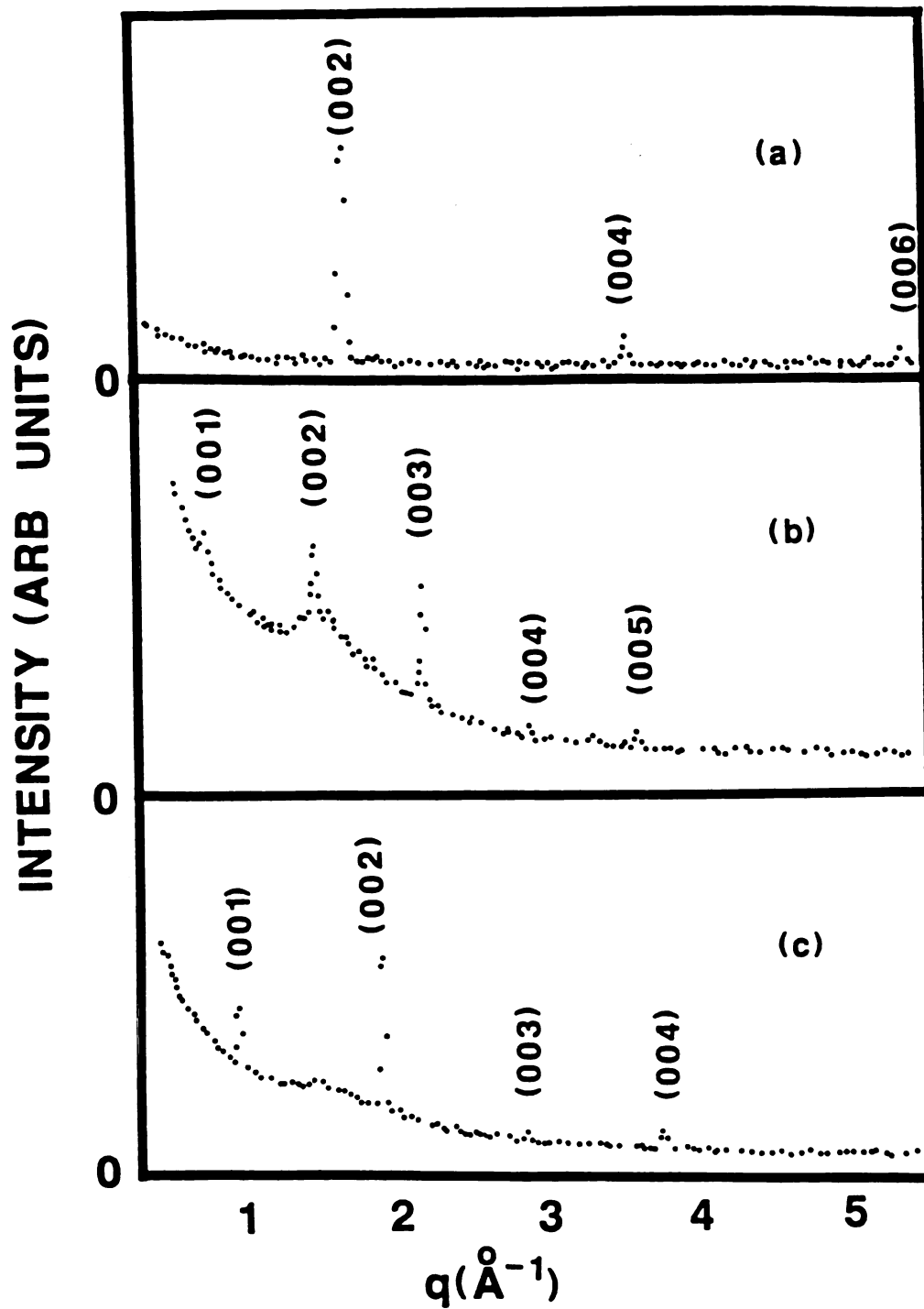


Fig. 1. The (00l) x-ray diffraction patterns of (a) a single pristine cylindrical onion skin-like graphite fiber, (b) the same fiber as in (a) after intercalation with potassium to form the binary GIC KC_{24} , and (c) the same fiber as in (b) after ammoniation to form the ternary GIC $K(NH_4)_3C_{24}$. The diffraction patterns were recorded at room temperature using $MoK\alpha$ radiation. The background continuum is diffuse scattering from the glass envelope and from air in the beam path.

A FIELD EMISSION STEM STUDY OF THE Br DISTRIBUTION IN BROMINATED GRAPHITE
FIBERS

X.W. Qian* and S.A. Solin

Department of Physics and Astronomy
Michigan State University
East Lansing, Michigan 48824-1116

J.R. Gaier

NASA Lewis Research Center
21000 Brook Park Road
Cleveland, OH 44135

Brominated pitch based graphite fibers exhibit certain novel properties and potential applications [1,2]. For example, it has been observed that an 18 fold reduction of their resistivities of the pitch-based graphite fibers can be achieved if the pristine fibers are allowed to fully interact with bromine [3] and even the residual fiber compounds that are formed by pumping off the bromine from the fully brominated fibers (saturated fibers), exhibit a five-fold reduction in the resistivities relative to that of the pristine fibers [3]. To understand this property, it is essential to know the Br distribution in such fiber compounds. Here we focus on the residual fibers that have a density of 2.2 gm/cm^3 corresponding to a composition of $\text{BrC}_{1.1}$.

A FSTEM (Field Emission Scanning Transmission Electron Microscope) was used to study the Br distribution in the residual form of the fiber. The fiber under examination was bombarded by a well focused 100 KeV electron beam (beam diameter $\sim 50\text{\AA}$) in such way that the direction of the beam was perpendicular to the longitudinal axis of the fiber. The high energy electrons penetrate into the material, excite the Br atoms in their pathway which in turn give off the characteristic K X-rays. A EDX (Energy Dispersive X-ray) detector collects the X-rays. When the electron beam is digitally controlled to scan across the fiber or along the longitudinal axis of the fiber, the cross-sectional or longitudinal X-ray intensity profile can be recorded. These X-ray intensity profiles together with a knowledge of the electron path inside the fiber enabled us to deduce the Br distributions in the fiber.

The details of the incident electron path are established by computer simulation. As the electrons penetrate into the material, they strongly interact with the atoms in the material. They lose energy and are scattered away from the original direction. Consequently, the electron beam diameter and the energy vary with the penetration depth [4]. A Monte Carlo simulation [5] shows that over the range of fiber size ($\sim 10 \mu\text{m}$), the beam diameter is related to the depth through a power law with an exponent



Fig. 1. The Br K X-ray intensity variation (curved line of dots) along a PB fiber superposed on the bright field image of the fiber the axis of which is perpendicular to the incident electron beam. The straight dotted line denotes the position of the electron beam as it is digitally scanned along the longitudinal axis of the fiber.

of 1.5, and the energy of the electrons varies linearly with depth with a rate $-0.6 \text{ KeV}/\mu\text{m}$. At $10 \mu\text{m}$ depth the beam is broadened to $3 \mu\text{m}$ and the energy is reduced to 94 KeV . Once the electron paths and energies inside the fiber are known, the X-ray intensity profile generated from an assumed bromine distribution can be calculated directly. By comparing the calculated profile to the experimental profile we can deduce the Br distribution in the fiber.

Experimentally we find an inhomogeneous Br distribution along the longitudinal axis of the fiber (see Fig. 1) with two distinct cross-sectional distributions, i.e. a uniform distribution in the Br-rich region and a Gaussian distribution in the Br-poor region (See fig. 2). It is worth noting that a depletion layer of $-1 \mu\text{m}$ is found on the surface of the Br-poor regions. This is attributed to the porous like structure of the fiber near the surface.

ACKNOWLEDGEMENTS

We thank D.M. Hwang, J.R. Gaier, and D.A. Joworski for their useful discussions. This work is supported by the National Aeronautics and Space Administration under grant NAG-3-595.

*Exxon Fellow

REFERENCES

1. J.G. Hooley and V.R. Diets, Carbon 16, 251(1978)
2. J.R. Gaier and D. Marino, NASA TM-87016, 1985.

3. J.R. Gaier, NASA TM-87275, 1986.
4. J.I. Goldstein in Introduction to Analytical Electron Microscopy, edited by J.J. Hern, J.I. Goldstein and D.C. Joy (Plenum Press, New York and London, 1979).
5. X.W. Qian, S.A. Solin, and J.R. Gaier, Phys. Rev., submitted.

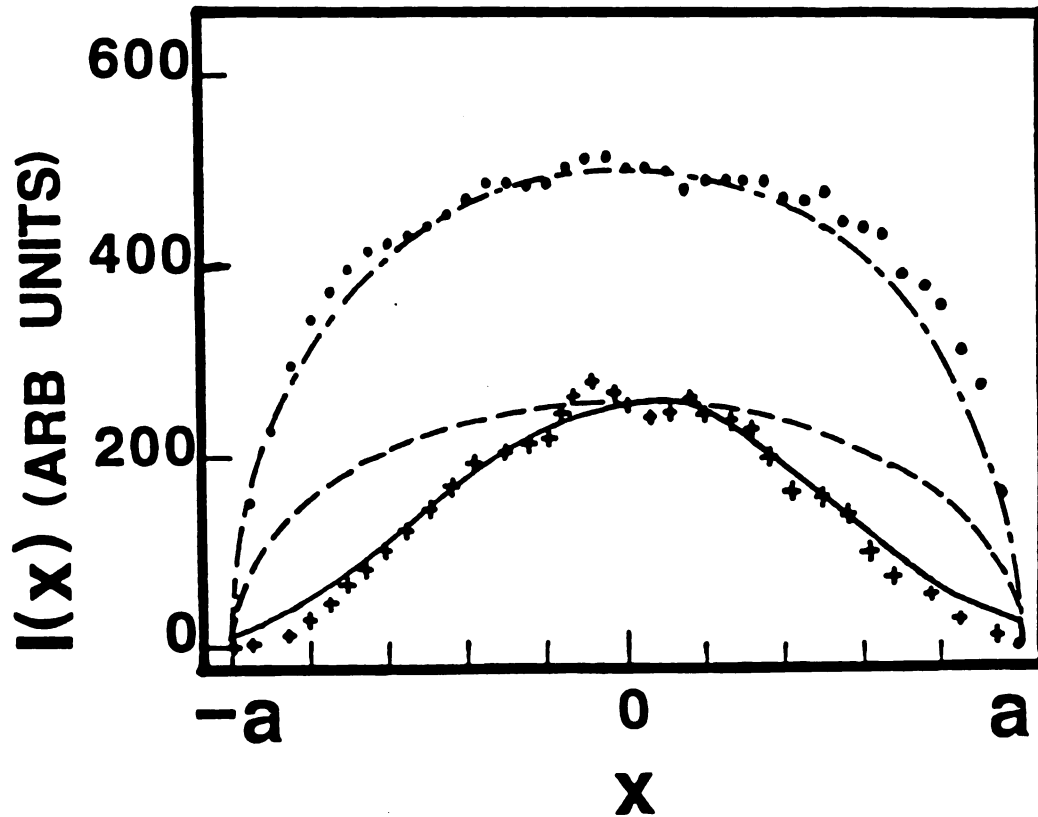


Fig. 2. A plot of Br K X-ray intensity vs. the lateral position (x) of the incident electron beam. The dots (\cdot) denote the experimental data for the Br-rich region, and the dashed line is the calculated intensity from a radially uniform Br distribution. The crosses ($+$) represent the experimental data points in the Br-poor region, and the solid line is the calculated intensity from a Gaussian Br distribution, $\rho_{\text{Br}}(r) = \rho_0 e^{-\frac{r^2}{0.45a^2}}$, where a is the radius of the fiber and r is the distance from the axis of the fiber. A scaled intensity calculated from a uniform Br-distribution in the Br-poor region is also shown as a broken line.

ANALYTICAL ELECTRON MICROSCOPIC STUDY OF MICRODOMAIN STRUCTURES IN ANTIMONY
PENTACHLORIDE INTERCALATED GRAPHITE

D.M. HWANG,* X.W. QIAN,** AND S.A. SOLIN**

*Bell Communications Research, Murray Hill, NJ; **Michigan State University,
East Lansing, MI.

It has been reported¹ that at room temperature $SbCl_4$ intercalated graphite exhibits multiphase multidomain inplane structures with Sb-rich islands in an Sb-deficient background. In this paper, we will show that the islands consist of $SbCl_4/SbCl_3$ -like material, while the background is $SbCl_4/SbCl_3$ -like. We report a unique molar ratio of $SbCl_4:SbCl_3:SbCl_2 = 4:1:18:9$ in stage-4 $SbCl_4$ -graphite.

Bulk stage-4 $SbCl_4$ -graphite was prepared from HOPG by the standard two-bulb technique and then x-ray characterized. Transmission electron microscopic specimens were cleaved from the bulk, thinned with adhesive tape, and mounted on copper supporting grids. A Vacuum Generators Model HB501 analytical scanning transmission electron microscope equipped with a field emission tip was used to obtain the bright field and dark field images, the energy dispersive x-ray spectra, and electron energy loss spectra.

Typical bright and dark field images obtained from stage-4 $SbCl_4$ -graphite thin flakes of thickness $\sim 500\text{\AA}$ are shown in Figs. 1 and 2, respectively. Both reveal the existence of high density islands. Similar multi-domain images have also been observed on the fresh surface of bulk stage-2 $SbCl_4$ -graphite with a scanning ion microscope.²



Fig. 1. Bright field micro-image of stage-4 $SbCl_4$ -graphite.

Typical energy dispersive x-ray spectra from island and background regions obtained with an electron beam size of $\sim 50\text{\AA}$ are shown in Fig. 3. Following standard x-ray microanalysis procedures,³ the chemical composition in the island region is found to be $SbCl_{3.1 \pm 0.3}$, while the background region has a composition of $SbCl_{7.0 \pm 2.0}$. By monitoring the x-ray intensity of the Cl K-line and the Sb L-line signals as a function of probe position on the specimen while scanning the electron beam in one or two dimensions, it is found that Cl atoms are distributed uniformly throughout the imaged area, while the Sb concentration is almost doubled in the island region compared to that in the background region.

The high contrast of the multidomain images and the distinct Sb:Cl ratio in the island and background regions suggest that the inplane domain structures are strongly correlated along the c-axis, i.e. the high density domains in each intercalant layer stack directly on top of each other over the specimen thickness of ~500Å. A preliminary electron microdiffraction study⁶ confirms this conclusion. In addition to the graphite diffraction pattern, the islands give amorphous halos, while the background gives extra spots some of which could be indexed to the $(\sqrt{7} \times \sqrt{7})R19.1^\circ$ superlattice.⁶

It has been proposed⁵ that upon intercalation into graphite, $SbCl_3$ disproportionates into $SbCl_2$ and $SbCl_4^-$, and the latter species is responsible for the charge transfer. Our observation suggests that the Sb^{3+} and Sb^{2+} species are spatially segregated.

If $SbCl_3$, $SbCl_2$, and $SbCl_4^-$ are the only molecular species present, then the island region should contain only $SbCl_3$, which is electrically neutral. Consequently, the graphite layers adjacent to the island region should be neutral, while those adjacent to the background region, would be positively charged. This point is checked using electron energy loss spectroscopy.¹ Although the graphite 6eV π -plasmon peak shows significant differences between the island and background regions, the carbon 1s core excitation edge indicates the same shift of the Fermi level relative to the valence band. Therefore, the charge in the graphite layers must be delocalized as must the charge in the intercalant layers.

We propose that the islands consist of $SbCl_3/SbCl_4^-$ complexes, while the background consists of $SbCl_2/SbCl_4^-$ complexes. Ebert, et al.⁵ have proposed that $SbCl_4^-$ is also a disproportionation product of $SbCl_3$ when it is intercalated into graphite. Given the conditions that (1) The average chemical composition is $SbCl_2$; (2) The charge is completely delocalized; (3) The Cl atoms are uniformly distributed; and (4) The island region occupies 11% of the total area; we derived the unique chemical formula of $(SbCl_3)_{1/8} (SbCl_4^-)_{1/32} (SbCl_2)_{9/16} (SbCl_4^-)_{9/32}$.

ACKNOWLEDGEMENTS

We would like to thank A.W. Moore for providing pyrolytic graphite and V. Shull for technical assistance. We are grateful to J. Fischer, P. Eklund, J. Cowley, and R. Levi-Setti for stimulating discussions. This research has been supported by the NSF under grant DMR83-11554, by Michigan State University through its internally-funded Analytical Electron Microscope Laboratory, and by the Research Board of the University of Illinois at Chicago.

REFERENCES

1. D.M. Hwang and S.A. Solin, Bull. Am. Soc. 29, 293 (1984), and to be published.
2. W. Parker, R. Levi-Setti, and D.M. Hwang, to be published.
3. Introduction to Analytical Electron Microscopy, ed. by Hren, Goldstein, and Joy (Plenum, New York, 1979).
4. D.M. Hwang and J. Cowley, unpublished.
5. L.B. Ebert, D.R. Mills, and J.C. Scanlon, Mat. Res. Bull. 18, 1505 (1983).

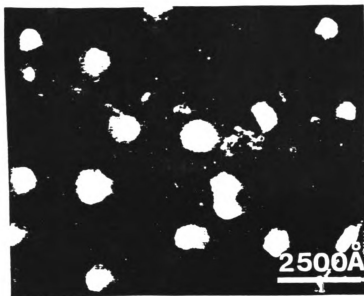


Fig. 2. Dark field micro-image of stage-4 SbCl_3 , graphite.

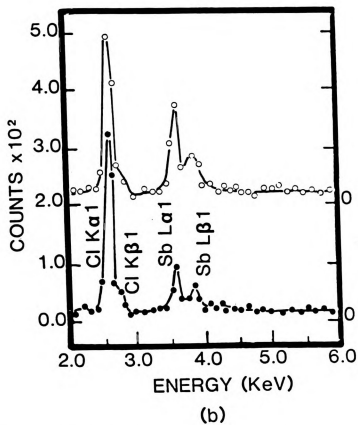


Fig. 3. Energy dispersive x-ray spectra from island (o) and background (•) regions in stage-4 SbCl_3 -graphite.

^1H NMR Study of NH_3 Orientation and Diffusion in
Ternary Ammonia Alkali Metal-Graphite Intercalation Compounds

R. M. Fronko and H. A. Resing
Code 6120
Naval Research Laboratory
Washington, D. C. 20375-5000

T. Tsang
Department of Physics and Astronomy
Howard University
Washington, D. C. 20059
and Code 6120
Naval Research Laboratory
Washington, D. C. 20375-5000

X. W. Qian* and S. A. Solin
Department of Physics and Astronomy
Michigan State University
East Lansing, Michigan 48824-1116

*Exxon Fellow

ABSTRACT

For the first stage ternary graphite compounds (TGIC) $K(NH_3)_{4.3}C_{24}$, $Rb(NH_3)_{4.1}C_{24}$ and $Cs(NH_3)_{3.7}C_{24}$ derived from highly oriented pyrolytic graphite, the 1H NMR spectra have been studied at various temperatures and orientations. The spectra consist of three sets of triplet resonance lines due to the $^1H-^1H$ and $^1H-^{14}N$ dipolar interactions. The simple spectral features and narrow spectral lines indicate fast diffusion and reorientations of NH_3 molecules in the graphite gallery. The C_3 -axes of NH_3 molecules are oriented nearly perpendicular to the crystallographic c-axis of the TGIC. The molecules are situated near the bottoms of potential wells with barrier heights of ~ 0.2 eV. The HNH bond angle of 107° is very close to the gas phase value. The indirectly measured ^{14}N quadrupolar coupling constant of 3.7 MHz is intermediate between the gas and solid NH_3 values of 4.1 and 3.2 MHz. The NMR results are consistent with a rather mobile and liquid-like layer of planar $M(NH_3)_4^+$ ions (where M denotes K, Rb or Cs) in between the carbon layers. These ions are the two-dimensional analogues of the $M(NH_3)_6^+$ ions commonly observed in alkali metal-ammonia solutions. There is relatively weak partial solvation of the electronic charge on the carbon layers by the co-intercalation of NH_3 .

I. INTRODUCTION

By various oxidation and reduction reactions, graphite intercalation compounds (GIC) may be formed from many different types of graphite, such as natural crystals, highly oriented pyrolytic graphite (HOPG), and graphite fibers.¹⁻³ A universal feature of these topotactic reactions is that monatomic or molecular ions open and enter the space between the carbon layers of the graphite crystal. The entry of the intercalant species is accompanied by the deposit of counter-charge on the carbon layers. The electrical charge deposited on the planar carbon layers are highly mobile and give the GIC's very high electrical conductivities, often highly anisotropic and comarable to the noble metals. The high strength to weight ratio of graphite fibers is only slightly diminished by the intercalation process. Because of these unusual characteristics, the GIC's have many potential applications in power transmission, batteries, chemical catalysis, etc.

In donor compounds, the carbon layers are reduced by intercalation with alkali metals (denoted as M) such as K, Rb and Cs or other metals. The alkali metal (M) atom donates its outer s-electron to the carbon layer and enters the gallery or interlayer space as a monatomic ion with single positive charge. The staging phenomenon is exhibited by all these compounds, where the intercalate layers are periodically arranged in a matrix of carbon layers. The GIC's are classified by a stage index, n , denoting the number of carbon layers between the adjacent intercalant layers. This number n is not an average, but indicates the real periodicity of the crystal along the c-axis of the GIC. Thus several different compounds may be formed. For instance, the GIC compositions MC_8 , MC_{24} and MC_{36} corresponds to $n=1,2$, and 3 .

In acceptor compounds, the carbon layers are oxidized by intercalation with highly reactive compounds such as Br_2 , H_2SO_4 , HNO_3 , AsF_5 , etc. There are mobile holes in the valence bands of the carbon layer due to the removal of the electrons. Staging phenomena are also exhibited by the acceptor GIC's. However, small fractional charge transfers are common for the acceptors and the stoichiometry is no longer a clear indicator of the chemistry that has taken place. For instance⁴, in $\text{C}_{8n}\text{AsF}_5$ where n is the stage index, there are 0.26 holes generated per AsF_5 for n=1 but 0.50 holes generated per AsF_5 for n=2. This implies variable ratios among the equilibrium concentration of the "intercalated" species which are believed to comprise AsF_6^- , AsF_5 and AsF_3 . Here, the latter two species play the part of neutral "spacers". Hence the chemistry of the acceptor GIC's appears to have more variability, which can be manipulated by sample preparation.

Neutral "spacers" such as tetrahydrofuran⁵ and benzene⁶ may co-intercalate the donor compounds as well. The ammonia molecules (NH_3) co-intercalate the alkali metal donor GIC's also.⁷⁻⁹ However, liquid ammonia itself is a solvent for alkali metals, where the metal atom gives its outer s-electron to be solvated by the liquid NH_3 . The fundamental questions for these ternary GIC's are: (a) what are the NH_3 molecular geometries, orientations and motions in the graphite galleries, and (b) whether the co-intercalated NH_3 molecules are only neutral "spacers" or compete with the carbon layers for the electrons given up by the alkali atoms.

In our present study, we have used ^1H nuclear magnetic resonance (NMR) spectroscopy of the co-intercalated NH_3 molecules to seek answers to the first question. We have studied the first stage ternary alkali metal ammonia GIC's, $\text{M}(\text{NH}_3)_x\text{C}_{24}$, where x is approxi-

mately equal to 4 for M=K, Rb and Cs. These ternary compositions are reached by the subsequent intercalations of the corresponding second-stage binary GIC's MC_{24} with gaseous NH_3 at room temperature and a pressure of 9.5 atmospheres. There has been considerable recent work on these ternary GIC's (TGIC)⁸⁻¹¹ since the existence of $M(NH_3)_x$ layers have been shown to be two-dimensional analogue of the alkali metal-ammonia solutions^{12,13} and are liquid-like in the graphite gallery. The binary GIC's MC_{24} are obtained by the intercalation of alkali metal vapors into HOPG. The c-axes of the individual crystallites of HOPG are well-aligned (within a spread of $\pm 2^\circ$) while there is considerable disorder in the ab-plane of the carbon layer. Once the TGIC is formed, the sample behaves much like a single crystal.

In our present work, the experimental details are described in Sec. II. Typical experimental 1H NMR spectra are given in Sec. III. The general features of these spectra are nine resonance lines forming a triplet of triplets. These features are somewhat more complicated than the three-line spectra observed by Miller et al.¹⁴ for AsF_3 co-intercalated into the graphite gallery. These spectra have been used to deduce the preferred orientations and the rapid motions (with correlation times shorter than 10^{-5} sec) of NH_3 molecules in the TGIC. These spectra have been interpreted in terms of the dipolar splittings due to the $^1H-^1H$ and $^1H-^{14}N$ interactions. We have found that the molecular geometry of NH_3 in the TGIC to be very similar to the geometry of NH_3 observed in the gas phase.¹⁵ We have also shown that the uneven spacing of the central triplet is due to the ^{14}N quadrupole moment. The temperature dependences of 1H NMR spectra are presented in Sec. IV. These temperature dependences have been used to infer that molecular C_3 -axes of NH_3 are nearly perpendicular

to the crystallographic c-axis of the TGIC. In Sec. V, the ^1H NMR results are compared with the previous X-ray and neutron scattering results.⁸⁻¹¹ The results are consistent with a simple liquid-like intercalant layer of $\text{M}(\text{NH}_3)_4$ ions in these TGIC's.

The compositions of the TGIC's are $\text{K}(\text{NH}_3)_{4.3}\text{C}_{24}$, $\text{Rb}(\text{NH}_3)_{4.1}\text{C}_{24}$ and $\text{Cs}(\text{NH}_3)_{3.7}\text{C}_{24}$. The experimental data for these TGIC's are quite similar to each other, hence only the results for the K-compound will be discussed in detail.

It has been proposed by us¹⁶ that the ^{13}C NMR spectra and chemical shift may be used to seek answers to the second question. The ^{13}C NMR chemical shift and charge transfer to the carbon layers of the TGIC will be presented in a separate paper.¹⁷

II. EXPERIMENTAL

The TGIC's have been prepared by the exposure of the second stage binary GIC MC_{24} (from the reaction of alkali metal vapors with HOPG) to the vapor from liquid ammonia at room temperature (9.5 atm. vapor pressure) for several hours.^{8,9} However, a large pool of excess liquid NH_3 would remain in the TGIC sample tube. The excess NH_3 is undesirable for many NMR experiments. By using the apparatus shown in Fig. 1, the problem of excess NH_3 was circumvented by sealing the GIC with sufficient NH_3 to give the required composition and an atmosphere of NH_3 at 9.5 atm. pressure external to the GIC. The GIC and liquid NH_3 are contained in separate chambers which may be isolated from each other by teflon stopcock T. The total volume of the specimen chamber is V. The final volume of the sealed GIC sample is V'. The binary GIC (MC_{24}) is exposed to the vapor from a pool of liquid NH_3 (from the vacuum line on the other side of the stopcock T', not shown

in Fig. 1) for a minimum of 5 hours to reach the fully loaded TGIC as confirmed by a X-ray diffraction pattern. We then calculate the amount of NH_3 required to fully load the TGIC and to maintain the 9.5 atm. pressure in the volume V' . After closing the stopcock T' , the reservoir A is cooled slowly (to prevent exfoliation of the TGIC) to a pre-determined temperature such that the calculated amount of NH_3 would be present in the TGIC sample and in the vapor phase of the volume V . After the pre-determined temperature is reached, stopcock T is closed and the specimen chamber is slowly cooled to liquid nitrogen temperature to condense all NH_3 into the sample chamber. The sample is then sealed off at the point S to give the volume V' . Upon warming to room temperature, the TGIC composition is confirmed by a X-ray diffraction pattern. The TGIC does not contain pool of excess liquid NH_3 . Only a slight and non-obscuring amount of NH_3 is adsorbed on the TGIC surface.

For the potassium compound $\text{K}(\text{NH}_3)_{4.3}\text{C}_{24}$ (KTGIC), the X-ray rocking curve is shown in Fig. 2 for the (002) reflection using $\text{MoK}\alpha_{1,2}$ radiation (0.71 Å wave length). The X-ray intensity is plotted vs. the angle \ominus between the X-ray beam and the GIC surface. There appears to be about $\pm 3^\circ$ misalignments of the various crystallites within the GIC.

The ^1H NMR spectra were obtained on a JEOL type FX60Q Fourier transform spectrometer operating at 59.75 MHz using 27 μs (90°) pulses. The TGIC approximates a single crystal and all NMR spectra will depend only on the angle α between TGIC crystallographic c-axis and the magnetic field. The orientation $\alpha = 0^\circ$ is determined by maximizing the satellite line splittings of the NMR spectra.

For low temperature spectra, the probe was cooled by passing nitrogen from a pressurized tank through a cooling coil immersed in

a dewar containing liquid nitrogen. The temperature at the probe was maintained and measured with a JEOL NMVT-3C temperature controller using a thermocouple fixed at the bottom of the sample in the probe.

III. ^1H NMR SPECTRA AND MOLECULAR MOTION

In Fig. 3, the room temperature spectra at 60 MHz and $\alpha=0^\circ$ are shown for the K, Rb and Cs compounds. These spectra are quite similar to each other. Because of this similarity, only the results of the K-compound (KTGIC) will be discussed in detail. In Fig. 4, the room temperature spectra of KTGIC at 60 MHz are shown for various angles of α between the magnetic field H_0 and the crystallographic c-axis of the KTGIC. The spectral lines at $\alpha=0^\circ$ are numbered as 1-9 from left to right (from higher frequency to lower frequency). The general spectral feature is three triplets. We will refer to them as the central triplet and the outer triplets. The spectral line positions ν_m ($m=1$ to 9) in KHz are plotted vs. α in Fig. 5. The splittings between the spectral lines m and n may be denoted as $\nu_{mn} = \nu_m - \nu_n$. The room temperature spectrum at 300 MHz is shown as Fig. 6 for $\alpha=90^\circ$. The splittings between the spectral lines are similar to the values obtained at 60 MHz for $\alpha=90^\circ$ as shown in Fig. 4.

These experimental spectra may be used to deduce the molecular orientations and motions of the intercalated NH_3 . We will now proceed to calculate the theoretical NMR spectra and then compare with the experimental spectra. For NH_3 molecules, it is necessary to consider three ^1H nuclear spins with $I_1=I_2=I_3=\frac{1}{2}$ (forming an equilateral triangle) and one ^{14}N spin with $S=1$. The complete spin Hamiltonian H is given by:¹⁸

$$H = \gamma_H H_0 \sum_i I_{iz} + \gamma_N H_0 S_z + \sum_{ij} A_{ij} (I_i \cdot I_j - 3I_{iz} I_{jz}) + \sum_i B_i (-2I_{iz} S_z) + H_Q \quad (1)$$

where H_0 is the magnetic field along the Z-axis, γ_H and γ_N are the ^1H and ^{14}N gyromagnetic ratios, and H_Q is the ^{14}N quadrupolar Hamiltonian. The first term is the proton Zeeman term with summation over $i = 1, 2, 3$. The second term is the ^{14}N Zeeman term. The third term is the ^1H - ^1H dipolar coupling where \sum_{ij} denotes summation over $ij = 12, 23, 31$. If H , H_0 and γ are expressed in units of Hz, Gauss, and Hz/Gauss respectively, then we have

$$A_{ij} = \gamma_H^2 h r_{ij}^{-3} (3 \cos^2 \psi_{ij} - 1) / 2 \quad (2)$$

for pairs of like spins, where r_{ij} is the ^1H - ^1H internuclear distance, h is Planck's constant and ψ_{ij} is the angle between the internuclear vector \underline{r}_{ij} and the magnetic field H_0 . The fourth term is the ^{14}N - ^1H dipolar coupling:

$$B_j = \gamma_H \gamma_N h r_{Nj}^{-3} (3 \cos^2 \psi_{Nj} - 1) / 2 \quad (3)$$

where r_{Nj} is the ^{14}N - ^1H internuclear distance and ψ_{Nj} is the angle between the internuclear vector \underline{r}_{Nj} and the magnetic field H_0 . The last term, H_Q , is the ^{14}N quadrupolar Hamiltonian.

If the relatively small ^{14}N nuclear magnetic moment and H_Q are temporarily omitted, then the NH_3 molecule may be regarded as three interacting spin $\frac{1}{2}$ nuclei at the vertices of an equilateral triangle. The theoretical NMR spectra of these triangles have originally been discussed by Andrew and Bersohn.¹⁹ This treatment has been generalized to a two-dimensional GIC lattice by Miller et al.¹⁴ with necessary modifications. In the GIC lattice, a spherical coordinate system may be used where the polar axis (the z-axis) is chosen to be the crystallographic c-axis of the GIC. The instantaneous orientation of the C_3 -axis of a particular NH_3 molecule may be denoted by the polar and azimuthal angles, θ and ϕ , in the spherical coordinate

system as shown in Fig. 7. For the entire GIC system with many NH_3 molecules intercalated into the graphite galleries, it is expected that θ will occupy only a relatively narrow range of angles because of the constraints of the gallery height. On the other hand, several angles of ϕ distributed evenly over the range 0 to 2π are accessible to an intercalated NH_3 molecule. If the NH_3 molecules are stationary, then there would be wide distributions in the angles ψ_{ij} and ψ_{Nj} for different NH_3 molecules when H_o is at angle α with respect to the GIC c-axis. Thus the ^1H NMR spectrum will resemble a typical powder pattern. Examples of these powderlike spectra have been given by Miller et al.¹⁴ The experimentally observed narrow NMR spectral lines and simple features (shown in Figs. 3, 4 and 6) imply considerable motional averaging (with correlation times of less than 10^{-5} sec.) due to: (a) fast rotation of NH_3 molecules about the C_3 molecular symmetry axis (equivalence of protons), and (b) fast reorientations of the molecular C_3 -axes about the GIC c-axis (fast averaging over the angle ϕ). These rapid motional averagings imply that $A_{12}=A_{23}=A_{31}=A$ and $B_1=B_2=B_3=B$ in equation (1). These equalities simplify the calculations considerably. We may couple the three proton spins of the NH_3 molecule into the total spin, $I = I_1 + I_2 + I_3$ and $I_z = I_{1z} + I_{2z} + I_{3z}$. Thus we have:

$$\sum_{ij} I_i \cdot I_j = (I \cdot I - \sum_i I_i \cdot I_i) / 2 \quad (4)$$

$$\sum_{ij} I_{iz} I_{jz} = (I_z^2 - \sum_i I_{iz}^2) / 2 \quad (5)$$

and their eigenvalues are $[I(I+1)/2] - (9/8)$ and $(I_z^2/2) - (3/8)$ since $I_i = \frac{1}{2}$ and $I_{iz} = \pm \frac{1}{2}$. Thus the energy level for the spin Hamiltonian H of equation (1) is:

$$E(I, I_z, S_z) = \gamma_H H_o I_z + (A/2) [I(I+1) - 3I_z^2] + \gamma_N H_o S_z - 2BI_z S_z \quad (6)$$

In equation (6), we have temporarily neglected the effect of H_Q . We also note that H_Q may also contribute to spectral line broadening. These effects will be considered later.

The energy levels, as given by equation (6), are shown schematically (not to scale) in Fig. 8 as $H_Z + H_D$ (Combined nuclear Zeeman and dipolar effects while ^{14}N quadrupolar effects are omitted). When the ^{14}N spin S is omitted, the couplings of three spin $\frac{1}{2}$ nuclei would result in a total spin of $I=3/2$ (non-degenerate) and $I=1/2$ (doubly degenerate). For $I=3/2$, the energy levels are at $(3\gamma_{\text{H}}H_0/2) - (3A/2)$, $(\gamma_{\text{H}}H_0/2) + (3A/2)$, $(-\gamma_{\text{H}}H_0/2) + (3A/2)$ and $(-3\gamma_{\text{H}}H_0/2) - (3A/2)$ for $I_z=3/2, 1/2, -1/2$ and $-3/2$. The differences between the adjacent energy levels are $\gamma_{\text{H}}H_0 - 3A$, $\gamma_{\text{H}}H_0$ and $\gamma_{\text{H}}H_0 + 3A$. For $I=1/2$, the energy levels are at $\gamma_{\text{H}}H_0/2$ and $-\gamma_{\text{H}}H_0/2$ for $I_z=1/2$ and $-1/2$. The difference is $\gamma_{\text{H}}H_0$. The theoretical NMR spectrum is a three spectral line pattern at resonance frequencies of $\gamma_{\text{H}}H_0 - 3A, \gamma_{\text{H}}H_0$ and $\gamma_{\text{H}}H_0 + 3A$ with 1:2:1 intensity ratio. That is, we have one central component (at frequency $\gamma_{\text{H}}H_0$) and two satellites with frequency shifts of $D_{\text{HH}} = \pm 3A$ from the center, where the subscript HH emphasizes that the frequency shift (the frequency difference between the central component and one of the satellite components) comes from $^1\text{H}-^1\text{H}$ dipolar coupling. When we include the ^{14}N spin S , then the NMR spectra in the vicinity of the frequency $\gamma_{\text{H}}H_0$ would come from transitions between $E(I, I_z, S_z)$ and $E(I, I_z \pm 1, S_z)$ where the energy levels are given by equation (6) since the frequency range of our NMR spectra are much less than $\gamma_{\text{N}}H_0$ (~ 40 KHz vs. ~ 4 MHz) and there would be no flips of ^{14}N spins. There are three triplets, the central triplet (denoted as 4-6 in spectra A of Fig. 8) and two satellite triplets (1-3 and 7-9 in spectra A of Fig. 8). The frequency shifts of the satellite triplets are $D_{\text{HH}} = \pm 3A$ from the central triplet due to the $^1\text{H}-^1\text{H}$ dipolar coupling. Within

each triplet, the differences are $D_{\text{NH}} = \pm 2B$ between adjacent resonance lines due to the $^1\text{H}-^{14}\text{N}$ dipolar coupling. The difference between the expressions for D_{HH} and D_{NH} ($\pm 3A$ vs. $\pm 2B$) is due to the well-known factor of $3/2$ between like and unlike spin pairs. This theoretical spectrum is shown as "A" in the insert of Fig. 8 where the effect of H_Q has been neglected. This theoretical NMR spectrum is in qualitative agreement with the experimental spectra in Figs. 3, 4 and 6. Certain discrepancies, such as the uneven spacings of lines 4-6 in Fig. 4 when α is away from 0° or 90° , will be shown later as due to the effects of H_Q . The central component (near the frequency $\nu_{\text{H}}H_0$) may also be more intense in the experimental spectrum than predicted because of the presence of liquid or adsorbed NH_3 in the sample tube in addition to the GIC.

We will now calculate the motionally averaged values of A and B. We will begin with the latter. A Cartesian coordinate system x, y, z may be fixed in the GIC crystal with unit vectors $\hat{i}, \hat{j}, \hat{k}$. The z -axis is parallel to the crystallographic c -axis. The magnetic field H_0 is in the xz -plane and at angle α away from the z -axis, hence its unit vector \hat{H}_0 is:

$$\hat{H}_0 = \hat{k} \cos \alpha + \hat{i} \sin \alpha \quad (7)$$

This Cartesian coordinate system may be transformed into the spherical coordinate system where the unit vectors are:

$$\begin{aligned} \hat{e}_r &= \hat{i} \sin \theta \cos \phi + \hat{j} \sin \theta \sin \phi + \hat{k} \cos \theta \\ \hat{e}_\theta &= \hat{i} \cos \theta \cos \phi + \hat{j} \cos \theta \sin \phi - \hat{k} \sin \theta \\ \hat{e}_\phi &= -\hat{i} \sin \phi + \hat{j} \cos \phi \end{aligned} \quad (8)$$

The instantaneous orientation of the NH_3 molecular C_3 -axis is given by the angles θ and ϕ as shown in Fig. 7. The unit vector \hat{e}_r is

parallel to the C_3 -axis, while the two unit vectors \hat{e}_θ and \hat{e}_ϕ are perpendicular to the C_3 -axis. The N-H internuclear vector \underline{r}_{Nj} is at a fixed angle η from the C_3 -axis as shown in Fig. 7. For the unit vector \hat{r}_{Nj} , its component parallel to the C_3 -axis is $\cos \eta$ while the perpendicular component is $\sin \eta$. If the perpendicular component is at angle β from the unit vector \hat{e}_θ , then we have:

$$\hat{r}_{Nj} = \hat{e}_r \cos \eta + (\hat{e}_\theta \cos \beta + \hat{e}_\phi \sin \beta) \sin \eta \quad (9)$$

For any instantaneous orientation of \underline{r}_{Nj} , we have:

$$\cos \psi_{Nj} = \hat{r}_{Nj} \cdot \hat{H}_0 \quad (10)$$

We may substitute equation (8) into (9) to express \hat{r}_{Nj} in terms of $\hat{i}, \hat{j}, \hat{k}$ and then take the scalar product with equation (7),

$$\begin{aligned} \cos \psi_{Nj} = & \cos \alpha (\cos \eta \cos \theta - \sin \eta \sin \theta \cos \beta) \\ & + \sin \alpha (\cos \eta \sin \theta \cos \phi + \sin \eta \cos \theta \cos \beta \cos \phi - \sin \eta \sin \beta \sin \phi) \end{aligned} \quad (11)$$

We will now take the motional average of the $(3\cos^2 \psi_{Nj} - 1)/2$ term. The average is over both $\beta = 0$ to 2π (rapid reorientations of NH_3 molecules about their molecular C_3 -axis) and $\phi = 0$ to 2π (rapid precessions of molecular C_3 -axis about the c-axis of the GIC). The only non-zero averages are $\langle \cos^2 \beta \rangle = \langle \sin^2 \beta \rangle = \langle \cos^2 \phi \rangle = \langle \sin^2 \phi \rangle = 1/2$, while other averages, such as $\langle \cos \beta \rangle$, $\langle \cos \beta \sin \beta \rangle$, etc. are all zero. After averaging over β and ϕ , the result is:

$$\langle (3\cos^2 \psi_{Nj} - 1)/2 \rangle = [(3\cos^2 \theta - 1)/2] [(3\cos^2 \eta - 1)/2] [(3\cos^2 \alpha - 1)/2] \quad (12)$$

From equation (3), the motionally averaged value of B is:

$$B = \gamma_H \gamma_N h r_{Nj}^{-3} [(3\cos^2 \theta - 1)/2] [(3\cos^2 \eta - 1)/2] [(3\cos^2 \alpha - 1)/2] \quad (13)$$

It is necessary to average over the probability distribution over the angle θ between the NH_3 molecular C_3 -axis and the TGIC c-axis. This probability function will be denoted by $P(\theta)$. We may introduce

the order parameter S which is usually identified as¹⁴

$$S = \langle (3\cos^2\theta - 1)/2 \rangle \quad (14)$$

In equation (14) and hereafter, the angular bracket will be used to denote averaging over the probability distribution of θ :

$$\langle f(\theta) \rangle = \int_0^\pi f(\theta)P(\theta)\sin\theta \, d\theta / \int_0^\pi P(\theta)\sin\theta \, d\theta \quad (15)$$

where $f(\theta)$ may be any function of θ . Thus B is given by:

$$B = \gamma_H \gamma_N^2 r_{Nj}^{-3} S [(3\cos^2\eta - 1)/2] [(3\cos^2\alpha - 1)/2] \quad (16)$$

For random distributions of the angle θ (P is a constant and is independent of θ), then $S=0$ and the NMR spectra would collapse to a single resonance line. This is the case of totally isotropic motion. However, the experimental result of three sets of triplets for the T_GIC indicates that $S \neq 0$ and certain angles of θ are preferred. That is, the NH_3 molecules are situated in a potential well and the angle θ will vary over a limited range near the bottom of the potential well.

Since the $^1\text{H}-^1\text{H}$ internuclear vector \underline{r}_{ij} is perpendicular to the NH_3 molecular C_3 -axis, equation (16) may also be used for the motionally averaged value of A by setting $\eta=90^\circ$ and by replacing γ_N and r_{Nj} with γ_H and r_{ij} . The result is:

$$A = (\gamma_H^2 r_{ij}^{-3} / 2) S [(3\cos^2\alpha - 1)/2] \quad (17)$$

The frequency shifts of the satellite triplets are $D_{\text{HH}}=3A$ from the central triplet due to the $^1\text{H}-^1\text{H}$ dipolar interaction. Using the H-H distance of 1.624 Å from the electron diffraction studies¹⁵ of NH_3 molecules in the gas phase, the absolute value of D_{HH} in KHz is:

$$|D_{\text{HH}}| = 3|A| = 42.1 |S| \left| (3\cos^2\alpha - 1)/2 \right| \quad (18)$$

From Figs. 4 and 5 for K_TGIC at room temperature and 60 MHz, it may be seen that the central lines of the triplets (lines 2,5,8) are

evenly spaced, thus either ν_{25} or ν_{58} may be identified with D_{HH} . This is shown as the lower diagram of Fig. 9. The experimental data (shown as crosses) clearly display the $(3\cos^2\alpha - 1)/2$ angular dependence and agrees well with the calculated curve from equation (18) when we choose the order parameter to be $|S| = 0.41$.

The effect of H_Q will now be included. This has no effect on the 1H - 1H dipolar interaction and on D_{HH} . However, it is now necessary to consider the effects of both the Zeeman and quadrupolar interactions on the ^{14}N nucleus. These interactions will be denoted by H_N and H_Q respectively, where $H_N = \gamma_N H_0 S_z$. Because of the combined effects of both H_N and H_Q , the ^{14}N nuclear spin S is not necessarily quantized along the magnetic field H_0 (the Z-axis).

In the crystal coordinate system (x,y,z) of the GIC, then H_Q is axially symmetric along the z-axis because of motional averaging. The effective quadrupolar coupling constant will be denoted as e^2qQ_e/h . The standard matrix²⁰ for H_Q with spin $S=1$ in the principal coordinate system is:

$$M_Q = (e^2qQ_e/4h) \begin{pmatrix} -1 & 0 & 0 \\ 0 & 2 & 0 \\ 0 & 0 & -1 \end{pmatrix} \quad (19)$$

where the eigenstates are for $S_z=1,0$ and -1 . We have chosen H_0 at angle α away from the z-axis in the xz-plane. Using the standard matrices of S_z and S_x , the Zeeman matrix for H_N is:

$$M_N = (\gamma_N H_0 c) \begin{pmatrix} 1 & 0 & 0 \\ 0 & 0 & 0 \\ 0 & 0 & -1 \end{pmatrix} + (2^{-1/2} \gamma_N H_0 s) \begin{pmatrix} 0 & 1 & 0 \\ 1 & 0 & 1 \\ 0 & 1 & 0 \end{pmatrix} \quad (20)$$

where $\cos\alpha$ and $\sin\alpha$ have been abbreviated as c and s .

A similarity transformation $R^{-1}MR$ will be used for the transformation from the crystal coordinate system (x,y,z) to the magnetic

field coordinate system (X,Y,Z). The matrix R is chosen such that $R^{-1}M_N R$ is diagonal. Thus we get:

$$R^{-1}(M_N + M_Q)R = (\gamma_N H_0) \begin{pmatrix} 1 + (\lambda/2)(1 - 3c^2) & 3cs\lambda/2^{1/2} & -3s^2\lambda/2 \\ 3cs\lambda/2^{1/2} & \lambda(3c^2 - 1) & -3cs\lambda/2^{1/2} \\ -3s^2\lambda/2 & -3cs\lambda/2^{1/2} & -1 + (\lambda/2)(1 - 3c^2) \end{pmatrix} \quad (21)$$

where the quadrupolar/Zeeeman interaction ratio λ is defined by

$$\lambda = e^2 q Q_e / (4 \gamma_N H_0 h) \quad (22)$$

and the eigenstates in (21) are the ^{14}N spin functions quantized in the direction of the magnetic field H_0 (the Z-axis). These states will be denoted as ψ_1 , ψ_0 , and ψ_{-1} where the subscripts are the eigenvalues of S_z .

We will now diagonalize the matrix given by equation (21). For small λ when the quadrupolar effect is weak as compared to the ^{14}N Zeeman term, a perturbation calculation can be made to first order in λ . Because of the quadrupolar interaction, there is some mixing among the eigenstates ψ_1 , ψ_0 and ψ_{-1} . The perturbed wave functions will be denoted by $\bar{\psi}_1$, $\bar{\psi}_0$ and $\bar{\psi}_{-1}$ and are given by:

$$\begin{aligned} \bar{\psi}_1 &= \psi_1 + (3cs\lambda/2^{1/2})\psi_0 - (3s^2\lambda/4)\psi_{-1} \\ \bar{\psi}_0 &= \psi_0 - (3cs\lambda/2^{1/2})(\psi_1 + \psi_{-1}) \\ \bar{\psi}_{-1} &= \psi_{-1} + (3cs\lambda/2^{1/2})\psi_0 + (3s^2\lambda/4)\psi_1 \end{aligned} \quad (23)$$

Their eigenvalues are given by the diagonal matrix elements of equation (21). They will be denoted as ϵ_1 , ϵ_0 and ϵ_{-1} .

For the resonance frequencies of the central triplet (lines 4,5,6) of the ^1H NMR spectra, we will now consider the complete spin Hamiltonian given by equation (1) except for the ^1H - ^1H dipolar

interaction. Thus we will use the Hamiltonian

$$H = \gamma_H H_0 I_Z + \gamma_N H_0 S_Z + H_Q + H' \quad (24)$$

where H' is the ^1H - ^{14}N dipolar Hamiltonian. In the absence of H_Q , it is given by equations (6) and (16),

$$H' = -2BI_Z S_Z = -2bI_Z [S_Z(3\cos^2\alpha - 1)/2] \quad (25)$$

where b is a constant and is given by

$$b = \gamma_H \gamma_N h r_{Nj}^{-3} S(3\cos^2\eta - 1)/2 \quad (26)$$

where S is the order parameter. In the presence of the ^{14}N quadrupolar interaction, the ^{14}N spin may be quantized with non-vanishing components away from the Z -direction, hence it is necessary to use²⁰

$$H' = -2bI_Z S' \quad (27)$$

where S' is defined by

$$S' = [S_Z(3\cos^2\alpha - 1)/2] + [S_X \cos\alpha \sin\alpha / 2] \quad (28)$$

The resonance frequencies for $m=1,0$ and -1 are given by

$$\begin{aligned} \nu_m &= \langle I_Z=1/2, \Psi_m | H | I_Z=1/2, \Psi_m \rangle - \langle I_Z=-1/2, \Psi_m | H | I_Z=-1/2, \Psi_m \rangle \\ &= [(\gamma_H H_0/2) + \epsilon_m - b \langle \Psi_m | S' | \Psi_m \rangle] - [(-\gamma_H H_0/2) + \epsilon_m + b \langle \Psi_m | S' | \Psi_m \rangle] \\ &= \gamma_H H_0 - 2b \langle \Psi_m | S' | \Psi_m \rangle \end{aligned} \quad (29)$$

Using Ψ_m given by equation (23), we get

$$\nu_{\pm 1} = \gamma_H H_0 \pm 2b[(3\cos^2\alpha - 1)/2] - g \quad (30)$$

$$\nu_0 = \gamma_H H_0 + 2g \quad (31)$$

where g is the extra shift of the NMR spectral lines due to the ^{14}N quadrupolar coupling:

$$g = (9b\lambda/4)\sin^2 2\alpha \quad (32)$$

The frequencies $\nu_{\pm 1}$ correspond to lines 4 and 6 in Figs. 4,5 and 8, while the frequency ν_0 correspond to line 5.

The energy levels are shown schematically (not to scale) in Fig. 8, where H_D denotes the $^1\text{H}-^1\text{H}$ and the $^1\text{H}-^{14}\text{N}$ dipolar interactions and H_Q denotes the ^{14}N quadrupolar interactions. The theoretical ^1H NMR spectra are shown in the insert. For spectrum A, the effect of H_Q is neglected. The spectral lines of the central triplet are evenly spaced with $\Delta\nu_{45} = \Delta\nu_{56} = 2b(3\cos^2\alpha - 1)/2$. This has been denoted as $D_{\text{NH}} = 2B$ where B is given by equation (16) and the subscript NH emphasizes that the splittings between adjacent spectral lines are due to the $^1\text{H}-^{14}\text{N}$ dipolar interactions. In spectrum B, the effects of H_Q have been included by a perturbation calculation to first order in λ . We have found that spectral lines 4 and 6 have shifted by g in the same direction while line 5 has shifted by $2g$ in the opposite direction. We note that $\Delta\nu_{46}$ is independent of g , hence we have used $D_{\text{NH}} = \Delta\nu_{46}/2$ to calculate D_{NH} from the experimental data shown in the top diagram of Fig. 5. The results are shown as the crosses in the top diagram of Fig. 9. The $(3\cos^2\alpha - 1)/2$ angular dependence (shown as the solid curve) may be clearly seen. We also note that H_Q has no effect on the $^1\text{H}-^1\text{H}$ dipolar interactions. For both spectra A and B of Fig. 8, we may identify either $\Delta\nu_{25}$ or $\Delta\nu_{58}$ with $D_{\text{HH}} = 3A$ given by equation (17).

From the geometry of the NH_3 molecule, it may be seen that $r_{ij} = 3^{1/2}r_{\text{Nj}}\sin\eta$. From A and B given by equations (17) and (16), we note that the ratio $D_{\text{NH}}/D_{\text{HH}} = (2B)/(3A)$ depends on the angle η only:

$$D_{\text{NH}}/D_{\text{HH}} = 2(3^{1/2})(\gamma_{\text{N}}/\gamma_{\text{H}})(1-3\cos^2\eta)\sin^3\eta \quad (33)$$

From Fig. 9, the experimental ratio is $D_{\text{NH}}/D_{\text{HH}} = 0.116$ which gives

$\eta = 68.1^\circ$. This is in very good agreement with the value of $\eta = 68.4^\circ$ obtained by electron diffraction studies of NH_3 in the gas phase.¹⁵

From equations (30) and (31), the difference

$$g = (\nu_{56} - \nu_{45})/6 = (2\nu_5 - \nu_4 - \nu_6)/6 \quad (34)$$

should be proportional to λ with the angular dependence of the form of $\sin^2 2\alpha$. We have used equation (34) to calculate g from the experimental data shown in the top diagram of Fig. 5. The results are shown as the crosses in the upper diagram of Fig. 10. The $\sin^2 2\alpha$ angular dependence may be clearly seen. The experimental data are in good agreement with the theoretical curve calculated from equation (32) using $9b\lambda/4 = 0.195$ KHz which gives $\lambda = 0.087$.

From the proton resonance frequency of 59.75 MHz, we get $\gamma_{\text{NH}_3} = 4.3$ MHz. From equation (22), we have $|e^2qQ_e/h| = 1.50$ MHz. This effective coupling constant is related to the actual coupling constant e^2qQ/h of the NH_3 molecule by the order parameter S :

$$|e^2qQ_e/h| = |S| |e^2qQ/h| \quad (35)$$

Using $|S| = 0.41$, we get $|e^2qQ/h| = 3.7$ MHz. This indirectly determined ^{14}N quadrupolar coupling constant is intermediate between the gaseous NH_3 value²² of 4.1 MHz and the solid NH_3 value²³ of 3.2 MHz. This result for the intercalated NH_3 is consistent with the relatively weak chemical binding of NH_3 molecules in the galleries of the TGIC.

From equations (30) and (31), the average frequency

$$\nu_A = (\nu_4 + \nu_5 + \nu_6)/3 \quad (36)$$

of the central triplet is independent of both ^{14}N - ^1H dipolar interaction and ^{14}N quadrupolar effects. The experimental ν_A vs. α curve in the lower diagram of Fig. 10 shows the residual chemical shift effects:

$$\nu_A = \nu_{AZ} \cos^2 \alpha + \nu_{AX} \sin^2 \alpha \quad (37)$$

For the solid curve in the lower diagram of Fig. 10, we have chosen $\nu_{AZ}=0.01$ and $\nu_{AX}=-0.62$ KHz. These frequencies give a chemical shift anisotropy of $\delta_z - \delta_x = 10.7$ p.p.m. for protons in the KTGIC.

In summary, it may be seen that for the central triplet, we have transformed ν_4, ν_5, ν_6 into $D_{NH}=(\nu_4-\nu_6)/2$, $g=(2\nu_5-\nu_4-\nu_6)/6$ and $\nu_A=(\nu_4+\nu_5+\nu_6)/3$. These parameters are related to the $^1H-^{14}N$ dipolar interaction, the ^{14}N quadrupolar effect and the 1H chemical shift. These parameters also show different angular dependences on α .

From the room temperature KTGIC spectra shown in Fig. 4, it may be seen that there are considerable broadenings of the outer triplets (spectral lines 1-3 and 7-9) when the orientations are away from $\alpha=0^\circ$ or 90° . This is due to the slight misalignment of the c-axes of the various crystallites within the TGIC. This angle of misalignment will be denoted as ξ . For equation (18), the actual range of angle is $\alpha \pm \xi$ when we consider the individual crystallites. The range of D_{HH} (in KHz) is given by

$$D_{HH} = 17.2 \left\{ [3\cos^2(\alpha \pm \xi) - 1] / 2 \right\} \\ = 17.2 \left[(3\cos^2\alpha - 1) / 2 \right] \pm (25\sin 2\alpha) \xi + \dots \quad (38)$$

where ξ is expressed in radians and we have used the experimental value $|S|=0.4$ for the TGIC. The last term is the extra broadening due to the crystal misalignment. This broadening increases rapidly when α is moved away from either 0° or 90° . The spectra in Fig. 4 is consistent with our previous estimate of $\xi \sim 0.05$ radians or 3° from the X-ray rocking curve shown in Fig. 1.

The frequency dependence of the 1H NMR spectra at room temperature and $\alpha=90^\circ$ may be seen by the comparison between Fig. 4 and Fig. 6. These spectra are taken at 60 MHz and 300 MHz respectively. The spectral line positions and the values of D_{HH} and D_{NH} are quite similar for these two frequencies. For the 300 MHz spectrum,

the ^{14}N quadrupolar interaction is overwhelmed by the Zeeman interactions. Except for the partial obscuring of the central line by adsorbed and gaseous NH_3 , there is good agreement between the experimental spectral line intensities and the theoretical 1:1:1:2:2:2:1:1:1 ratio.

Since $S \neq 0$, there are potential barriers for the NH_3 molecules in the galleries of the TGIC. We have studied the temperature dependence of the ^1H NMR spectra in order to determine these potential barriers. In Fig. 11, the 60 MHz spectra of KTGIC are shown at various temperatures. We have chosen $\alpha = 0^\circ$ in order to minimize the spectral line broadening. We have identified D_{HH} as the frequency difference between the central components of the central triplet and the satellite triplet. Equation (18) (with $\alpha = 0^\circ$) is then used to calculate $|S|$. Very similar results have also been obtained for the Rb- and Cs-compounds. The experimental values of $|S|$ at various temperatures have been summarized in Fig. 12.

From the ^1H NMR spectra of KTGIC at 60 MHz and $\alpha = 0^\circ$ for various temperatures shown in Fig. 11, the relaxation effects due to the ^{14}N quadrupolar interaction may also be inferred. For the central triplet (spectral lines 4 to 6 in the notation of Fig. 8), it may be seen that the line width (LW) at half-maximum is considerably larger for the satellites (lines 4 and 6) as compared to the central peak (line 5). This difference between the satellite and central peak LW will be denoted as $\Delta\nu$. This extra broadening comes from motional averaging and may be used to deduce the correlation times τ_c for the motions of NH_3 through the GIC gallery. For small τ_c , then $\Delta\nu$ (in Hz) is given by:¹⁸

$$\pi\Delta\nu = \sigma^2 \tau_c \quad (39)$$

where σ is the frequency range (in radians/sec) over which the motional averaging occurs. The correlation times can usually be expressed in the Arrhenius form, $\tau_c = \tau_0 e^{U/RT}$ where U is the activation energy per mole, R is the gas constant, T is the temperature and τ_0 is the frequency factor. Hence we get:

$$\ln \Delta\nu = \ln(\sigma^2 \tau_0 / \pi) + (U/RT) \quad (40)$$

In Fig. 13, we have plotted $\ln \Delta\nu$ vs. $1/T$ using the data from Fig. 11. We found $U=3.3$ kcal/mole or 0.14 eV and $\sigma^2 \tau_0 = 1.4$. Usually, we have $\tau_0 \sim 10^{-14}$ sec for ammonium compounds^{24,25}, hence we have $\sigma/2\pi \sim 2$ MHz which is of the same order of magnitude as the ^{14}N quadrupolar coupling constant in KTGIC.

The ^{14}N quadrupolar relaxation may be responsible for the extra LW of lines 4,6 as compared to line 5 and also for extra LW of lines 7,9 as compared to line 8. The correlation times τ_c may be related to the diffusion of NH_3 molecules in the graphite gallery. The diffusion is both the rotational and translational type, where the angle ϕ may change by 60° or 120° on jumping from one site to another site. Because of the threefold symmetry of the NH_3 molecule, rotations about the molecular C_3 axes do not contribute to the LW. We also note that the characteristics of the ^{14}N quadrupolar relaxation (sharp lines 5 and 8 but broader lines 4,6,7 and 9) are quite different from the misalignment broadening (lines 4,5 and 6 are quite sharp but lines 7,8 and 9 are much broader) given by equation (38) for α away from 0° or 90° . In Fig. 11, spectra are taken at $\alpha=0^\circ$ in order to minimize the misalignment broadening.

IV. SPECTRAL TEMPERATURE DEPENDENCE AND POTENTIAL BARRIERS

From the ^1H NMR spectra, we have deduced the absolute values (but not the signs) of the order parameter S at various temperatures. The results are shown in Fig. 12. For the motion of NH_3 in a potential energy well defined by the potential function V , then S may be calculated from equations (14) and (15) by using $P = e^{-V/RT}$.

Because of the layered structure of the TGIC and the symmetry between $+c$ and $-c$ directions of the TGIC lattice, we can write a Fourier expansion of V ,

$$V(\theta) = V_2 \cos 2\theta + V_4 \cos 4\theta + \dots \quad (41)$$

where V_2 , V_4 , etc. are constants. The first term is expected to be dominant. In the following, we will use $V = V_2 \cos 2\theta$ and consider

(A) the case of $V_2 > 0$ (potential minimum is at $\theta = 90^\circ$) and $S < 0$,
and (B) the case of $V_2 < 0$ (potential minimum is at $\theta = 0^\circ$) and $S > 0$.

(A) $V_2 > 0$, $S < 0$.

Except for a constant, we may write $V = 2V_2 \cos^2 \theta$. By introducing the new variable $u = \cos \theta$, then for $f(\theta) = \cos^2 \theta$, equation (15) may be written as:

$$\langle \cos^2 \theta \rangle = \int_{-1}^1 u^2 e^{-au^2} du / \int_{-1}^1 e^{-au^2} du \quad (42)$$

where $a = 2V_2/RT$. For $a \gg 1$, then the integration limits may be changed from $(-1, 1)$ to $(-\infty, \infty)$. Thus we get $\langle \cos^2 \theta \rangle = (2a)^{-1}$ and

$$|S| = -S = \frac{1}{2} - \frac{3}{2} \langle \cos^2 \theta \rangle = \frac{1}{2} - \frac{3RT}{8V_2} \quad (43)$$

The next term in the expansion is $3(\pi a)^{-1/2} e^{-a}$, which is very small for $a \gg 1$.

(B) $V_2 < 0$, $S > 0$.

The potential minimum is now at $\theta = 0^\circ$. For the expansion about this minimum, we have defined $u = \sin \theta$ and $V = 2|V_2| \sin^2 \theta$. By using

the Taylor's expansion $d\theta = (1 + \frac{1}{2}u^2 + \dots)du$, then we get

$$\langle \sin^2\theta \rangle = \int_0^1 e^{-au^2} (u^3 + \frac{1}{2}u^5 + \dots) du / \int_0^1 e^{-au^2} (u + \frac{1}{2}u^3 + \dots) du \quad (44)$$

where $a = 2|V_2|/RT$ is chosen to be positive. For $a \gg 1$, the integration limits may be changed from $(0,1)$ to $(0,\infty)$. Thus we get:

$$|S| = S = 1 - \frac{3}{2} \langle \sin^2\theta \rangle = 1 - \frac{3RT}{4|V_2|} \quad (45)$$

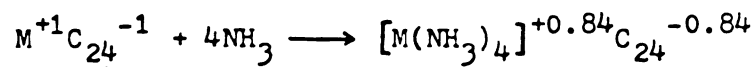
The next term in the expansion is $-3/(4a^2)$, which is very small for $a \gg 1$.

For TGIC, the experimental value of $|S|$ is 0.41 at room temperature (300°K). For case A with $S < 0$, the theoretical curve from equation (43) is shown as the solid line. From the room temperature value of $|S|$, we have found that $V_2 = 2.5$ Kcal/mole or 0.11 eV. For case B with $S > 0$, the theoretical curve from equation (45) is shown as the dashed line. From the room temperature value of $|S|$, we have found that $-V_2 = |V_2| = 0.76$ Kcal/mole or 0.033 eV. There is a factor of 7 difference between the slopes of these two theoretical lines. The experimental data are consistent with the choice of $S < 0$ (case A), thus the molecular C_3 -axes of NH_3 are nearly perpendicular to the crystallographic c-axis of the TGIC. The potential barrier height (the difference between the maximum and the minimum values of V) is $2V_2 = 5$ Kcal/mole or 0.22 eV.

V. DISCUSSION

In our present work, ^1H NMR spectroscopy has been used to study the first stage TGIC's, $\text{M}(\text{NH}_3)_x\text{C}_{24}$, where $x \sim 4$ and M denotes K, Rb or Cs. The results of these three TGIC's are quite similar to each other and are consistent with a rather mobile (liquid-like) intercalant layer of planar $\text{M}(\text{NH}_3)_4^+$ ions in between the carbon layers. These ions are the two-dimensional analogues of the $\text{M}(\text{NH}_3)_6^+$ ions commonly observed in alkali metal-liquid ammonia solutions.¹² This structure of TGIC agrees well with the recent X-ray diffraction data.^{26,27} For rigid $\text{M}(\text{NH}_3)_4^+$ intercalants, the order parameter S is -0.5 since $\theta=90^\circ$. Experimentally, we have observed $S=-0.41$ at room temperature due to the thermal vibrations of NH_3 molecules near the minimum of the potential barrier. The barrier height is ~ 0.2 eV.

The charge transfers in these TGIC's have been studied by ^{13}C NMR spectroscopy.¹⁷ The approximate reaction for the formation of the TGIC by the co-intercalation of NH_3 is:



As expected, there is partial solvation of the electronic charge on the carbon layers by the intercalated NH_3 . Nevertheless, this solvation by NH_3 is relatively weak. For example, when the TGIC is in contact with liquid NH_3 , the liquid phase remains clear without the highly characteristic colorations of alkali metal-ammonia solutions. While alkali metal ions in the TGIC may be fluidized by NH_3 , very little metal (if any) is extracted by the liquid NH_3 . This relatively weak solvation by NH_3 may be contrasted with the much stronger action of water which would violently decompose the TGIC. This relatively weak solvation by NH_3 is also consistent with the indirectly observed ^{14}N quadrupolar coupling constant of TGIC (3.7 MHz) which is intermediate

between the gaseous (4.1 MHz) and solid NH_3 (3.2 MHz) values.

In conclusion, the ^1H and ^{13}C NMR spectral studies have provided answers to the two fundamental questions about the TGIC: (a) what are the NH_3 molecular geometries, orientations and motions in the graphite galleries, and (b) whether the co-intercalated NH_3 molecules are only neutral "spacers" or compete with the carbon layers for the electrons given up by the alkali atoms.

VI. ACKNOWLEDGMENTS

The partial financial supports of National Research Council Fellowship for R. M. F. at Naval Research Laboratory, of National Aeronautics and Space Administration grant NAG-5-156 at Howard University, and of National Science Foundation grant DMR82-11554 at Michigan State University are gratefully acknowledged.

REFERENCES

1. M. S. Dresselhaus and G. Dresselhaus, Adv. Phys. 30, 139 (1981).
2. S. A. Solin, Adv. Chem. Phys. 49, 455 (1982).
3. M. S. Whittingham and A. J. Jacobson, Intercalation Chemistry, (Academic Press, New York, 1982).
4. L. Mattix, J. Milliken, H. A. Resing, J. Mintmire and D. C. Weber, Synth. Metals 10, 193 (1985).
5. A. P. Legrand, L. Facchini, D. Bonnin, J. Bouat, M. F. Quinton and F. Beguin, Synth. Metals 12, 175 (1985).
6. A. L. Blumenfeld, Y. V. Isaev and Y. N. Novikov, Synth. Metals 10, 193 (1985).
7. W. Rudorff and E. Schultze, Angew. Chem. 66, 305 (1954).
8. B. R. York and S. A. Solin, Phys. Rev. B 31, 8206 (1985).
9. B. R. York, S. K. Hark and S. A. Solin, Solid State Commun. 50, 595 (1984).
10. S. A. Solin, Y. B. Fan and X. W. Qian, Synth. Metals 12, 181 (1985).
11. X. W. Qian, D. R. Stump, B. R. York and S. A. Solin, Phys. Rev. Lett. 54, 1271 (1985).
12. J. C. Thompson, Electrons in Liquid Ammonia (Clarendon Press, Oxford, 1976).
13. J. Jortner and N. R. Kestner, Electrons in Fluids (Springer-Verlag, Berlin, 1973).
14. G. R. Miller, M. J. Moran, H. A. Resing and T. Tsang, Langmuir 2, 194 (1986).
15. M. T. Weiss and M. W. P. Strandberg, Phys. Rev. 83, 567 (1951).
16. T. Tsang and H. A. Resing, Solid State Commun. 53, 39 (1985).

17. Manuscript in preparation.
18. C. P. Slichter, Principles of Magnetic Resonance (Springer-Verlag, Berlin, 1978).
19. E. R. Andrew and Bersohn, J. Chem. Phys. 18, 159 (1950).
20. M. H. Cohen and F. Reif, Solid State Physics 5, 321 (1957).
21. D. L. Vanderhart, H. S. Gutowsky and T. C. Farrar, J. Amer. Chem. Soc. 89, 5056 (1967).
22. G. Hermann, J. Chem. Phys. 29, 875 (1958).
23. S. S. Lehrer and C. T. O'Konski, J. Chem. Phys. 43, 1941 (1965).
24. D. E. O'Reilly and T. Tsang, J. Chem. Phys. 46, 1291 (1967).
25. T. Tsang, T. C. Farrar and J. J. Rush, J. Chem. Phys. 49, 4403 (1968).
26. X. W. Qian, D. R. Stump and S. A. Solin, Phys. Rev. B33, 5756 (1986).
27. H. Zabel, A. Mageri, A. J. Dianoux and J. J. Rush, Phys. Rev. Lett. 50, 2094 (1983).

FIGURE CAPTIONS

- Fig. 1. Apparatus for sample preparation: V, total volume of specimen chamber; V', final sample volume; S, sealing point; T and T', teflon stopcocks; A, NH₃ reservoir; B, the GIC sample; C, connection to vacuum line.
- Fig. 2. X-ray rocking curve for the (002) reflection of K(NH₃)_{4.3}C₂₄ using MoK $\alpha_{1,2}$ radiation (0.71 Å wave length); X-ray intensity vs. angle Θ between X-ray beam and GIC surface.
- Fig. 3. Room temperature ¹H NMR spectra at 60 MHz and $\alpha=0^\circ$ for K(NH₃)_{4.3}C₂₄, Rb(NH₃)_{4.1}C₂₄ and Cs(NH₃)_{3.7}C₂₄. Only six resonance lines (out of 9) are shown.
- Fig. 4. ¹H NMR spectra of K(NH₃)_{4.3}C₂₄ at 60 MHz and room temperature vs. angle α between magnetic field H_0 and the crystallographic c-axis of GIC. The resonance lines are numbered 1 to 9 for the $\alpha=0^\circ$ spectrum. Low frequency is toward right. Arrow indicates the position of ¹H signal from adsorbed and gaseous NH₃.
- Fig. 5. Spectral line positions ν_m in KHz vs. angle α (from spectra of Fig. 4). The positions of lines 4, 5 and 6 (the central triplet) are plotted on an expanded scale in the upper diagram.
- Fig. 6. ¹H NMR spectrum of K(NH₃)_{4.3}C₂₄ at 300 MHz, room temperature and $\alpha=90^\circ$.
- Fig. 7. Geometry of NH₃ molecule intercalated between two carbon planes. Two of the hydrogen atoms are denoted by i and j. C₃ is the NH₃ molecular symmetry axis. H₀ is the direction of the magnetic field. N is the nitrogen atom. The z-axis is the crystallographic c-axis of the GIC.
- Fig. 8. Energy levels due to H_Z, H_D and H_Q (Zeeman, dipolar and ¹⁴N quadrupolar Hamiltonians). Theoretical NMR spectra are shown in the insert: (A) H_Q is neglected; (B) H_Q is included.

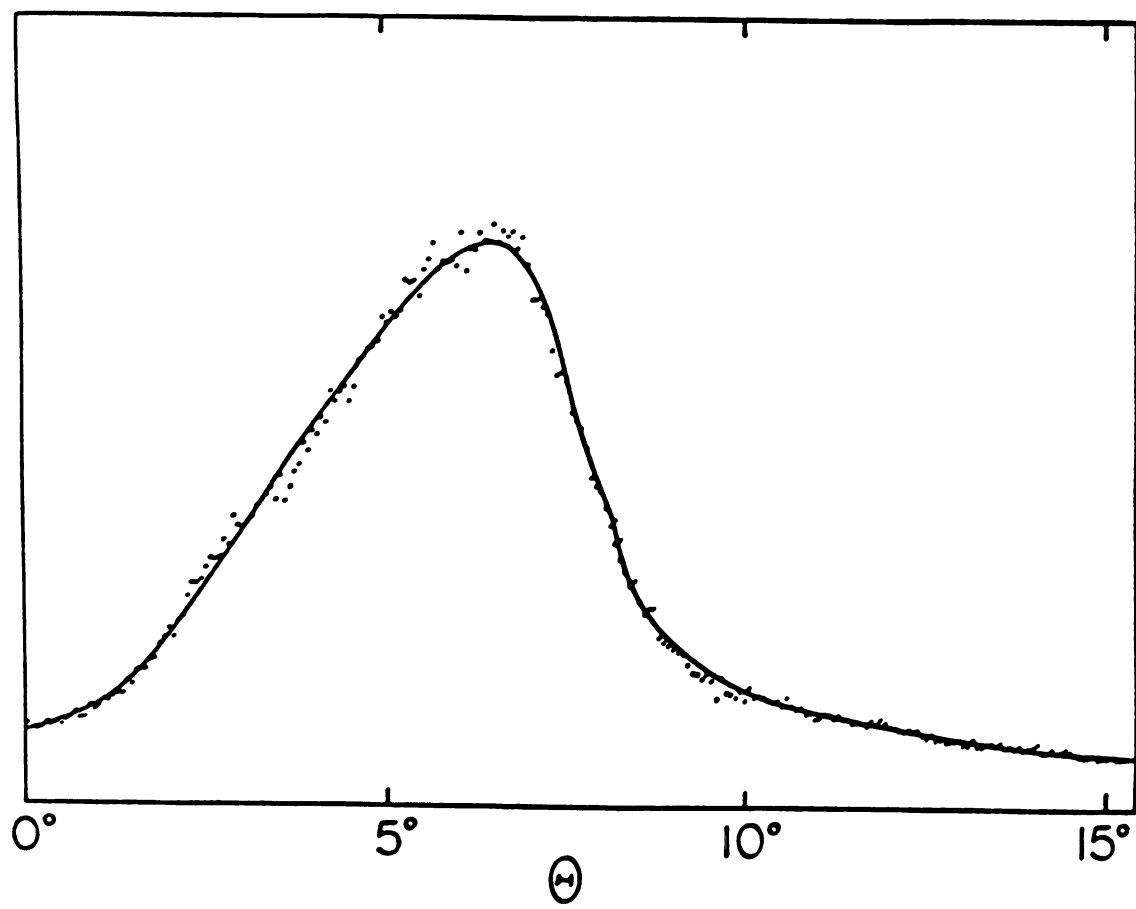
Fig. 9. D_{HH} and D_{NH} in KHz vs. angle α . Crosses are based on the experimental data for KTGIC at room temperature and 60 MHz from Fig. 5. The solid theoretical curves are proportional to $(3\cos^2\alpha - 1)/2$.

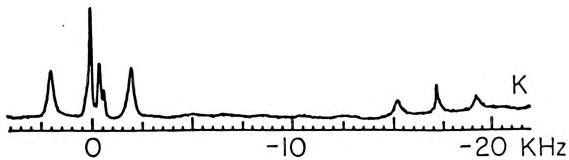
Fig. 10. Upper diagram: $g = (2\nu_5 - \nu_4 - \nu_6)/6$ in KHz vs. α . Crosses are based on experimental data in Fig. 5 for KTGIC at room temperature and 60 MHz. The solid line is the theoretical curve $g = 0.195\sin^2 2\alpha$. Lower diagram: $\nu_A = (\nu_4 + \nu_5 + \nu_6)/3$ in KHz vs. α . Crosses are based on experimental data in Fig. 5. The solid line is the theoretical curve from equation (37).

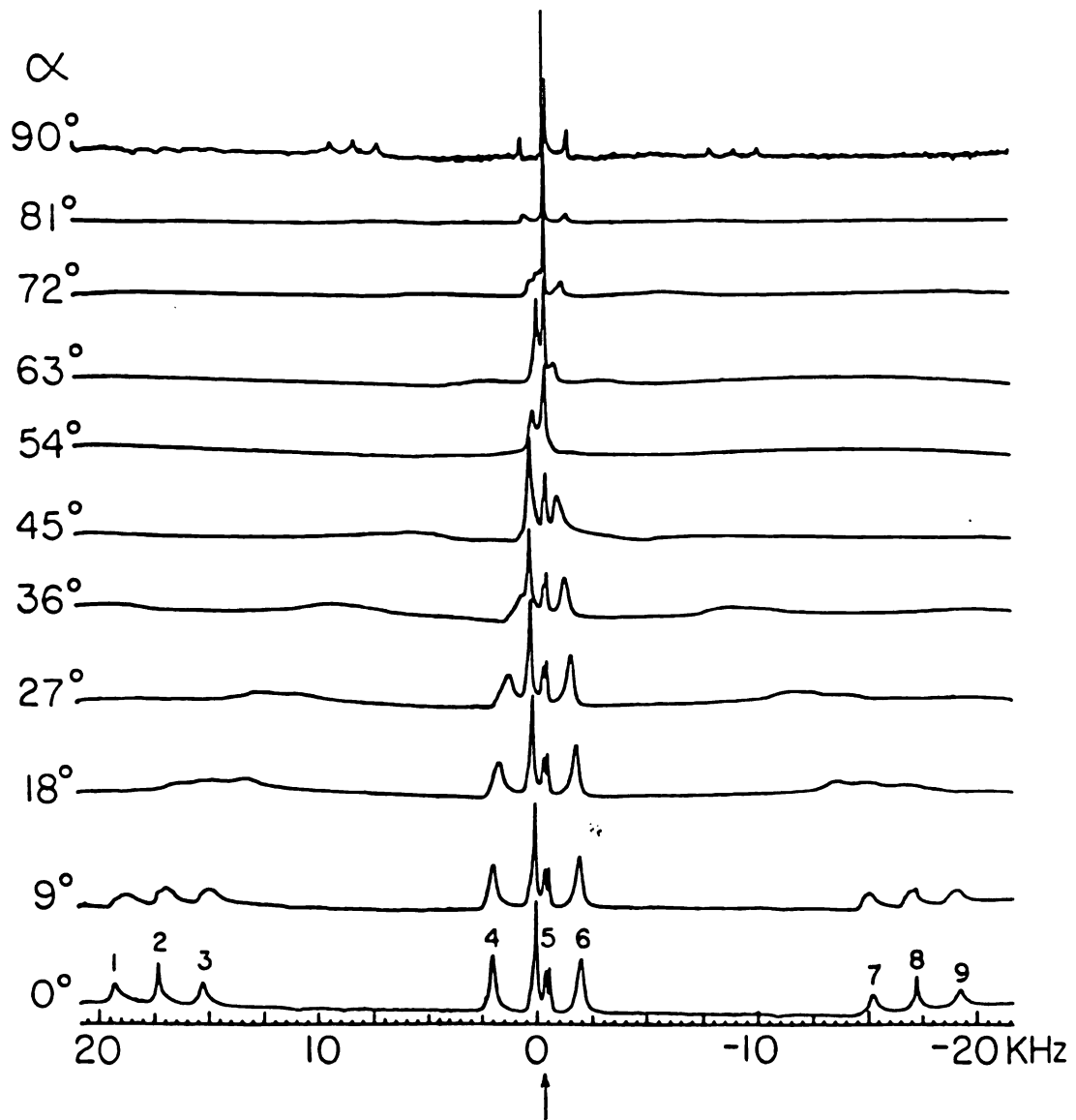
Fig. 11. ^1H NMR spectra at 60 MHz and $\alpha = 0^\circ$ for $\text{K}(\text{NH}_3)_4.3\text{C}_{24}$ at various temperatures (T in $^\circ\text{C}$). Only spectral lines 4-9 (in the notation of Fig. 8) are shown.

Fig. 12. Absolute value $|S|$ of the order parameter vs. temperature T in $^\circ\text{K}$. The crosses, triangles and circles are for the K-, Rb- and Cs-compounds respectively. The solid line is calculated from equation (43) for $S < 0$. The dashed line is calculated from equation (45) for $S > 0$.

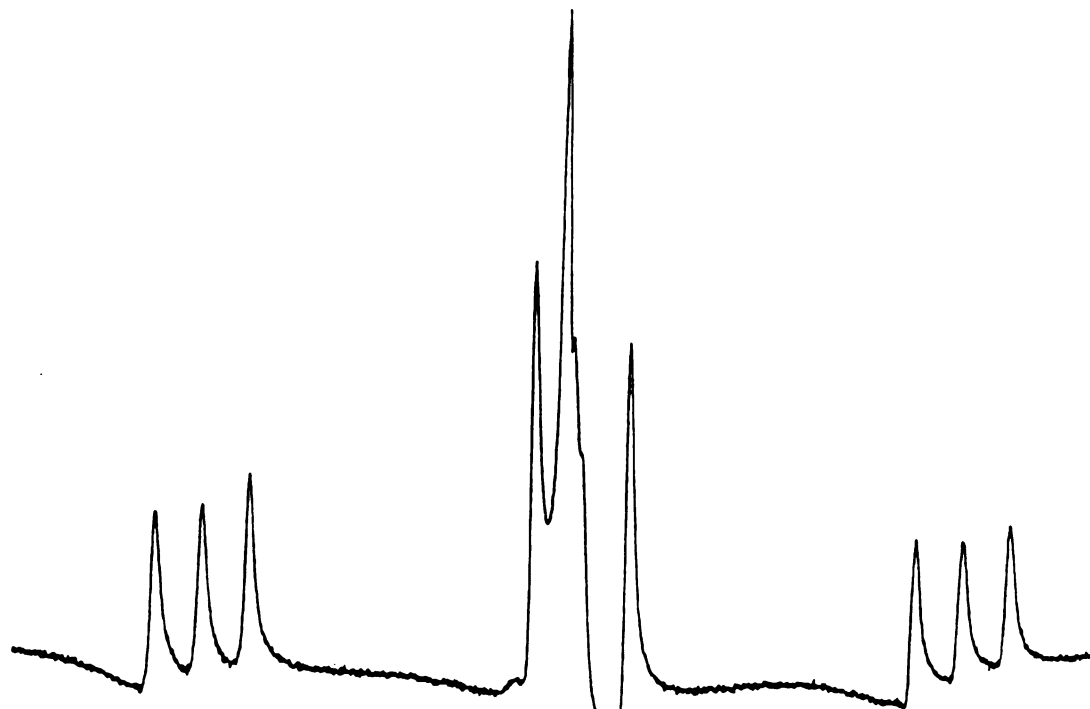
Fig. 13. $\ln \Delta\nu$ vs. $1000/T$ (in $^\circ\text{K}^{-1}$) for the KTGIC at 60 MHz and $\alpha = 0^\circ$.

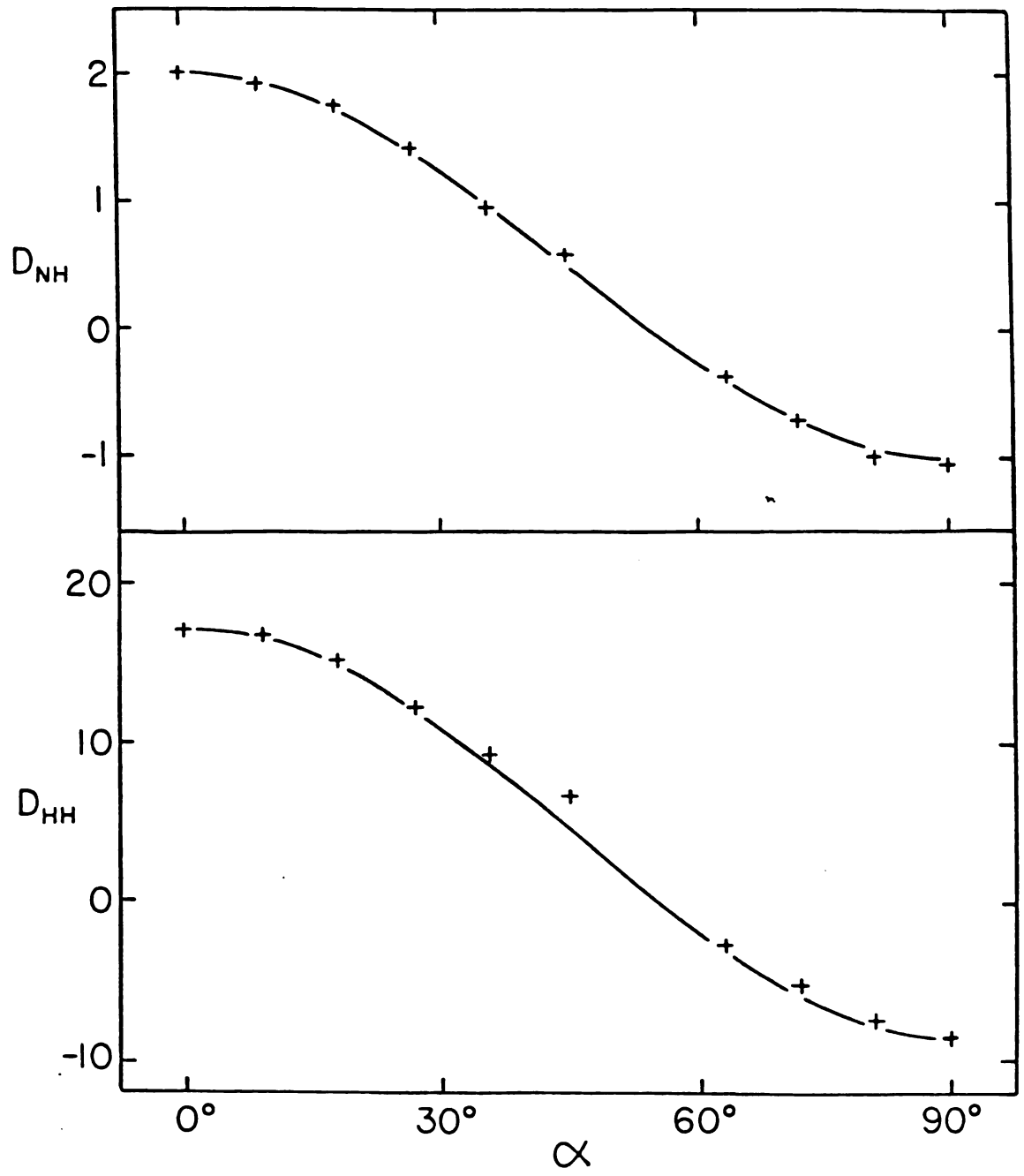


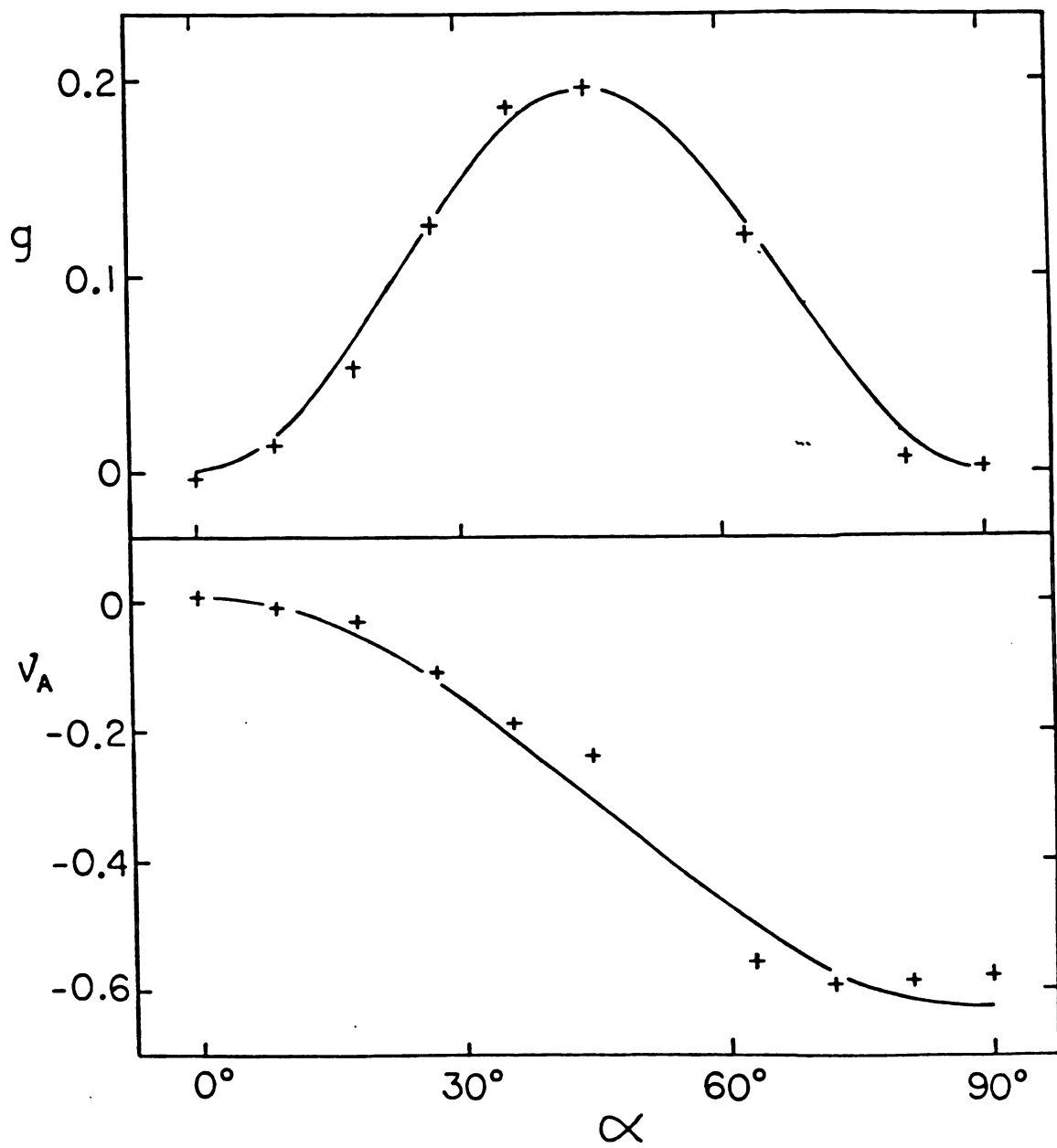




10 5 0 -5 -10KHz







^1H NMR Spectra

$\text{KC}_{24}(\text{NH}_3)_{4.2}$

$T(^{\circ}\text{C})$

12

-10

-44

-64

-85



